UNIVERSITÀ DEGLI STUDI DI NAPOLI "FEDERICO II"

Scuola Politecnica e delle Scienze di Base

Area Didattica di Scienze Matematiche Fisiche e Naturali

Dipartimento di Fisica "Ettore Pancini"



Laurea Magistrale in Fisica

Dark Matter search with the NEWSdm experiment using machine learning techniques

Relatori: Candidato:

Prof. Giovanni De Lellis Dott.ssa Antonia Di Crescenzo Dott. Andrey Alexandrov Chiara Errico Matricola N94/457

Anno Accademico 2018/2019

 $\begin{array}{c} Acting \ with \ love \\ brings \ huge \ happening \ \heartsuit \end{array}$

Contents

In	\mathbf{trod}	uction	1
1	Dar	k matter: first evidences and detection	3
	1.1	First evidences of dark matter	3
	1.2	WIMPs	8
	1.3		11
	1.4	Direct detection	13
	1.5	Detectors for direct search	15
		1.5.1 Bolometers	16
			17
		-	18
	1.6		20
	1.7		21
		·	23
2	The	NEWSdm experiment 2	25
	2.1		25
	2.2		28
			29
	2.3		30
			31
			34
			35
	2.4		35
			38
	2.5		40
	2.6		42

Contents	iv

3	Rec	construction of nanometric tracks	47
	3.1	Scanning process	47
	3.2	Analysis of NIT exposed to Carbon ions	49
	3.3	Shape analysis	50
	3.4	Plasmon analysis	51
		3.4.1 Accuracy	52
		3.4.2 Npeaks	53
		3.4.3 Isolated grains	55
	3.5	Plasmon efficiency	57
4	Dee	ep Learning and Convolutional Neural Network	60
•	4.1	1	60
	1.1	4.1.1 Classification and Regression problem	62
	4.2	Deep Learning	64
	4.3	Convolutional Neural Network	66
	1.0	4.3.1 Hyperparameters	69
5	CN	N for reconstruction of z-coordinates	71
	5.1	z-coordinate reconstruction	71
	0.1	5.1.1 CNN architecture	74
		5.1.2 Image dataset	75
	5.2	Results	77
	0.2	5.2.1 Small dataset with peaks	78
		5.2.2 Large dataset with peaks	80
		5.2.3 Uniform dataset	80
	5.3		81
Co	onclu	ısion	89
Aı	ppen	dix A	91
Bi	bliog	graphy 1	07

Introduction

One of the compelling topics that have captured the attention of researchers is the detection of dark matter. Since the beginning of the last century, increasing evidence of the presence of this unknown type of matter that permeates the universe arose. In particular, it results that only 5% of the matter is baryonic, and the remaining part is somehow "dark" since it does not interact electromagnetically. About 27% turns out to be dark matter whose presence has been shown through gravitational interactions and the remaining 68% is dark energy, today still completely unknown.

Weak Interacting Massive Particles (WIMPs) are one of the favourite candidates of dark matter because they are cold, i.e. not relativistic, interact only through weak and gravitational forces and are massive.

For the detection of dark matter there is a large number of experiments based on the direct detection and, in particular, on the detection of nuclear recoils induced by the scattering of WIMP particles off target nuclei. Moreover, an unambiguous proof of the galactic origin of dark matter would come from the observation of the direction of the WIMP induced nuclear recoils.

This thesis work was carried out within the NEWSdm experiment, which aims at detecting WIMP induced nuclear recoils in a solid target made of new generation nuclear emulsions, called Nano Imaging Trackers (NIT).

In the aforementioned detector, tracks are of the order of a few hundred nanometers. Nuclear emulsions allow reconstructing these tracks with optical microscopes. So NIT are scanned with optical microscopes that, although limited by optical resolution, are currently the best scanning devices.

To overcome the diffraction limit and reconstruct tracks in the bi-dimensional plane, the resonance effect of polarized light was exploited, according to which metal grains respond differently when illuminated by light with different polarization angles.

In spite of this improvements on the bi-dimensional plane, the axial resolution

Contents 2

remains limitated by the diffraction. Objects are well reconstructed if their distance from the focal plane is of the order of the Depth of Focus, while are badly reconstructed if they are close by. The idea of using a double focal plane was exploited in order to have the object out of focus at least at one of the planes.

The aim of this work is to achieve a nanometric accuracy in the tri-dimensional track reconstruction, by means of a convolutional neural network which improves significantly the accuracy on the z-cordinate.

This work is organized into five chapters:

- ◆ Chapter1: includes the path that brought evidence for dark matter into our Universe, a description of WIMPs and an overview of dark matter experiments focusing on direct detection and the potential of directionality;
- ◆ Chapter 2: dedicated to the description of the new nuclear emulsions, the NEWSdm experiment, the main background sources for this experiment and the readout strategy for nuclear emulsions through optical microscopes;
- ◆ Chapter 3: reports the study of the resonance effect of polarized light carried out on 70 nm NIT exposed to carbon ions;
- ◆ Chapter 4: for a brief description of artificial intelligence, machine learning, deep learning and of convolutional neural network;
- ◆ Chapter 5: setting the problem of z-coordinate reconstruction at nanometric scale, details of the convolutional neural network used on purpose and the results obtained.

Chapter 1

Dark matter: first evidences and detection

From the early twentieth century first hints of an unknown type of matter permeating the Universe arose. This new entity was called "dark matter" since it showed to feel only gravitational force. Despite all efforts and progress made by the scientific community so far, the dark matter intrinsic nature is still a big puzzle and therefore many experiments keep looking for a compelling evidence of its existence.

This chapter is focused on the description of evidences that suggest the presence of dark matter in the Universe, on the derivation of a quantitative estimate of its amount and on the description of the most promising dark matter candidate. Finally, an overview of techniques used for dark matter search is given, mainly focusing on the direct search and in particular on the directionality as a smoking gun in the discovery of dark matter from galactic origin.

1.1 First evidences of dark matter

In 1933 Fritz Zwikcky [1], observing the Doppler effect of galactic spectra of the Coma cluster, calculated the velocity dispersion of single galaxies belonging to the cluster. In order to estimate the mass of the cluster, he employed the virial theorem

$$\langle T \rangle = -\frac{1}{2} \langle U \rangle$$

where $\langle T \rangle$ and $\langle U \rangle$ are the average kinetic energy and potential energy, respectively. The mass of the cluster resulted to be four-hundred times larger than the observed luminous mass.

Approximately 40 years later Vera Rubin [2, 3] made a study about rotation curves of spiral galaxies, providing a further evidence about the large amount of non-luminous matter in the Universe. Spiral galaxies contain the majority of luminous matter in the galattic center.

Considering a star at distance r from the galactic center and equalizing gravitational and centrifugal forces

$$G\frac{mM(r)}{r^2} = \frac{mv^2}{r} \tag{1.1}$$

it is possible to obtain its velocity as

$$v = \sqrt{\frac{GM(r)}{r}} \tag{1.2}$$

where M(r) is the mass of the galaxy within the radius r. If the star is in the galactic center $M(r) \propto r^3$ and therefore $v \propto r$ while in the disc M = cost and the velocity is expected to show a Keplerian behavior, namely $v \propto \frac{1}{\sqrt{r}}$. Rubin found a completely different behavior: the rotation curves are flat for high r-values, as shown in Figure 1.1, requiring the presence of a huge amount of "dark matter" in the halos surrounding galaxies. These studies provide a further evidence of the large amount of non-luminous matter in the Universe. Remarkable information about the presence of missing matter is also given by the deflection of photon trajectories due to gravitational lensing [5, 6] which was observed for the first time in 1979 by Walsh [7]. The gravitational deflection of photons passing through a point mass M is:

$$\alpha = \frac{4GM}{c^2b} \tag{1.3}$$

where b is the impact parameter of the light scattering process due to the gravitational field [8]. If the light source is strictly behind the point mass one can observe it as a ring otherwise it appears as a distorted image. This phenomenon is observed for very large objects like galaxies or galaxy clusters while for stars an amplification of the brightness intensity, called microlensing, is observed [9]. Studying stars in the Large Magellanic Cloud it was observed that the amplitude of blue and red spectra have the same amplidute, thus

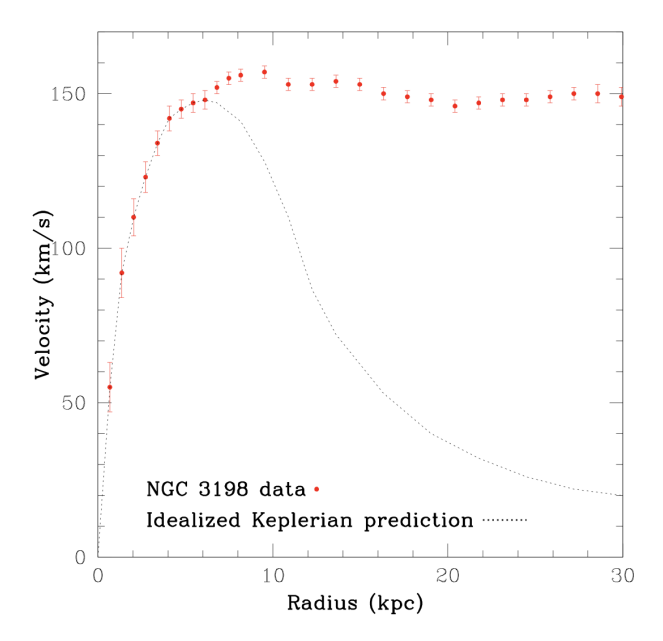


Figure 1.1: Red-dots represent the measured rotation speed of the HI regions in NGC 3198 while the dashed line idealizes the Keplerian behaviour [4].

indicating that the deflection $\Delta p/p$ is independent on the wavelength. If the photon has a momentum p, its gravitational mass will be p/c^{-1} and therefore it will receive a transverse momentum $\Delta p \propto p$ leading to the mentioned property.

Microlensing is a very powerful tool to investigate the Massive Compact Halo Objects (MACHOs) which includes neutron stars, brown dwarfs, black holes and unassociated planets that would emit very little or no radiation [10]. MACHOs were conceived as the natural baryonic candidates to explain the missing mass. Several collaborations used the microlensing effect to study the Great Magellanic Cloud [11–13]. However, many observations like those made by the MACHO Collaboration [11] found only 13-17 possible microlensing events on 11.9 million stars studied. These results suggest that

¹A photon with momentum p has an energy equal to $p \cdot c$. Since for a dimensional reason the energy has to be divided for c^2 we obtain that the effective gravitation mass of the photon is p/c.

the contribution provided by MACHOs is negligible since it accounts for just a few percent of the mass needed to explain the above mentioned evidence. At the same time the hypothesis of a dark matter made by undiscovered parlicles began to make its way.

The clearest evidence for non baryonic dark matter is reported by the *Bullet Cluster* which describes the collision of two clusters as shown in Figure 1.2 [14]. Two magenta clumps represent the interaction of baryonic matter emitting in the X-ray spectrum while in blu are indicated regions where the majority of the mass is inferred by gravitational lensing. The separation between the mass measured with the gravitational lensing and the X-ray emission is considered as one of the overwhelming evidence for a dark matter made by undiscovered particles.



Figure 1.2: Composite image of galaxy cluster 1E0657-56 [15]. Hot gas distributions are shown in magenta, dark matter halos in blue.

In 1965 Penzias and Wilson [16] discovered that the Universe is irradiated by an isotropic and uniform microwave radiation corresponding to the temperature of a black-body of ~ 3k. This radiation, known as Cosmic Microwave Background (CMB), gives information about the composition of the Universe and it is one of the most important proof for the Big Bang Theory. According to this model, the whole Universe was concentrated in a space-time singularity and after a violent explosion it expanded and cooled down.

The matter was initially grouped in a plasma formed by photons, leptons and quarks. The cooling down led the quarks to form protons that subsequently bound to electrons to form neutral atoms. Photons that until then were trapped in the plasma because of the scattering with free electrons (scattering Thomson) were free to travel in the Universe. The CMB is an imprint of that period called *Recombination epoch* since it makes it possible to retrieve the last scattering surface (i.e. the Universe when the photons separated from everything else) through the photon energy spectrum. The small anisotropies observed $O(10^{-6})$ [17–19] are interpreted as fluctuations of mass density in the Universe when the astrophysical structures seen nowadays were originated.

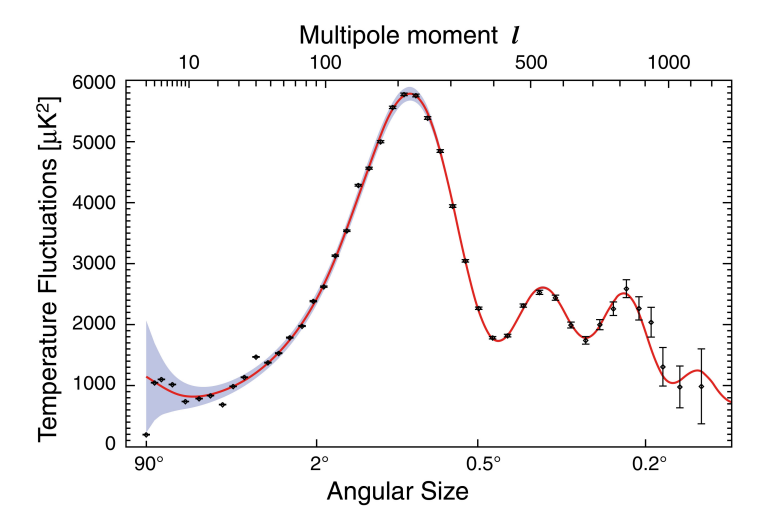


Figure 1.3: The CMB power spectrum as a function of the angular scale. Red line is the best fit to the model, and the grey band represents the cosmic variance [20].

The angular power spectrum of the CMB (see Figure 1.3), especially the position and width of peaks, provides important information about the baryon density and other cosmological parameters. The position of the first peak gives the total mass-energy density $\Omega \sim 1$: it rapresents the geometry of a flat Universe; the ratio between the first and the second peak provides the baryonic density $\Omega_b \sim 0.04$.

With the Big Bang Nucleosynthesis Theory (BBN) it is possible to obtain, in a different way, the baryonic density parameter [21]. BBN is the period

1.2 WIMPs 8

after the Big Bang where the first light elements were formed from the fusion between protons and neutrons, starting with deuterium, helium and small amounts of lithium. The deuterium formed in the stars is rapidly converted into 4He , so the huge amount of deuterium in the first second after the big bang follows the same behavior. Using nuclear physics and known reaction rates, BBN elemental abundances can be calculated, and so the ratio D/H heavily depends on the component of baryons in the Universe. Two values of $\Omega_B h^2$, depending on the amount of Deuterium have been calculated by Cyburt [22]:

$$\Omega_b h^2 = 0.0229 \pm 0.0013$$

 $\Omega_b h^2 = 0.0216^{+0.0020}_{-0.0021}$

Using the value $h = 0.674 \pm 0.005$ from recent observations for the reduced Hubble parameter [23], $\Omega_b = 0.0484 \pm 0.0010$, therefore only a small fraction of the matter is baryonic.

As discussed only 5% of the Universe turns to be known and the radiation contribution is negligible. This brought the development of the Λ_{CDM} model, also known as the cosmology standard model, based on the presence of dark energy and cold dark matter, as well as radiation and ordinary matter. This model, through measurements on the CMB and other observations such as BBN, SNIa and baryon acoustic oscillations (BAO) is the model that best fits observations and provides a mass-energy content for components of $\Omega_b = 0.049$, $\Omega_{CDM} = 0.265$ and $\Omega_{\Lambda} = 0.686$ [24] for baryon, cold dark matter and dark energy respectively.

1.2 WIMPs

Although the existence of dark matter is supported by many observational evidences, its nature remains one of the unresolved questions in particle and astroparticle physics.

In addition to evidences suggesting a large component of dark matter in the Universe, its presence becomes crucial to explain the formation of structures on cosmological scales. Several studies based on numerical simulations show that a cold dark matter is required to reproduce the astrophysical structures as seen today [25]. According to numerical models, smaller-scale structures are initially formed and then large structures like galaxies (bottom-up formation). On the contrary, hot dark matter implies a top-down formation.

1.2 WIMPs 9

The ideal non-baryonic dark matter candidate should therefore have the following properties:

- cold, to give rise to the formation of the large-scale structure;
- neutral, since it does not interact electromagnetically, but only through gravitation;
- "collisionless", with a very low interaction cross-section because they are still unobserved;
- massive, to take into account the total amount of matter in the Universe;
- stable, to be in such quantity, nowadays, to explain dynamics of galaxies.

In the Standard Model (SM) there are no particles that have these characteristics and the nature of dark matter is still unknown. It is possible to have a complete review of the candidates referring to [26, 27].

One of the favorite candidates for dark matter are Weakly Interacting Massive Particles (WIMPs) so the focus will be on this hypotesis. As pointed out, to describe the development of the structure of the Universe, we are looking for cold dark matter, that is non-relativistic at the time of decoupling with the rest of the matter "freeze-out". This happens when the annihilation rate becomes smaller than the expansion one [8]:

$$N\langle \sigma v \rangle \le H \tag{1.4}$$

where N is the WIMP density, v is the relative velocity of particles and antiparticles, σ is the WIMP-antiWIMP annihilation cross-section, and H is the Hubble parameter at the time of freeze-out. The density of a specific particle at the freeze-out is called *relic density*. From that moment, its abundance remains constant. This density can be theoretically calculated, so the candidate of dark matter must have the relic density according to the abundance reported at the end of the previous section 1.1.

Since WIMPs are massive and non-relativistic, their density will be given by Boltzman's law:

$$N(T) = \left(\frac{MT}{2\pi}\right)^{3/2} e^{-M/T} \tag{1.5}$$

1.2 WIMPs 10

The density of particles evolves with time according to the Friedman's equation of fluid in the non-relativistic case:

$$\frac{dn}{dt} = -3Hn - \langle \sigma v \rangle (n^2 - n_{eq}^2)$$
 (1.6)

where n is the density of the particle, H is the Hubble expansion rate, $\langle \sigma v \rangle$ is the thermally averaged total cross section for annihilation of a particle with its anti-particle times the relative velocity of the two particles in the center of mass frame and n_{eq} is the equilibrium thermal density. The exact value of the annihilation cross-section is not known, and the equation is not analytically solvable, but there exists a fairly simple analytic approximation that yields a solution with an accuracy of about 10% for an annihilation cross-section with a rather arbitrary dependence on energy [28]:

$$\Omega_{cdm}h^2 = \frac{m_{\chi}n_{\chi}}{\rho_c} \simeq \frac{3 \times 10^{-27} cm^3 s^{-1}}{\langle \sigma v \rangle}$$
 (1.7)

where χ is a generic dark matter particle. The cross-section necessary to observe the current dark matter density is of the order of the weak interaction scale.

The reason why WIMPs are considered as reasonable particles is found in equation (1.7). Indeed, if there is a new particle with weak scale interactions and masses from a few GeV/s to several TeV/s, as assumed for WIMPs, it can be estimated that it has an annihilation cross-section times velocities $\langle \sigma v \rangle = 10^{-25} {\rm cm}^3 {\rm s}^{-1}$. This value provides a relic density close to the abundance of dark matter reported.

One of the most important parameters for determining the expected event rate for a direct detection experiment is the local dark matter density. Therefore several models arose to describe the WIMPs profile density distribution according to the observed rotation curves in galaxies. Usually, dark matter halos are parametrised with a pseudo-isothermal sphere with the following density

$$\rho(r) = \frac{\rho_0}{1 + \left(\frac{r}{r_0}\right)^2} \tag{1.8}$$

where ρ_0 is the local WIMP density that can vary in the range (0.2 – 0.4) GeV/c^2 [29] and r_0 is the core radius [30].

Despite its success, the Standard Model (SM) does not contain any particle that could act as the dark matter. The only stable, electrically neutral, and weakly interacting particles in the SM are neutrinos. However, there are two main reasons why neutrinos cannot account for all of the Universe's dark matter

- 1. neutrinos are relativistic, a neutrino-dominated Universe would have inhibited structure formation and caused a "top-down" formation [31];
- 2. neutrinos are ruled out by cosmological observations because they could account only for a small fraction of dark matter [21, 32].

Although the identity of WIMPs remains a mystery, the best motivated and theoretically developed WIMP candidate comes from new theories proposed to extend the standard model. The most promising theory beyond SM is supersymmetry (SUSY)[33], which also yields a viable WIMP candidate called the neutralino or lightest supersymmetric particle (LSP).

1.3 Search for dark matter

The search for dark matter can be performed with three complementary approaches, as schematically represented in Figure 1.4

- production of dark matter at particle colliders;
- indirect detection;
- direct detection.

In this section will briefly describe the first two items, while a whole section will be focused on the third one.

Dark matter can be produced in high energy interactions at particle colliders. Since dark matter does not interact electromagnetically, its presence can only be revealed in events with missing transverse momentum and energy. This search is carried out at the Large Hadron Collider at CERN with the ATLAS [35, 36] and CMS [37, 38] experiments. Those experiments are looking for signatures of new particles produced in collisions especially in the low mass region (< 1GeV).

The indirect detection [39] consists of searching for the annihilation or the decay of dark matter particles. This technique is based on the measurement

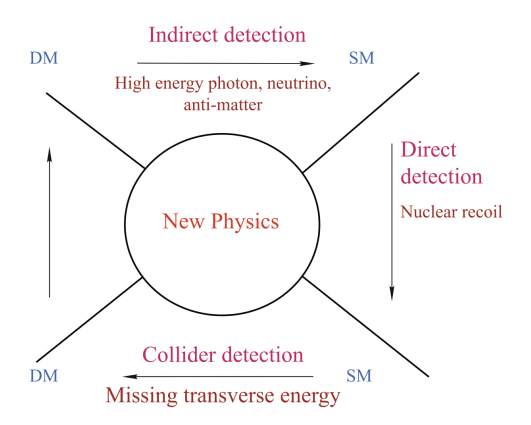


Figure 1.4: Schematic plot to highlight direct detection, indirect detection and collider detection of dark matter. The arrows indicate the direction of reaction. [34]

of the flux of particles produced during the annihilation of WIMPs in the galactic halo or near celestial bodies. Particularly interesting for indirect dark matter search are γ -rays and neutrinos since they preserve spectral information and point back to the source.

Search for γ -rays are usually carried out through experiments on satellite telescopes, as the Earth's atmosphere is opaque to gamma rays; it is noteworthy to mention Fremi-LAT [40] and EGRET [41, 42]; otherwise, ground-based telescopes are used and since the flow of gamma rays decreases rapidly with increasing energy, such detectors are required to have a very large effective area, like HESS [43]. The detection of astrophysical neutrinos generally implies the use of detectors composed of large volumes of water or ice that allow the study of the Cherenkov light produced in the detector medium as the products of neutrino interactions passes through it. This research is performed by experiments such as Ice Cube [44], ANTARES [45] and Super-Kamiokande [46]. Another indirect manifestation of the presence of WIMPs could be through their annihilation with the production of electron-positron pairs. The PAMELA [47, 48] experiment observed an excess of positrons in the range from 10 GeV to 250 GeV, this overabundance was then confirmed by AMS-2 [49] and Fermi [50]. However, there are also other interpretations of the observed signal such as the collision of cosmic rays with the interstellar medium or the production by pulsar [51].

1.4 Direct detection

Direct detection concern the scattering on both nucleons and electrons. Since the level of background is lower for the nucleons, usually direct detection aims to measure nuclear recoils produced by elastic scattering of WIMPs off target nuclei of the detector:

$$\chi N \longrightarrow \chi N$$
(1.9)

where χ is a dark matter particle and N represents the target nucleus. For $10-100~{\rm GeV/c}^2$ WIMP masses a recoil energy in the range $1-100~{\rm keV}$ [29] is expected. The differential recoil spectrum resulting from WIMP interactions can be written as:

$$\frac{dR}{dE}(E,t) = \frac{\rho_0}{m_{\chi} m_N} \int_{v_{min}}^{v_{max}} v f(\mathbf{v},t) \frac{d\sigma}{dE}(E,v) d^3v$$
 (1.10)

where m_{χ} and m_N are dark matter and nucleus masses, rispectively, ρ_0 is the local WIMP density, v is the dark matter velocity defined in the rest frame of the detector and $f(\mathbf{v},t)$ represents the WIMP velocity distribution in the detector rest frame, finally $\frac{d\sigma}{dE}(E,v)$ is the WIMP-nucleus cross section. The velocity distribution is time dependent due to the revolution of the Earth around the Sun and it is usually described by an isotropic Maxwel-Boltzman distribution, which is truncated at velocities exceeding the escape velocity [52]:

$$f(\mathbf{v},t) = \frac{1}{\sqrt{2\pi\sigma}} exp\left(-\frac{v^2}{2\sigma^2}\right)$$
 (1.11)

where $\sigma = v_c \sqrt{\frac{3}{2}}$ is the velocity dispersion with v_c the local circular velocity, $v_c \sim 220$ km/s. This value is averaged from different analyses [53]. For the elastic scattering the transferred momentum is

$$q^2 = 2m_r^2 v^2 (1 - \cos\theta^*)$$

where $m_r = m_{\chi} m_N / (m_{\chi} + m_N)$ is the reduced mass and θ^* is the scattering angle in the center of mass frame. Hence, the recoil energy in the non-relativistic regime is:

$$E = \frac{q^2}{2m_N} = \frac{m_r^2 v^2 (1 - \cos\theta^*)}{m_N}$$
 (1.12)

The minimum velocity of the WIMP that can give a recoil energy E, is obtained for $\cos \theta^* = -1$:

$$v_{min} = \sqrt{\frac{Em_N}{2m_r^2}} \tag{1.13}$$

whereas the maximum velocity, v_{max} , is the escape velocity of the WIMPs in the halo [29]. According to [54] the escape velocity is within the range 498 km/s < v_{max} < 608 km/s and the commonly used value is 544 km/s.

The WIMP-nucleus elastic scattering depends on how the WIMP couples with the nucleon and, in the non-relativistic limit, it can be divided into two classes: the spin-independent (SI) and spin-dependent (SD).

The former represents the simplest case of interaction where the WIMP couples equally with neutrons and protons, the amplitude of each one adds in phase and the scattering results as a coherent process. The latter, instead, takes into account the spin of neutrons and protons. Since coupled nucleons will give a zero contribution to the amplitude, only the non coupled ones will contribute: this is why targets with an odd number of protons or neutrons are needed to detect SD interactions.

For spin independent interactions, the cross-section at zero momentum transfer is:

$$\sigma_0^{SI} = \frac{4m_r^2}{\pi} [Zf^p + (A_Z)f^n]^2$$
 (1.14)

where f^p and f^n are the effective copuling factors of WIMPs on protons and neutrons, rispectively, Z is the atomic number and A-Z the number of neutrons. Usually, $f^p \simeq f^n$ and therefore the cross-section is proportional to A^2 .

Instead for the spin-dependent case the cross-section at zero momentum transfer is:

$$\sigma_0^{SD} = \frac{32}{\pi} G_F^2 m_r^2 \left[a_p \langle S^p \rangle + a_n \langle S^n \rangle \right]^2 \frac{J+1}{J}$$
 (1.15)

where G_F^2 is the Fermi coupling constant, J the total nuclear spin, $a_{p,n}$ are the effective spin coupling of spin with protons and neutrons and $\langle S^{p,n} \rangle$ are the expectation values of the nuclear spin content due to the proton and neutron group.

In order to write the differential cross-section it is necessary to take into account the finite size of the nucleus with the form factor $F^2(q)$ which in the case of SI is commonly described with the Helm parameterisation, while for

SD it is written in terms of spin structure function

$$F^{2}(q) = \frac{S(q)}{S(0)} \tag{1.16}$$

and normalized so that F(0) = 1. The differential cross-section is:

$$\frac{d\sigma}{dE} = \frac{m_N}{2m_r^2 v^2} (\sigma_0^{SI} F_{SI}^2(E) + \sigma_0^{SD} F_{SD}^2(E))$$
 (1.17)

Besides, Earth's motion around the Sun produces a seasonal modulation in the total number of events expected [55]. During July, there is a component of Earth motion around the Sun parallel to the Sun's motion around the galactic center, while in January, this component is antiparallel and reduces Earth's velocity relative to the halo. For this reason there is an annual modulation of the event count rate that shows a maximum in July and a minimum in January.

Directionality is another dark-matter signature which can be employed for its detection as the direction of the nuclear recoils resulting from WIMP interactions has a strong angular dependence [56]. This dependence is clearly evident if the differential rate is written as a function of the angle γ defined by the direction of the nuclear recoil relative to the mean direction of the solar motion

$$\frac{d^2R}{dEdcos\gamma} \propto exp \left[-\left(\frac{(v_E + v_{\odot})cos\gamma - v_{min}}{v_c^2}\right)^2 \right]$$
 (1.18)

where v_E is the Earth's velocity, v_{\odot} the velocity of the Sun around the galactic centre, v_{min} the minimum WIMP velocity and v_c the halo circular velocity.

1.5 Detectors for direct search

In the direct search for dark matter, the elastic scattering induced by a WIMP transfers to the target nucleus an energy that can be detected with three different signals, which depend on the detector technology in use. These effects can be:

- the production of heat (phonons in a crystal);
- scintillation photons due to de-excitation of the target nucleus;

• direct ionisation of the target atoms.

Some experiments involve a single detection channel while others combine two of the three effects mentioned. In the following the focus will be on scintillator crystals, bolometers and liquid noble-gas detectors.

1.5.1 Bolometers

Bolometers are detectors capable of measuring the energy deposited by the incoming particle in form of phonons, i.e. vibrations of the crystal lattice. Phonons produced by the dissipated energy can be separated in thermal and athermal phonons. Thermal phonons can be measured by the induced temperature rise with typically $\Delta T = E/C \sim 1\mu K$, where E is the released energy and C the detector's heat capacity. Athermal ones are a fraction of the initial phonons not at equilibrium and can provide information on the energy and the position of the recoil. In addition to the phonon signal, cryogenic bolometers can also perform particle discrimination exploiting the charge or the scintillation signal.

The CDMS II experiment [57] at Soudan Underground Laboratory is made of nineteen Germanium and eleven Silicon detectors of 230 g and 110 g, respectively. The signal detection is based both on phonon excitation and ionization. This experiment has not found any evidence for an annual modulation of the event rate [58]; this result disagrees in particular with the observation of the CoGeNT experiment which also uses a germanium target [59]. A follow-up experiment is SuperCDMS [60] which currently set the most sensitive exclusion limits at low WIMP masses [61]. The CRESST-II experiment, at LNGS with a detector based on scintillating crystals at very low temperature (mK) [62] used the combination of phonon and scintillation signals to detect the WIMP-nucleus interaction. With a total exposure of 730 kg from 2009 to 2011, it observed an excess of events corresponding to a significance of 4.7σ [63]. In the 2013, after an improvement of the background detection efficiency, with an exposure of 29.35 kg the previous signal was disproved. An exclusion limit was set on spin-independent WIMP-nucleon scattering which probes a new region of parameter space for WIMP masses below 3 GeV/c^2 [64].

1.5.2 Liquid noble-gas detector

Liquid noble-gas detectors, when crossed by radiation, show an high scintillation and ionisation. Currently, liquid argon (LAr) and liquid xenon (LXe) detectors are used as detector media. To distinguish the main background due to γ and e^- interactions (electronic recoils, ER) from the interactions of WIMPs with nuclei (nuclear recoils, NR), two methods can be applied in liquid noble-gas detectors: pulse-shape discrimination (PSD) and charge-to-light signal ratio.

The luminescence in these materials is produced by two different states: the singlet which has a fast decay time (t_f) and the triplet having slow decay time (t_s) . This results in a differentiation of the shape between ER and NR because for the first t_s is prevalent whereas for the second t_f . This technique gives large separation power in liquid argon since $t_f \sim 6$ ns and $t_s \sim 1.6 \mu s$ [65]. However, pulse shape discrimination provides a good separation only for a large number of measured photons and therefore, a higher energy threshold has to be considered. In liquid Xenon, the values for the decay constants are too close to each other, $t_f \sim 4$ ns and $t_s \sim 22$ ns [66], giving less rejection power.

The above mentioned liquid noble-gas detectors can work with two different technologies:

- single phase if the noble element is used only in the liquid state;
- double phase when both the gaseous and liquid state of the element are employed.

Single phase detectors consist typically of a spherical target, containing the liquid medium, surrounded by photo-detectors. The main advantage is the full coverage with photo-multipliers (PMT) which results in a larger light output compared to detectors which are only partially covered. The distribution and timing of the photons at the PMT can be used to determine the position of the event.

Double phase detectors allow to detect both the scintillation light and the charge signal from ionisation produced by energy deposition [67]. In this case the charge-to-light ratio depends on the particle type and allows to separate signal-like events from background. This category of detectors has a cylindrical shape with PMTs located on top and bottom surfaces. Their task is to detect both the prompt light signal and ionised electrons. Ionised electrons

are drifted upwards to the liquid-gas surface and amplified via proportional scintillation in the gas phase [68]. Therefore, double phase detectors are operated as a Time Projection Chambers (TPCs). The difference between the scintillation signal and the charge signal provides the z position and the information provided by PMT allows to identify the x-y plane position, thus allowing the reconstruction of the event.

Experiments using liquid-Ag in single-phase are DEEP [69] and CLEAN [70] at the SNO laboratory in Canada, whereas in Japan, at the Kamioka Observatory, the XMASS experiment [71] employs the same technology with liquid-Xe.

The first experiment using liquid-Ar in double-phase was WARP [72], at the LNGS laboratory. Other dual-phase experiments with Argon are: the DarkSide [73] which has reached 50 kg of active mass and is planning a multi-ton detector, ArDM [74] detector that was first tested at CERN and then moved to the Canfranc underground laboratory. Experiments using double-phase detectors are XENON at LNGS with 1ton active mass[75], LUX at the Sanford underground laboratory in the US, operates a LXe TPC with an active mass of 250 kg [76]; ZEPLIN [77], which operated at the Boulby underground laboratory, achieving a high separation between signal and background by using a flat detector geometry allowing to increase the electric field in the liquid to a maximum of almost 9 kV/cm and PandaX [78] which is operated at the Jin-Ping underground laboratory initially with a target volume of 120 kg, then increased to 500 kg. [79]. LUX and ZEPLIN experiments have joined to build the multi-ton LZ detector hosting about 7 tons of liquid xenon in the target volume [80, 81].

1.5.3 Scintillator

When particles pass through a scintillating material, atoms or molecules of the medium are excited and the subsequent de-excitation causes the emission of photons. For dark matter research NaI(Tl) and CsI(Tl) crystals are mainly used. Usually, such detectors are used for acquisitions over several years but in these crystals it is possible to acquire only the scintillation signal, thus, it is not possible to discriminate between particles, except to exclude multiple hits in different crystals, since WIMPs are expected to produce only one hit. To identify dark matter in these experiments annual signal modulation can be used, but a sufficiently low background is required, which can be obtained with high purity crystals and active vetoes.

The DAMA experiment and its successor DAMA/LIBRA, located at the LNGS underground laboratory is using ultra low-radioactive NaI(Tl) cristals to detect dark matter. This experiment has collected 1.33 ton \times y exposure showing an annual-modulated single-hit rate in the energy range (2-6) keV_{ee} (keV electronic recoil equivalent). Its maximum is compatible within 2σ CL with the expected phase for dark matter interactions [56] and the significance of this signal is at 9.3 σ over a measurement of 14 annual cycles [82]. In addition, recent results of DAMA/LIBRA phase2 have confirmed the 9.5 σ annual modulation of CL in the 1-6 keV range.

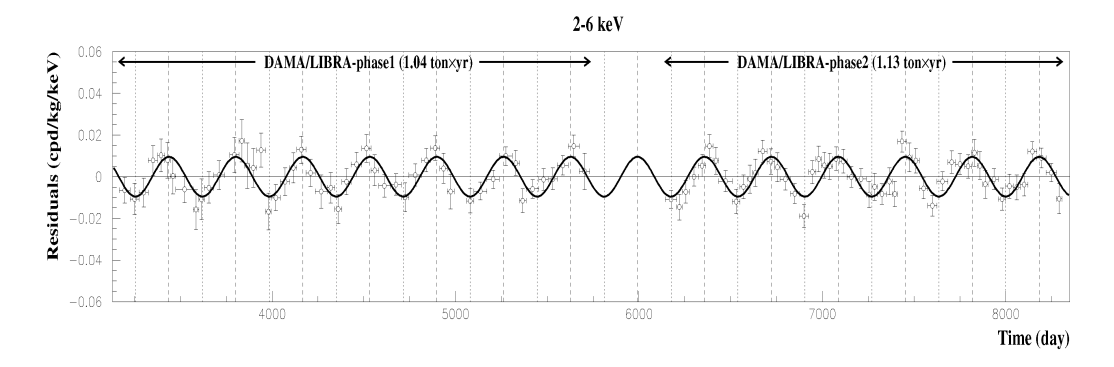


Figure 1.5: Residual rate for single-hit scintillations measured by DAMA/LIBRA-phase1 and DAMA/LIBRA-phase2 in the (2-6) keV energy interval [83].

If the DAMA signals are interpreted as due to the WIMP-nucleus scattering, there will be two possible regions: at $(10 - 15) \text{ GeV/c}^2$ for scattering off sodium and $(60 - 100) \text{ GeV/c}^2$ for scattering off iodine [84].

The signal observed by DAMA has not actually been confirmed by other experiments and moreover, the annual modulation can be explained in several ways that exclude dark matter [85]. The signal could be related to atmospheric muons, whose rate is modulated annually due to temperature variations in the stratosphere [86], or to combinations of muons and modulated neutrinos caused by the varying Sun-Earth distance [87] or by the seasonal variation of the neutron background [88].

In order to perform independent cross-check of the DAMA signal, several experiments, were proposed. The SABRE experiment [89] was supposed to place two similar detectors based on NaI(Tl) crystals, one at the LNGS in

the northern hemisphere and another one in the southern hemisphere at the Stawell Underground Physics Laboratory (SUPL), Australia. The double measurement could allow to reduce the background due to muons that have an opposite seasonal modulation in the two hemispheres. They have recently reported a difficulty in producing pure crystals.

1.6 Direct detection experiment general result

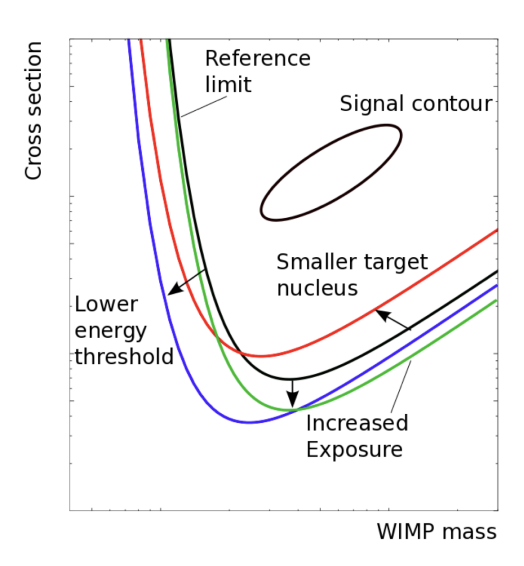


Figure 1.6: Typical representation of the results obtained by direct dark matter detectors: cross-section with matter as a function of the WIMP mass. The black line shows a limit and signal for reference, while the coloured limits illustrate the variation of the upper limit due to differences in the detector design or properties. [52]

Direct dark matter experiments usually represent their results in the WIMP mass cross-section plane as shown in Figure 1.6. Closed lines represent regions where an eventual observation is claimed while open lines represent the upper limit if no signal is detected. Different factors influence the sensitivity curve of an experiment:

• a lower energy threshold corresponds to a sensitivity at lower WIMP masses (blue line);

- a longer exposure time corresponds to a lower explored cross-section (green line);
- smaller target nuclei reduce the overall sensitivity (red line).

Furthermore, other effects may play a role in detector sensitivity such as uncertainties in hypothetical models and/or systematic errors in experimental procedures.

The current spin-independent and spin-dependent landscapes, where strict upper limits exist for higher mass WIMPs are shown in Figure 1.7a and 1.7b, 1.7c respectively. The hints for WIMP signals measured by DAMA/LIBRA and CoGeNT are represented as closed contours while the cross-section limits provided by other experiments are reported as curves in the parameter space.

Since detectors for the direct dark matter search are increasing their sensitivity, reaching masses of the order of tons, they will begin to encounter what is known as the "neutrino floor". The latter is due to Solar, atmospheric and diffuse supernovae neutrinos which undergo coherent scattering off nuclei. Neutrino induced recoils cannot be distinguished from those induced by WIMP.

1.7 Directionality

Detectors capable of measuring the direction of WIMP-induced nuclear recoils can provide an unambiguous identification of dark matter and at the same time allow to overcome the limit imposed by coherent neutrino scattering. The motion of the Solar System through the galaxy generates an apparent wind of dark matter particles, as observed in the Earth's frame, blowing from a preferred direction that corresponds approximately to the Cygnus constellation as shown in Figure 1.8.

Since main background sources are expected to be isotropic, the detection of a signal peaked in the direction of the Earth's motion could provide a clear proof of the galactic origin of dark matter.

Directional detectors are supposed to measure the direction of WIMP-induced recoils with a good angular resolution to discriminate them from the isotropic background.

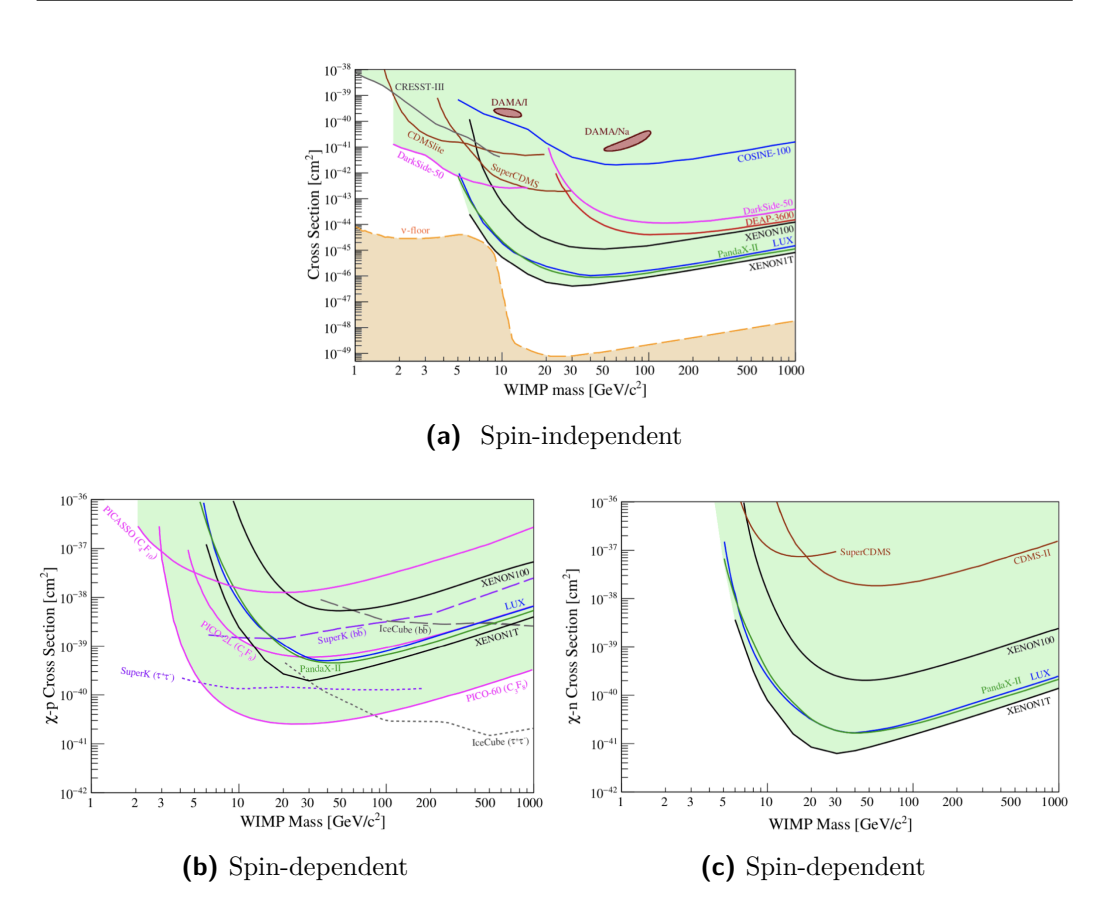


Figure 1.7: Signal indications (closed curves) and exclusion limits (open curves) for WIMP mass in (a) spin-indipendent case and spin-dipendent case: (b) WIMP-proton interactions, (c) WIMP-neutron interactions.[90]

So far, low-pressure gas detectors, as NEWAGE [91], DMTPC [92], MIMAC [93], DRIFT [94], D3 [95] have been used where expected track lengths of WIMP-induced recoils are of the order of the millimeter. However, such detectors cannot easily increase their mass up to the ton-scale as the most competitive experiments.

Experiments with a dense target such as ADAMO [96], DCaNT [97] and SCENE [98] are not able to reconstruct the track of the recoil but are able to measure its angle with a specific direction for each detector. In particular: the axis of the crystal in ADAMO, the axis of the nanotube in DCaNT and the direction of the electric field in SCENE.

For a solid detector, expected track lengths of WIMP-induced recoils are

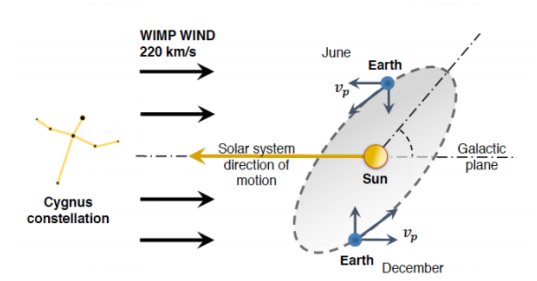


Figure 1.8: Schematic representation of the Earth motion through the Milky Way.

of the order of few hundred nanometers, making their reconstruction very challenging. The use of nuclear emulsions as a tracking detector with the highest spatial resolution could allow both to easily scale the detector mass and to reconstruct tracks in the sub-micrometric range.

1.7.1 Nuclear Emulsion

Nuclear emulsions are made of silver halide crystals embedded in a gelatine matrix. When ionizing particles pass through it, energy is released to silver bromide crystals leaving a latent image. The size of silver halide crystals in standard emulsion ranges from 0.1 μ m to 1 μ m.

The use of nuclear emulsions [99] for the study of particles, originated in 1896 when Becquerel first observed the blackening of photographic plates on contact with uranium salts. Such emulsions allowed the discovery of numerous particles starting from 1947, when Powell, Lattes and Occhialini [100] observed events in which a heavy meson (π) decayed into a light and penetrating lepton (μ) .

Subsequently, the birth of the Emulsion Cloud Chamber (ECC) technique [101] made by the alternation of nuclear emulsions and passive material, and the development of automatic scanning systems allowed the study of cosmic rays to observe the first mechanisms of production and decay of particles containing the charm quark. The first experiment in which large-scale automatic scanning systems of nuclear emulsions were used is CHORUS [102], but it is the OPERA experiment, which studied neutrino oscillations $\nu_{\mu} \rightarrow \nu_{\tau}$ [103], that marked a turning point in the use of emulsions in high

energy physics.

The use of a solid target for directional dark matter searches would overcome the limitation of gaseous detectors, due to low scalability to large masses, thus allowing to reach a high sensitivity in low cross-section sectors of the SI case. However, in a solid medium, the track of the WIMP-scattered nuclear recoil will have a path length of the order of a few hundred nanometers. Therefore nuclear emulsions with smaller crystals and an innovative optical scanning system are required to observe the signal. NEWSdm will be the first experiment to search for dark matter with a directional approach using a solid target made of a new generation of nuclear emulsions, as it will be described in the following chapter.

Chapter 2

The NEWSdm experiment

The NEWSdm experiment proposes an innovative approach for WIMP search with directional measurement. Key elements to fulfil this challenging task are the production of new generation nuclear emulsions, the development of new readout systems and the background rejection. All these aspects will be discussed in detail in the present chapter.

2.1 Nano Imaging Trackers

As mentioned in the previous chapter, nuclear emulsions have been widely used as vertex and tracking detector in the search for new particles with unrivalled spatial and angular resolution. However, standard emulsions used for the OPERA experiment use crystals with ~200 nm size which are not suitable for dark matter search, since WIMP induced nuclear recoils produce tracks a few hundred nanometers long.

Since 2007 an R&D activity was performed at Nagoya University leading to the production of new emulsion films with crystals from 80 nm down to 20 nm. In particular, the following nuclear emulsions were produced:

- (i) Nano Imaging Trackers (NIT) with crystals of 44.4 nm of diameter and a linear density of 11 crystals per μ m [104];
- (ii) Ultra-Nano Imaging Trackers (U-NIT) with crystals of 24.8 nm of diameter and a linear density of 29 crystals per μ m [105].

These new kind of emulsions make it possible to reconstruct trajectories with path lengths down to 100 nm when analyzed with an optical microscopes

with enough resolution. Distributions of the crystal diameter measured with an electron microscope for NIT and U-NIT emulsions are shown in Figure 2.1.

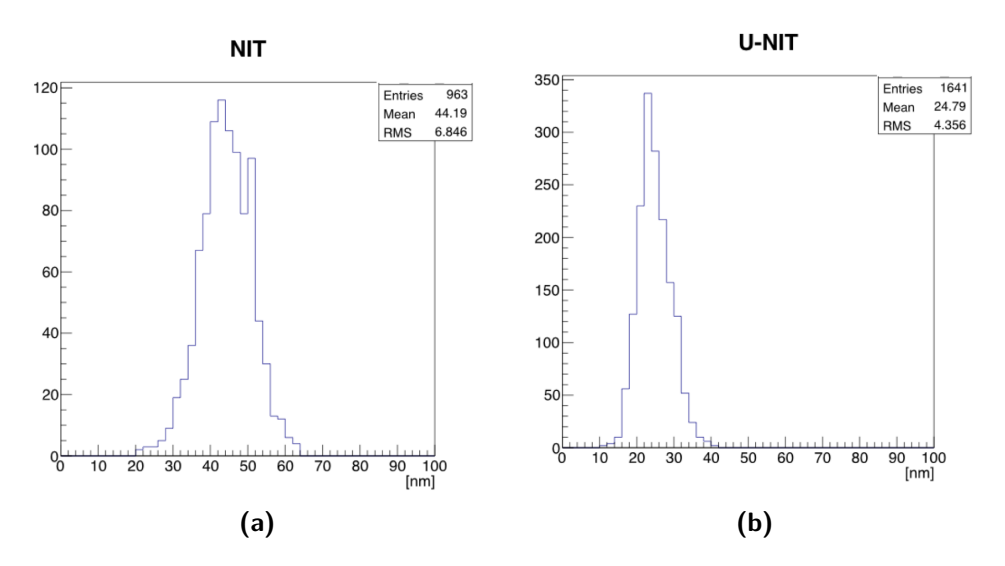


Figure 2.1: Distribution of the crystal diameter measured with an electron microscope for NIT (a) and U-NIT (b) emulsions. [106]

The production of NIT crystals and emulsion films is based mainly on three steps using a dedicated machine:

1. AgBr formation process, mixing in a thermostatic bath $AgNO_3$ and NaBr according to the following reaction

$$AgNO_3 + NaBr \longrightarrow AgBr + Na^+ + NO_3^-$$
 (2.1)

thus forming AgBr crystals. Furthermore, polyvinyl alcohol (PVA) and NaI are added to ensure the uniformity of the crystal size and to increase quantum activation efficiency;

- 2. desalination process: AgBr crystals are mixed with gelatin and the residual ions Na^+ and NO_3^- are extracted by a reduction process. Moreover, in order to have an uniform distribution of the crystals, this mixture is centrifuged at a speed of 1000 rpm and a temperature of 50°C;
- 3. *pouring process*: the emulsion gel obtained is mixed with ultra-pure water and poured on a rigid plastic or glass support.

Constituent	Mass Fraction
AgBr-I	0.78
Gelatin	0.17
PVA	0.05

Table 2.1: Constituents of NIT emulsions.

Element	Mass Fraction
Ag	0.44
Br	0.32
I	0.019
\mathbf{C}	0.101
O	0.0.074
N	0.027
Н	0.016
S	0.003

Table 2.2: Chemical composition of NIT emulsions.

The mass fraction of NIT constituents and the chemical composition of NIT emulsions are shown in Tables 2.1 and 2.2.

The presence of both heavy nuclei, as silver and bromine, and light nuclei, as carbon, oxygen and nitrogen, allow to have a good sensitivity to high and low WIMP masses. WIMPs with masses of the order of $100~{\rm GeV/c}^2$ and higher prefer heavy Ag and Br atoms at a target, while WIMPs with masses of the order of $10~{\rm GeV/c}^2$ and below prefer lighter nuclei since the energy transferred is maximum when both particles in the scattering process have similar masses.

After having packed NIT films into under vacuum in Aluminum foil bags, NIT films are ready to be exposed. After the exposure, in order to analyze emulsions with fully automated optical microscopes, the *development process* is performed. Through this process, the latent image contained in an emulsion is made visible by the reduction of silver ions in the silver halide crystal to metallic silver. Silver halide crystals without a latent image center are not modified during the development process and are then dissolved by a fixing solution.

2.2 Layout of the NEWSdm detector

The NEWSdm experiment proposes an innovative approach for the directional detection of dark matter using NIT emulsions that act both as a target and as a tracking device. NIT emulsion allow to reach a very high spatial resolution and, in addition, a solid-state detector does not suffer from any limitations for scaling up in mass.

The bulk of NIT is surrounded by a sphere of polyethylene acting as a shield against external backgrounds. The emulsion target will be enclosed in a sealed plexiglass box maintained in High Purity (HP) Nitrogen atmosphere in slight overpressure with respect to the external environment to prevent radon contamination. The actual configuration foresees the use of 1m-thick polyethylene shield. A schematic representation of the detector layout is reported in Figure 2.2.

Since the average WIMP wind is expected to come from the Cygnus constellation, the detector will be placed on an equatorial telescope to compensate for the daily rotation of the Earth and keep the orientation fixed towards the expected incoming direction.

Besides, NIT films will be placed always parallel to the galactic plane.

The detector is usually mounted on two axes:

the Polar Axis, parallel to the Earth's axis of rotation, pointed toward the north celestial pole and rotated at a constant speed opposite to the Earth's rotation to cancel out the apparent motion of celestial objects;

the Declination Axis, perpendicular to the polar axis, points towards a fixed position of the sky e.g. the constellation of the Cygnus.

Both axes will be equipped with precise encoders to constantly control the position of the mechanics with high precision and the direction will be maintained with an accuracy better than 1 degree.

A detector of 10 kg of NIT can be made of thin films of 50 μ m assembled in a block of 389 planes with a surface of 25×30 cm² and a height of 20 cm. As shown in the Figure 2.3, the 2D track reconstruction is performed in the plane (XY) parallel to the nuclear emulsion films with the x-axis opposite to the Cygnus constellation direction. In this reference system the angle of the nuclear recoil is defined as the angular difference between its projection in the xy plane and the x-axis.

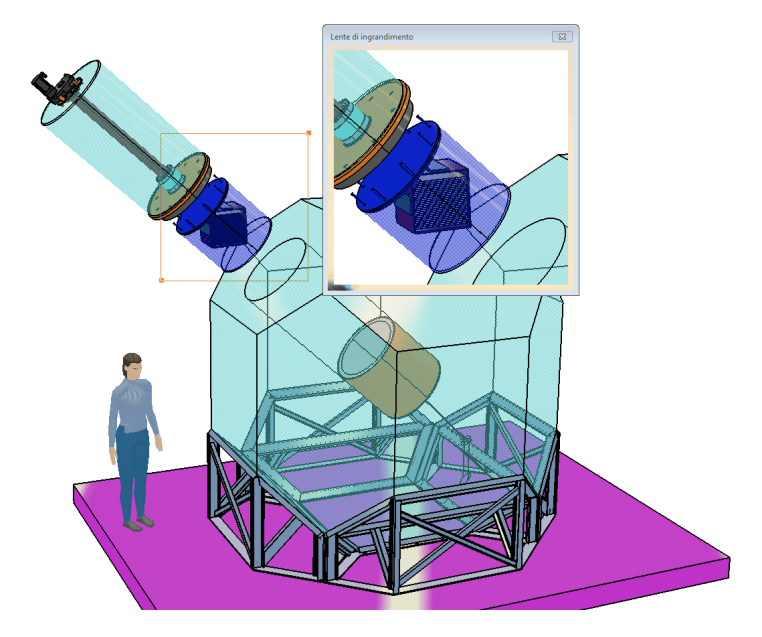


Figure 2.2: Schematic representation of the experimental set-up for an exposure of 10 kg per year. The equatorial telescope is represented by the gray arm, the shield of 1 m polyethylene by the cyan cylinder and the NIT stack in blue.

The angular distribution of WIMP-induced recoils is expected to be Gaussian and peaked at zero, with standard deviation increasing as the mass of the WIMP increases. The lighter the WIMP, the stronger the angular anisotropy. Indeed, for low WIMP masses the recoil energy is rather low and the track length threshold selects only a small fraction of the spectrum, characterised by the largest fractional energy transfer to the recoiled nucleus.

The detector sensitivity is strongly dependent on the minimum detectable track length which depends on the kinetic energy of the scattered nucleus.

2.2.1 Technical test

A technical test with 10g of NIT emulsions was done to measure the detectable background from environmental and intrinsic sources. The information of a negligible background allows the construction of the pilot experiment with a

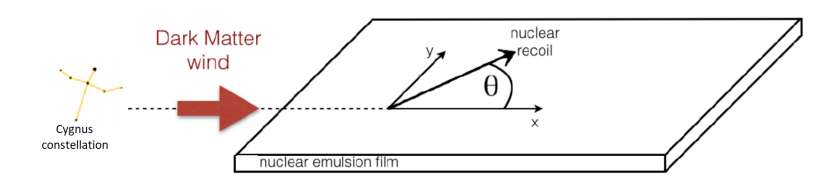


Figure 2.3: The 2D reconstruction is performed in the xy-plane. The x-axis is directed opposite to the Cygnus constellation and θ is the angle between the x-axis and the projection of the nuclear recoil in the xy-plane. [107]

ten kilogram per year exposure mass capable to explore the DAMA region. The experimental setup was installed in February 2017 in the Hall B of the LNGS. A schematic picture of the shielding and the picture of the experimental setup installed in Hall B are reported in Figure 2.4. NIT emulsions have been stored in a cryostat (LAUDA RP 890C) to ensure the required temperature (below -40°C) to reduce thermal excitation and fading. The shielding is made of 40 cm thick polyethylene plates, to absorb environmental and cosmogenic neutrons, and 10 cm thick lead bricks, to absorb environmental gamma.

2.3 Expected background

In order to unambiguously identify WIMP-induced recoil, all the physical sources and instrumental effects that may influence this measurement should be known and reduced. NIT emulsions are insensitive to minimum ionizing particles (MIP) since they do not produce enough electrons to form a latent image [108]. Signal-like events are characterized as a sequence of at least two or more aligned grains with a distance of less than 100 nm, therefore a background event can mimic the signal if it produces at least two grains in NIT.

Background sources for the NEWSdm experiment can be divided into three main categories: (i) external backgrounds from neutrons, γ -rays and muons, that can be reduced placing the detector underground and using a suitable shield; (ii) intrinsic radioactivity of detector components, that is an irreducible

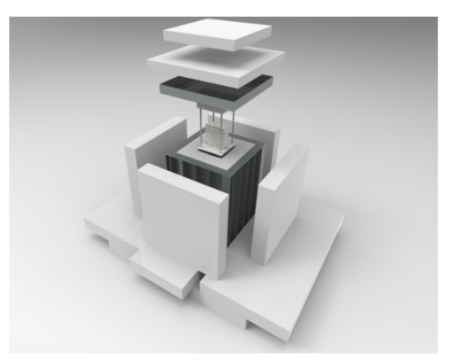




Figure 2.4: Schematic (left) and real (right) picture of the shielding for the technical test installed in underground Gran Sasso laboratory.

source of radiation and can be reduced only by using very high purity materials for the construction of the detector and of the shield; (iii) the instrumental background, not linked to any physical source but related to the emulsion film production, development and analysis processes.

2.3.1 External background

External background sources affecting underground laboratories are: environmental gammas and neutrons which essentially depend on the materials inside the experimental hall and the surrounding rock; muon and cosmogenic neutron flux which strongly depend on the site depth; diffuse neutrino background which becomes particularly dangerous for a ton-scale mass experiment.

Environmental gammas originate from decays in Thorium and Uranium chains whose products are strong gamma emitters, the energy of those γ -rays ranges from tens of keV up to 2.6 MeV [109]. The main interaction process of γ -rays with matter are the photoelectric effect, dominant for low energies, up to a few hundred keV, the pair production, dominant above a few MeV, and the Compton scattering which is the most probable process for the energies in the range between the other two. All of them produce electrons with energies of few keV which can produce a latent image on the surface of AgBr crystals. Since the environmental gamma flux at LNGS is 0.35 cm⁻²s⁻¹ [109] it can be

suppressed using shields made of dense materials, such as lead and copper, or large water tanks.

Neutrons induced by the environmental radioactivity at LNGS halls are produced by the spontaneous fission and the (α, n) reaction, whose energy is of the order of the MeV. The flux at LNGS is 8.7×10^{-7} cm⁻²s⁻¹ [110]. The neutron background from environmental radioactivity can be reduced by using a passive shield, usually made of hydrogen-containing materials since the most effective moderators are elements with low atomic number. Since mean free paths of fast neutrons in inexpensive materials such as water, concrete, and paraffin, are of about tens of centimeters, thicknesses of 1 m or more are required to slow down neutrons. Once neutrons have been moderated, they can be absorbed through capture reactions, that are enhanced by adding elements with high neutron capture cross-section, as boron and lithium. Such elements can either be homogeneously mixed with the moderator or can be present as an absorbing layer near its inner surface.

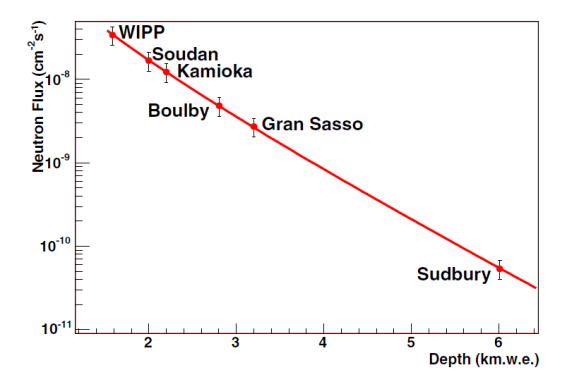


Figure 2.5: Total muon-induced neutron flux at different underground sites [111].

To reduce the number of muon-induced neutrons dark matter detectors are usually placed in underground laboratories. Cosmogenic neutrons with an energy spectrum extending up to the GeV are induced by muons penetrating underground through the rock, hence the yield depends on the depth of the underground laboratory. As shown in Figure 2.5, the deeper the site, the higher the reduction of the cosmogenic neutron flux. LGNS are located at 1.4 km under the mountain, an equivalent vertical depth of (3.1 ± 0.2) km water equivalent (k.w.e.). At these depths, the muon flux amounts to 1 muon

 $m^{-2}h^{-1}$, six orders of magnitude lower than the value measured at the surface, and the mean muon energy is of about 250-300 GeV [112]. There are three dominant processes of neutron production by muons underground:

- muon electromagnetic interaction with a nucleus, producing a nuclear disintegration and thus neutrons (direct muon spallation) [113];
- production of an electromagnetic cascade, in which high energy photons can cause spallation reactions;
- production of hadronic cascade, in which generated hadrons $(\pi^{\pm}, K^{\pm,0}, \mathbf{n}, \mathbf{p})$ can also cause spallation reactions [114].

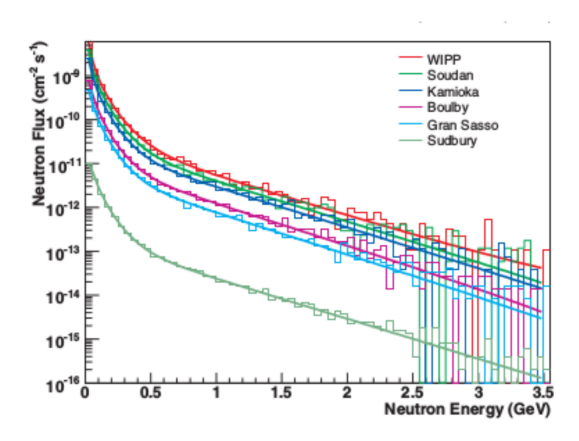


Figure 2.6: The differential energy specttrum for muon-induced neutrons at different underground sites [111].

The muon-induced neutrons energy spectrum extends up to several GeV and can penetrate to significant depth both in the surrounding rock and in the detector shielding materials as can be seen in Figure 2.6 from the FLUKA simulation [115]. The total muon-induced neutron flux emerging from the rock in the cavern at LNGS is 7.3×10^{-10} cm⁻²s⁻¹ and the average energy is 91 MeV [111]. Cosmogenic neutrons can be partially reduced by shielding the detector with several meters of hydrogen-containing materials. Furthermore, muons interacting in the shielding produce additional neutrons which can be rejected in the detector only via topological cuts.

Detectors for direct dark matter search are sensitive only to energy depositions but are unable to reconstruct the direction of the impinging dark matter particle. In scaling up their mass, they are becoming sensitive to solar, atmospheric, and diffuse supernova neutrinos. The neutrino-nucleus coherent scattering produces recoils which cannot be distinguished from dark matter interactions; therefore it is an irreducible background for such experiments whose sensitivity will be limited by the so-called neutrino floor.

2.3.2 Intrinsic background

The intrinsic background induced by the contamination of the materials is extremely dangerous for the observation of rare events since it is produced inside the detector without the possibility to be shielded. Thus, it is crucial using highly purified materials for detector and shield. The presence of the ¹⁴C isotope which undergoes β -decay and radiogenic neutrons from the decays of long-lived radioisotopes (e.g. U, Th) in NIT constituents is an intrinsic background sources for the NEWSdm detector.

With proper chemical treatments, it is possible to optimise the emulsion response, in terms of the number of latent images produced per unit path length (i.e. sensitivity), thus reducing the NIT sensitivity to the electrons [116]. A recent study carried out in Japan has shown that the emulsion sensitivity to electrons is strongly reduced at low temperatures [117]. Since γ -rays produce electrons when interacting with matter this cryogenic approach would present the big advantage of making also the γ -induced background negligible. The Collaboration is also exploring the possibility to cancel out the electron background from intrinsic ¹⁴C content, by replacing organic gelatine with synthetic polymers. Moreover, the electron discrimination can be improved by exploiting the different response of the resonant effect of the polarized light.

Radiogenic neutrons produced in the detector due to its intrinsic radioactive contaminants would be responsible for an irreducible neutron yield. Starting from the U and Th activities of the emulsion and measured with Inductively Coupled Plasma Mass Spectrometry (ICP MS) [118] and with γ -spectrometry, the neutron yield has been estimated through a dedicated MC simulation based on the SOURCES code [119] at a value of (1.2 ± 0.4) neutron yr⁻¹kg⁻¹. The neutron energy spectrum, as calculated with SOURCES, was then used as the input for a GEANT4-based simulation to estimate the fraction of neutrons interacting in emulsion and laying in the signal region. The detectable neutron-

induced background would be 0.06 yr⁻¹kg⁻¹ [120].

2.3.3 Instrumental background

The instrumental background is not related to physical interactions between incoming particles with the target nuclei and it is due to: (i) dust particles which are formed mainly during the production process of emulsion when not done in a clean room; (ii) fog grains produced by the thermal excitation. These sources of background are generated during the gel production and in chemical treatments. The current dust level is about 5×10^{-2} grains/ $(10\mu \text{m})^3$ but it can be strongly reduced by operating the NIT production in a clean room. Moreover, dust grains usually show very irregular shapes or brightness saturation; thus they can be discriminated during the analysis by applying appropriate selections. The probability of random coincidences of two or more fog grains can mimic a WIMP-induced nuclear recoil. The current level of fog density in NIT samples is about 0.1 grains/ $(10\mu \text{m})^3$. The number of tracks produced by chance coincidences depends on the minimum number of grains required to build a track (2) and increases with maximum allowed gap between two consecutive grains in a track. To achieve a negligible background induced by fog grains, a fog density of 10⁻³ grains per 1000 cubic micrometer is required [106]. Several studies are ongoing to lower the fog density level: (i) the use of purified gelatin that makes it possible to reduce by one order of magnitude the current fog density level; (ii) operating with a detector at low temperature to decrease the thermal excitation. Moreover, the resonance effect of polarised light can help distinguish between events due to fog and those due to the signal.

2.4 Optical microscope

After the exposure and the development, in order to analyze the whole target volume over a time scale comparable with the exposure time, it is necessary the use of a fully automatic high-speed scanning system.

These read-out systems have focal lengths of the order of one micron and are capable of moving continuously the focal plane allowing the scanning of the whole emulsion thickness and provide a 3D recontruction of the tracks. As a consequence, we obtain a series of tomographic images captured at different equally spaced depth levels. The images are digitized, converted to grayscale

and analyzed to recognize aligned cluster sequences forming the 3D structure of a track.

The large data flow from fast digital cameras requires high hardware performance, image processing and efficient computational algorithms.

Optical microscopes for automatic scanning of nuclear emulsions are based on the European Scanning System (ESS) framework [121].

The first prototype of the ESS made in 2004 in the laboratories of Naples reached a speed of $20 \text{ cm}^2/\text{h}$ and with a spatial resolution of about 1 μm and an angular resolution of about 1 mrad.

The microscope of the ESS consists of:

- a rigid support table capable of dampening any vibrations;
- scanning plate consisting of two motors that allow the displacements in the horizontal plane (X, Y);
- glass plate placed above the scanning plate, used as a support for the nuclear emulsion placement. This plate is equipped with an air intake system that allows the adherence of the emulsion;
- a granite arm supporting the lens;
- a focusing plate mounted vertically (in the Z plane) on the granite arm.
- digital camera installed on the vertical plate useful for the acquisition pictures.
- illumination system located below the scanning plate.

By implementing LASSO software modules on this hardware configuration, two different methods can be applied to the scanning system: stop and go (SG) and continuous motion (CM). With the SG mode the scanning speed could not exceed 24 cm²/h limited by the mechanical performance of the horizontal motion stage of the microscope, while with the CM mode it is possible to exceed this limit and reach the scanning speed of 40 cm²/h with the same hardware [122, 123].

The SG mode is the basic scanning technique used by all fast automatic scanning systems. Data acquisition is performed during movement along the vertical axis while the horizontal axes remain static. A work cycle lasts 180 ms, where 55 ms is spent on frame grabbing and up to 125 ms to reach the

next position in the view. This includes the time required for acceleration, horizontal displacement, deceleration, and vibrations to discharge. With the LASSO system the hardware speed limit of $24~{\rm cm}^2/{\rm h}$ is reached by optimising the work cycle reduced to $150~{\rm ms}$.

In the CM mode the images are grabbed in a constant movement along both vertical and horizontal directions, without stopping the stage. In this case the reset time is no longer determined by a horizontal movement but only by the vertical movement, i.e. the time required for a vertical axis to return to its original position. The vertical reset time of the ESS is 25 ms which allows to reduce the work cycle to 80 ms thus the scanning speed is two times faster [124]. When using the CM mode the stack of frames is inclined and no longer vertical as in the SG case. Therefore, data processing is more sophisticated, as most tracks will cross neighboring views as clusters belonging to the same track appear in different positions within an image. Therefore, processing must take into account the effects of optical distortion, vibration and view misalignment.

The work cycle of the ESS in SG mode is characterised by two phases: (1) DAQ movement and (2) reset movement. During the first phase, a set of images is acquired with the lens moving at a constant speed (v_z) proportional to the camera frame rate (f) and the sampling distance between two consecutive frames acquired (s) is defined as $v_z = sf$. The fastest camera frame rate and the largest possible sampling distance are chosen to increase the lens speed. The maximum sampling distance is, however, limited by the focal depth of the lens. Choosing lenses with a greater focal depth will allow a larger sampling range to be used but, at the same time, will produce images with shadows from distant grains and, therefore, increase the processing load and decrease purity by raising the combinatorial background level. During the reset movement the lens is moved to the next field of view (adjacent in XY). This represents the dead time of a scanning system where no images are captured. Then, the reset movement is performed at maximum possible speed and acceleration compatible with the stage performances.

The scanning speed could be improved using a wider field of view since a same area would be covered in shorter time. To increase the field of view without losing image quality, a lens with a lower magnification is used together with a camera with a smaller sensor pixel size and therefore a larger number of pixels. Smaller sensor pixels are needed to maintain the pixel-to-micron ratio at the same level ($\sim 0.3~\mu \text{m/pixel}$, usually called optical pixel size) allowing the use of existing algorithms for image processing.

The LASSO [123] software, used for data collection and track reconstruction, has a modular structure which makes it flexible to update the system following technological progress. The hardware components with the best features for a new generation of high-speed microscopes have been chosen.

In recent years, a research and development programme aimed at improving the performance of the ESS has been carried out by INFN teams, leading to prototypes with improved scanning performance by an order of magnitude, reaching a speed of almost $200 \text{ cm}^2/\text{h}$ [125]. Ongoing studies of the novel Inclined Motion scanning techniques coupled with multiple camera setups show the potentiality to increase the ESS performance by one or two orders of magnitude reaching scanning speeds of at least several thousands cm²/h [126]. Moreover, a new system (the Super-Ultra Track Selector) is under development in Japan, which aims to increase the scanning speed up to 5000 cm²/h [127].

2.4.1 Super-resolution microscope for dark matter search

To reach the sensitivity competitive with other dark matter experiments, the reconstruction of track lengths down to 100 nm is an important requirement [128].

This could take place with an X-ray microscope, but this choice would lead to a significant slowing down of the analysis phase. To avoid these limitations, a super-resolution optical microscope was developed in Napoli which exploits the local surface plasmon resonance (LSPR) phenomenon. This optical effect occurs when the wavelength of the incident light is comparable with the size of conductive nanoparticles (Ag grains) dispersed in a dielectric medium (organic gelatin) [129]. A picture of one of that microscopes assembled in Naples is shown in Figure 2.7.

The optical system is composed of:

a high magnification(100×) and high numerical aperture (N.A. = 1.45)
 Nikon Oil Objective Lens, Plan. Apo. which provides good image
 flatness over the entire field of view, with corrected chromatic aberration
 over the entire visible spectrum. The larger numerical aperture and
 magnification are used to optimize the response near the optical limit
 (~ 190 nm);

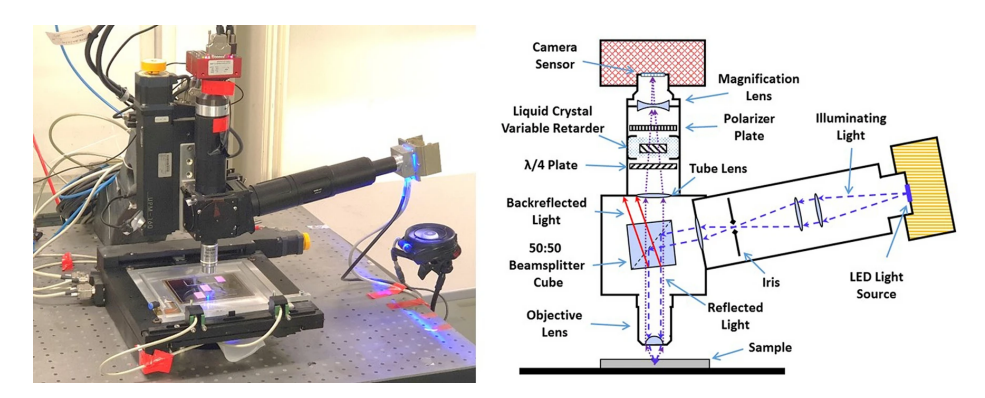


Figure 2.7: A picture of the developed microscope prototype (left) and the technical scheme of its setup (right). [130]

- A 4 Megapixel resolution high-speed camera with a field of view of $65 \times 48 \ \mu\text{m}^2$ and a digital resolution of $\sim 27 \ \text{nm/pixel}$ is placed at the end of the optical tube;
- epi-lighting mode which provides illumination and detection on one side of the sample (by reflection) in order to further decrease the amount of light entering the lens and increase the contrast. The illuminating light source is a UV LED with $\lambda = 406$ nm;
- liquid crystal polarization rotator coupled with a linear polarizing filter used to rotate the polarization state of an input beam linearly polarized through more than 180°, to take advantage of the polarization dependence of the LSPR effects.

The optical resolution of the microscope is estimated to be 207 nm, the angular resolution, measured through the elliptical fit of grains belonging to a long tracks, is 235 mrad (13°). The accuracy position in both coordinates in the emulsion plane is about 10.5 nm [129].

Another microscope equipped with a color camera (Mikroton EoSens 4CXP MC-4087) was assembled to exploit the LSPR effect when different wavelengths are used.

The longer nano-rods (120 nm) show a red shift of the resonance wavelength while the shorter ones (80 nm) show a blue shift (see Figure 2.8). A large energy loss of a particle usually occurs soon before it is absorbed in a material (Bragg peak). Grains belonging to the end of a track are expected to be

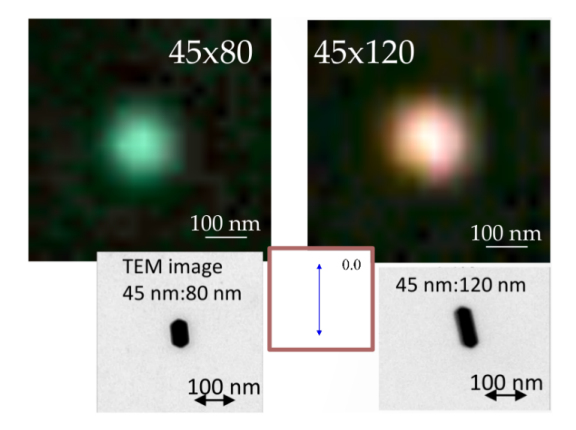


Figure 2.8: Optical microscope with color camera (top) and TEM (bottom) images of nano-rods of $45\times80 \text{ nm}^2$ (left) and $45\times120 \text{ nm}^2$ (right) [106].

seen with a red nuance since larger energy loss results in an higher ionizazion which increase the grain size. This technique is expected to allow for head-tail discrimination in NITs.

2.5 Candidate Selection

In order to reconstruct tracks with lengths up to a few hundred nanometers the NEWSdm experiment adopt a two-step approach for the analysis:

- 1. shape analysis performed with an optical microscope for the *candidate* selection;
- 2. candidate validation performed with a new optical microscope, assembled in Napoli University, which allows extending the reconstruction of tracks beyond the optical limit by exploiting the resonance effect of polarized light [130, 131].

Tracks produced by dark matter interactions with nuclei in NIT emulsions are expected to be a few hundred nanometers long. Given the optical resolution limit (~200 nm) most of the tracks would appear as single clusters instead of sequences of aligned grains.

Through the shape analysis it is possible to distinguish the clusters produced by a single grain (fog) due to thermal excitation, that have a spherical shape, from clusters formed by several grains that instead have an elliptical shape with the major axis along the effective direction of the trajectory of nuclear recoils.

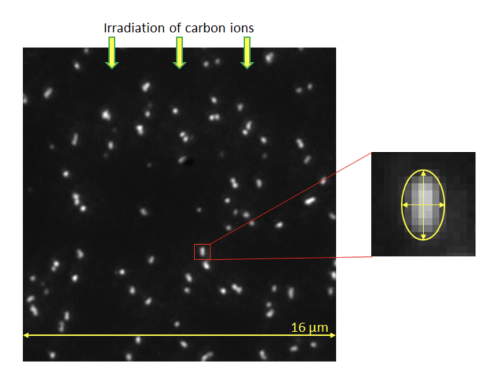


Figure 2.9: Kr ions implanted on NIT films. The image is taken with an optical microscope and the selection of candidate tracks is based on the elliptic fit of the clusters. [106]

Therefore a first selection of signal events is done using this technique. To test the efficiency and the resolution of the shape analysis and simulate the detector response to WIMP-induced recoils a test beam with low-speed ions implanted in NIT emulsions was performed.

Kr ions with energies of 200 and 400 keV [132, 133] and C ions with energies of 60, 80 and 100 keV were used since they produce in NIT emulsions tracks in the length range of a few hundred nm.

The submicrometric tracks produced by the Kr and C ions, are not resolved and appear as a single cluster when analysed by the optical microscope. On the other hand, the elliptical shape of clusters is clearly visible (see Figure 2.9). An elliptical fit is therefore performed to distinguish the signal events from the spherical fog [132].

Figure 2.10 reports the scatter plot of major and minor axes for the sample with 400 keV Kr-ion implanted (left) and the reference sample (right). The red and blue dots represent the population of cluster with ellipticity larger than 1.5 for each sample. Typically for signal tracks a threshold on the ellipticity of 1.25 or higher is set.

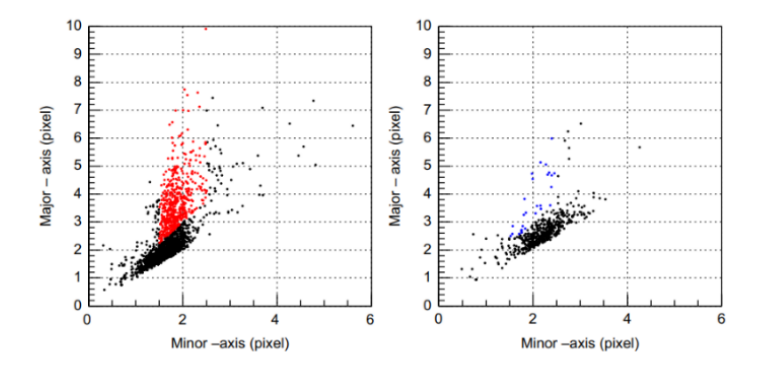


Figure 2.10: Major axis versus minor axis for the 400 keV Kr-ion sample (left) and not exposed sample (right). Red and blue dots represent clusters with an ellipticity larger than 1.5.

Moreover, the intrinsic angular resolution was estimated using NIT samples exposed to a 2.8 MeV neutron beam at the Fusion Neutron Source (FNS) in Japan. Since hydrogen has an higher neutron scattering cross-section than the other elements of NIT emulsion, the track length distribution of neutron-induced proton recoils ranges up to a few hundred micrometres. Tracks of few tens of micrometers and formed by a sequence of clusters have been selected (see Figure 2.11a). For long tracks the scattering can be neglected. The intrinsic angular resolution $(\Delta\theta)$ was estimated studying the angular difference between the direction of the major axis of elliptical clusters and the direction of the fitted track. Figure 2.11b shows the distribution $\Delta\theta$ which has a Gaussian shape, with a width equal to 230 mrad. This value represents the intrinsic angular resolution achieved with fully automated scanning systems, which is by far the best resolution achieved with direction-sensitive detectors in this energy range.

2.6 Candidate Validation

An X-ray microscope [134] was used to validate the tracks selected with the shape analysis measuring the efficiency achievable with optical microscopy. This microscope has a higher resolution (of the order of 60 nm) but a slower

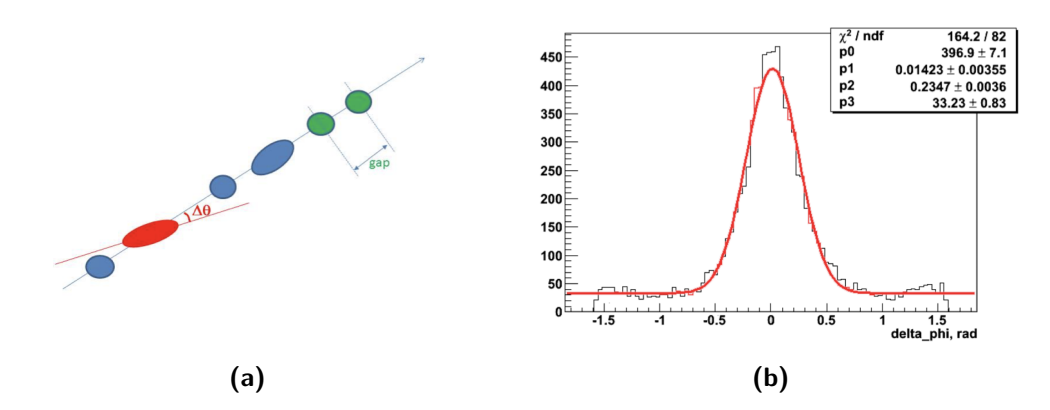


Figure 2.11: (a) Graphical representation of the method used for the evaluation of the intrinsic angular resolution. (b) Intrinsic angular resolution of the optical scanning system.

scanning speed than the optical microscope, in fact, the analysis of 100 μ m × 100 μ m requires about 100 s.

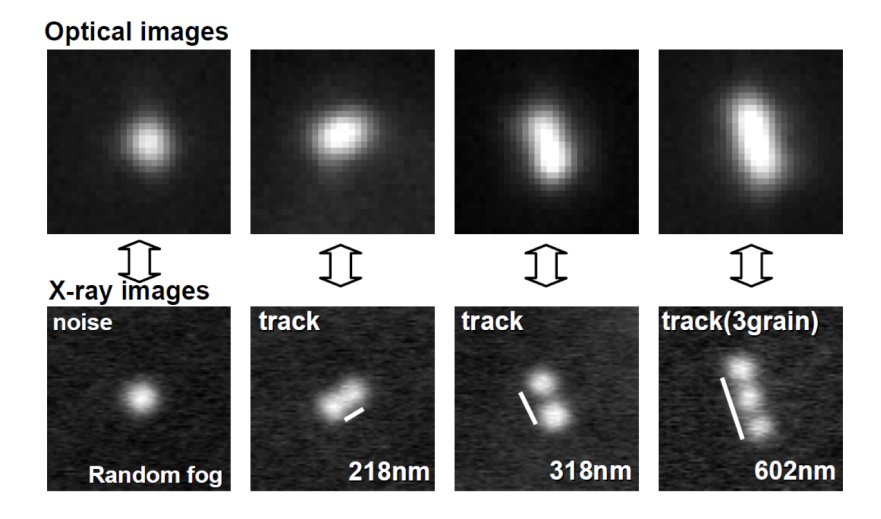


Figure 2.12: Comparison between reconstructed tracks of a few hundred nanometers length with the optical microscope and with the X-ray microscope. [106]

As shown in Figure 2.12, the high resolution of the X-ray microscope (70

nm [134]) allows resolving grains belonging to submicrometric tracks, thus providing the final discrimination between signal and background.

To evaluate the efficiency, multigrain tracks with the X-ray microscope have been selected, then scanned with the optical microscope and finally analyzed using the shape analysis. The global efficiency is 90% and it reaches 100% for tracks longer than 180-200 nm.

Therefore, X-ray microscopy can exceed the resolution of the optical microscope, which allows reconstructing tracks down to 200 nm, but it is slow compared to automated optical systems.

Since the scanning speed is a key point for high mass detectors, X-ray microscopes are not suitable for the second phase of the strategy, i.e. for the validation of candidates. Moreover, X-ray microscopes damage the sample, so that it could no longer be analyzed.

Hence, in order to overcome the limit of optical microscopes without decreasing too much the scanning speed, the candidate validation is performed exploiting the effect of plasmonic resonance that occurs when nanometric metallic grains are dispersed in a dielectric medium [131]. The free conduction electrons are driven in oscillation due to the strong coupling with the incident light in the visible ultraviolet band (UV-Vis) [135].

The coupling affects the optical properties of nano-particles producing a resonance effect in the scattered light. The dependence on the polarization of the resonance frequencies strongly reflects the nanoparticle shape anisotropy and can be used to infer the presence of non-spherical nanometric silver grains. The effect of localized surface plasmon resonance (LSPR) can be exploited in NIT emulsions where nanometric Ag grains are immersed in the organic gelatin. In the Figure 2.13, effects of resonant light scattering from single nanoparticles of Ag [131] are shown; one can see that the LSPR is sensitive to the shape of grains. Spherical particles do not show any different response depending on the incident polarization while a deformed sphere is sensitive to polarization.

The LSPR allows to infer the structure of a cluster in NIT emulsions beyond the optical resolution. Indeed multiple measurements of the same cluster with different polarization angles results in a displacement of the barycentre. The analysis of these displacements allows to distinguish clusters composed of single grain from those made of two or more grains. In this way, it is possible to obtain a measurement of the direction of the track and the length of the barycenter shift. In figure 2.14 an example of analysis performed on a cluster with ellipticity 1.27 from a 100 keV C-ion sample is shown.

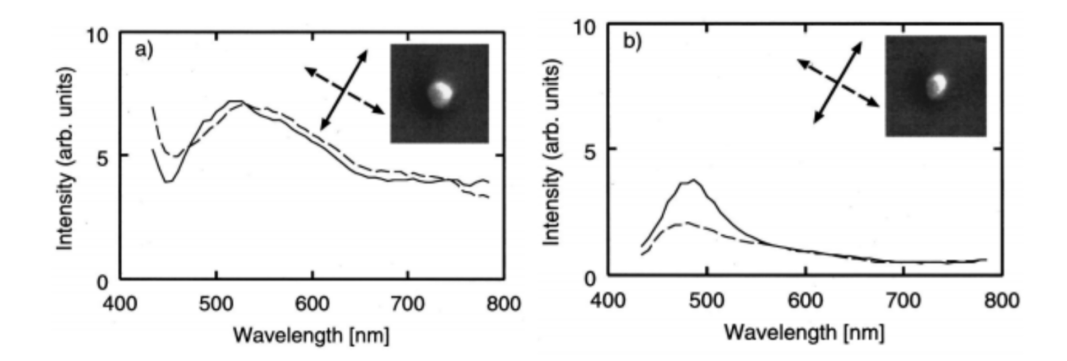


Figure 2.13: Scattered-light spectra from individual Ag particles with spherical (left) and spheroidal (right) shape [131]. Arrows indicate the polarization of the incident light. A dependence of the response on the light polarization is observed for particles with ellipsoidal shape.

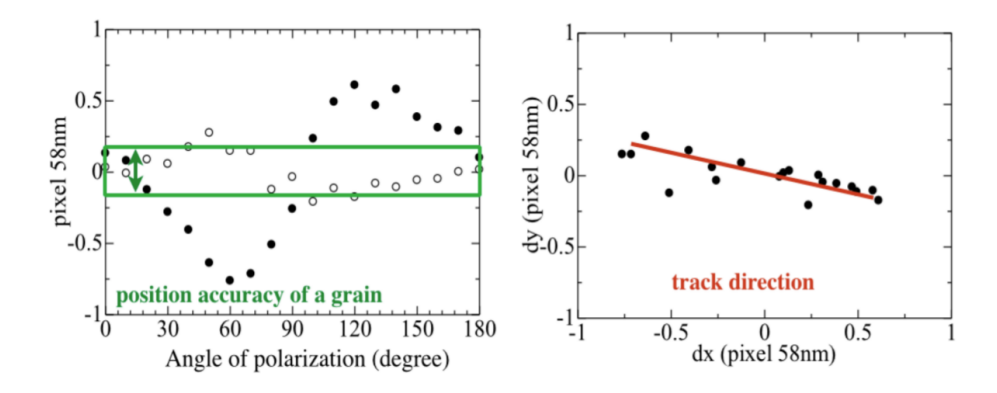


Figure 2.14: Resonance light effect exploited using different polarization angles of the incident light on a cluster with ellipticity 1.27 from a 100 keV C-ion sample. (left) dx and dy displacements of the cluster barycenter versus the polarization angle. (right) the barycenter shift in the xy-plane.[106]

The LSPRs effect has been studied in NIT emulsions using samples exposed to C-ions of different energies and obtaining an unprecedented accuracy in cluster position (< 10 nm).

Exploiting the LSPR effect the validation of the candidates identified by the shape analysis will be performed in the same scanning laboratory, without moving the samples to a dedicated laboratory for X-ray analysis and the scanning speed is much higher.

Moreover, it is possible to exploit the LSPRs wavelength dependency on the grain size, thus adding a new source of information to the Plasmon analysis, which looks at the cluster properties when observed with different polarization of incident light. Indeed, different nanometric grain size correspond to different wavelengths in the plasmon resonance response.

Chapter 3

Reconstruction of nanometric tracks

Directionality is an unambiguous proof of the intrinsic nature of WIMP dark matter. NIT emulsions are the best detector for this purpose as they allow to reconstruct tracks down to 100 nm. Optical microscopes, although limited by optical resolution, are currently the best scanning devices. However, the observation of track lengths below the diffraction limit is crucial for the NEWSdm experiment. In order to observe such tracks, the resonance effect of polarized light can be exploited: nanometric metallic grains behave differently when illuminated by light with different polarization angles. This chapter summarises the results obtained in the present thesis work about the analysis of NIT samples exposed to Carbon ions and scanned in the Napoli Emulsion Laboratory.

3.1 Scanning process

As we have seen in the previous chapter, the NEWSdm experiment follows a two-step read-out strategy for the data analysis: the candidate selection with the shape analysis and the candidate validation with the plasmon analysis. The scanning procedure for NIT emulsions is divided in the following steps:

• the area to scan is divided into overlapping $(4 \div 5\mu\text{m})$ fields of view with dimensions of $60 \times 45 \ \mu\text{m}^2$;

- for each field of view, the optical system moves along the thickness of the emulsion driving the focal plane with 250 nm steps;
- several 2D layers are therefore scanned and the corresponding images appear, due to the epi-illumination mode, as white pixels on a dark background. In case of plasmon analysis, each layer is scanned with eight different polarization angles of the incident light with 22.5° steps.
- the image processor reconstructs 2D clusters if pixels exceed a certain brightness threshold (*clustering process*);
- reconstructed clusters are then collected before moving to the next field of view.

The clustering is then followed by the *graining process* where the reconstruction of 3D grains from 2D clusters is performed.

Reconstructed 3D grains represent physical grains formed by latent images in NIT emulsions and made visible by chemical treatments. The grain reconstruction is performed as follows:

- 1. for each layer images of 2D clusters corresponding to different polarization angles are averaged to get the so called 2D merged cluster;
- 2. 2D merged clusters in the same or consecutive layers are merged to form the 3D grain if they are found within an angular acceptance defined by a truncated cone;
- 3. the brightest 2D merged cluster is referred to as the best focus cluster and the corresponding layer is called the best focus layer;
- 4. polarized clusters reconstructed in the best focus layer are defined as best focus polarized clusters.

In Figure 3.1 it is reported a schematic representation of the grain reconstruction process. The polarization information, as the barycenter shift and its direction, for each reconstructed grain is retrieved from its best-focused clusters.

Reconstructed data are usually divided into two classes: (i) micro-tracks, made of two or more adjacent and distinct grains, (ii) isolated events. The last category includes both single grain clusters (background-like) and clusters made by two or more unresolved grains (signal-like). The polarisation analysis is indeed aimed at distinguishing these two cases.

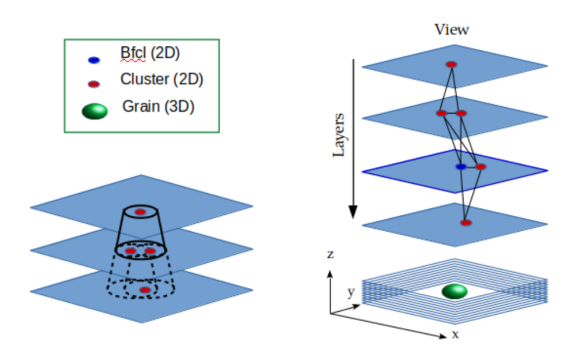


Figure 3.1: Schematic illustration of the grain reconstruction process. 2D merged clusters are represented in red and the best-focus cluster in blue. 2D merged clusters are merged to form the reconstructed grain represented in green.

3.2 Analysis of NIT exposed to Carbon ions

Several exposures are made with carbon ions that produce in NIT tracks of lengths comparable to those expected from WIMP-induced recoils; therefore they give both the possibility to calibrate the detector response and to test signal efficiency. In this work, a sample made of carbon ions implanted in NIT films made of 70 nm diameter crystals has been analyzed.

Carbon ions with energies of 100, 60 and 30 keV have been implanted on NIT with an inclination of about 10° with respect to the emulsion surface.

The average range calculated by SRIM software [136] is estimated to be 240, 150 and 80 nm, respectively. These samples are expected to contain elliptical clusters.

The analysis aims at the reconstruction of the direction of carbon ion. In particular, the goal is to evaluate the performance of the plasmon analysis in the reconstruction of directionality beyond the optical resolution limit where the shape analysis becomes ineffective.

The samples have been scanned without polarized light to perform the shape analysis and then varying the polarization of the incident light to study the plasmon resonance in NIT emulsions.

In order to evaluate the accuracy of the optical microscope, 30 keV carbon ions implanted in the NIT films with an inclination of about 80° from the

emulsion plane are used. Since such low energy vertically implanted Carbon ions sensitize only one grain, the measurement of the barycenter shift of the cluster can provide an estimation of the position uncertainty.

3.3 Shape analysis

The shape analysis is carried out on isolated grains where a fit is made with a two-dimensional Gaussian distribution. From this fit five parameters are obtained:

- μ_x and μ_y , i.e. the x and y positions of the clusters;
- σ_x and σ_y corresponding to the major and minor axes of the ellipse, respectively;
- the correlation factor ρ related to the cluster orientation.

The plots in Figures 3.2 show angular distributions, estimated by the elliptical fit of the clusters, for the 100, 60 and 30 keV samples. The distribution in Figure 3.2a and 3.2b are fitted with a Gaussian plus a constant. The constant is necessary to fit the plateau which represents the non-directional component according to the shape analysis.

The plateau is rather high because a large fraction of tracks are shorter than the optical resolution and therefore the recoil direction cannot be inferred. The directionality is well reconstructed for the 100 keV sample where longer tracks are expected, it is hardly visible in 60 keV sample and not at all in the 30keV since tracks are shorter.

It is possible to evaluate the efficiency of the reconstruction through the shape analysis as the ratio between the area under the Gaussian and the total area:

$$\epsilon_{shape} = \frac{N_{Gaus}}{N_{tot}} \tag{3.1}$$

where $N_{tot} = N_{Gaus} + N_{Flat}$ represents the sum of number of events with a preferred direction (N_{Gaus}) and a random direction (N_{Flat}) . In table 3.1 are reported the values to obtain the directional efficiency $\epsilon_{shape} = (25.0 \pm 0.2)\%$ for the sample of 100keV.

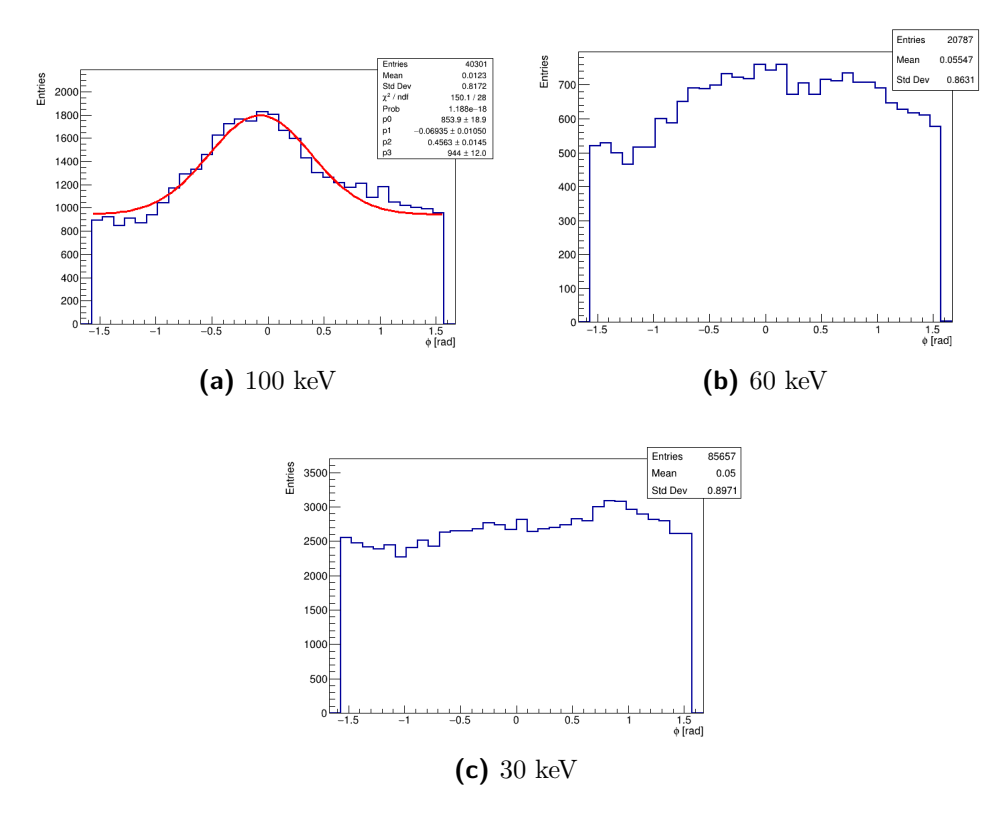


Figure 3.2: Distributions of track angles measured by shape analysis of 70nm NIT samples. The distribution in (a) is fitted with a Gaussian plus a constant.

3.4 Plasmon analysis

The shape analysis allows to perform a directional measurement of nuclear recoils with track lengths close to the microscope optical resolution (~190 nm). To further decrease the threshold in the track length reconstruction the plasmon analysis is used by exploiting the barycenter displacement of the clusters.

The plasmon analysis is effective to study the nano-tracks appearing as isolated grains and several variables are used to exploit the resonance effect induced by the polarized light:

• N_{pol} is the number of best focus polarized clusters (BFPC) for each grain, ranging from 1 to 8 which is the maximum number of polarisation angles;

Samples	100 keV
$\overline{N_{Gaus}}$	10092
N_{tot}	40301
ϵ_{shape}	25%

Table 3.1: Values need to obtain the efficiency for the 100 keV sample.

- α is the polarization angle of the best focus polarized clusters, it ranges from 0 to 180° in steps of 22.5°;
- x_{α}, y_{α} are the coordinates of the BFPCs;
- x_{bfc}, y_{bfc} are the coordinates of the barycentre of the BFPCs;
- Δs_{bfc} is the maximum distance between two BFPCs belonging to the same grain and representing for each grain the maximum barycenter displacement of its BFPCs;
- ϕ_{bfc} is the direction of the track in the xy plane, obtained from the line connecting the two extreme displacements of the BFPCs;
- Δs_{thr} is the threshold above which a displacement can be ascribed to the plasmon resonance effect.

Figure 3.3 shows the position in the XY plane of the barycenter of the BFCPs for the different polarization angles. Figure 3.3a shows a background grain that exhibits a rotational movement of the barycenter, with a displacement of ~ 10 nm, while in the figure 3.3b a signal grain for which the barycenter displacement of ~ 66.2 nm occurs with a direction of $\sim 25^{\circ}$.

Isolated grains could be made of unresolved nanotracks. Isolated grains are divided in static events ($\Delta s < \Delta s_{thr}$) and moving events ($\Delta s > \Delta s_{thr}$). In the latter category there are actually single clusters (1peak) or clusters with multiple brightness peaks (npeak).

3.4.1 Accuracy

To determine the threshold for the barycentre shift, it is useful to evaluate the position accuracy achieved in the emulsion plane (XY) by the optical microscope assembled in Napoli University.

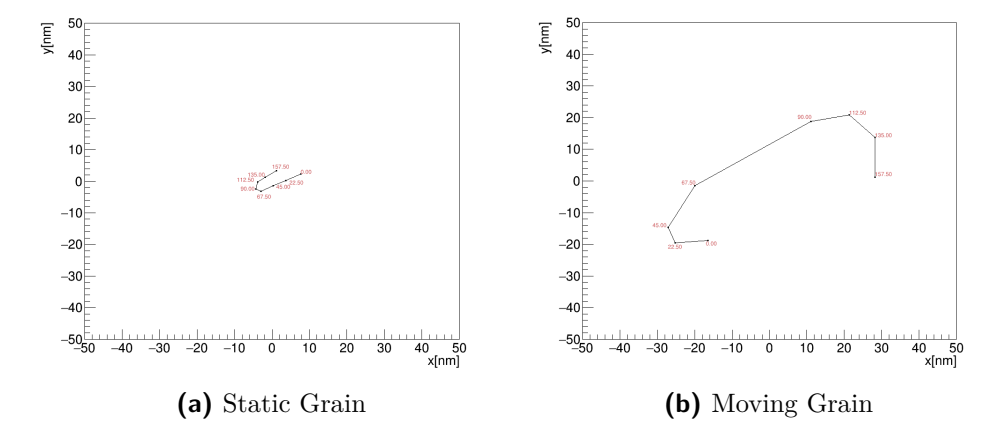


Figure 3.3: XY scatter plot of BFPCs positions for a static grain (a) and a moving grain (b).

To perform this measurement, the NIT film vertically exposed to 30 keV can be used as a reference sample for two main reasons: (i) the angular distribution of nuclear induced recoil is expected to be flat; (ii) the barycenter shift for n-crystals is expected to be small and comparable with the expected fluctuation in the cluster position. The position accuracy is defined for each coordinate as the standard deviation of BFPCs coordinates (x_{α}, y_{α}) , from BFPCs barycenter coordinates (x_{bfc}, y_{bfc}) . The accuracy is reported in Figure 3.4 where ~ 11 nm are obtained for both x and y coordinates respectively. The threshold on the barycenter shift (Δs_{thr}) has been defined as:

$$\Delta s_{thr} = 3\sigma_{xy} = 3\sqrt{\sigma_x^2 + \sigma_y^2} \sim 47nm \tag{3.2}$$

Therefore, clusters having a barycentre shift larger than 47 nm are considered signal like events.

3.4.2 Npeaks

When the distance between two grains is slightly smaller than the diffraction limit, they are still unresolved in unpolarized light. The variation of cluster brightnesses introduced by the LSPR effect caused by the polarization rotation may lead to the situation where these two grains become resolved at some polarization angles and are visible as separate clusters. For such a situation

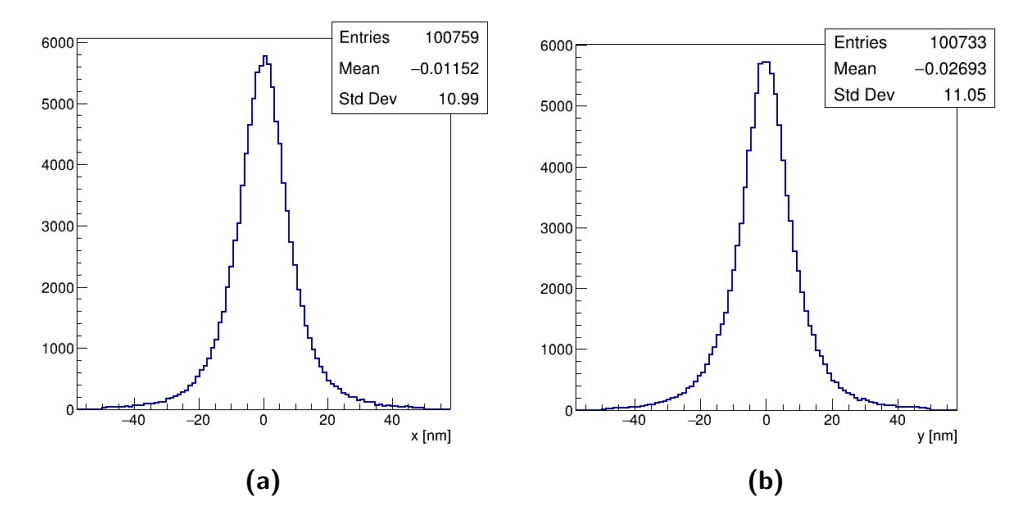


Figure 3.4: Position accuracy for the x (a) and y (b) coordinates.

an event class called npeaks is defined. This class represents intermediate events that are too short to be resolved by ordinary microscopes but can be treated as microtracks with the help of the plasmon analysis. Therefore, the length and the direction of npeak events are measured as a distance and the orientation of the two most distant clusters in resolved images.

Figure 3.5 shows the track length with respect to the angle ϕ for the npeaks analyzed samples of 100 (3.5a), 60 (3.5b) and 30 (3.5c)keV.

A clear peak in the beam direction is observed for 100 keV and 60 keV samples exposed horizontally in the npeaks region, i.e. with track lengths shorter than 350 nm. On the other hand, no angular correlation is visible for longer track lengths that are therefore interpreted as chance coincidence. This result shows that the npeaks grains are connected to the same carbon ion and therefore represent signal-like events.

The 2D angular distributions of the npeaks event are shown in Figure 3.6 for each sample. In the 30 keV sample (see 3.6c) the signal is not visible since the traks are too short, while for the other two samples it is much more evident. In particular, for the 100 keV sample (3.6a) a Gaussian plus a constant fit was made and it returns a value of $\sigma = (0.31 \pm 0.012)$ rad while for the 60 keV sample (3.6b) it returns $\sigma = (0.29 \pm 0.06)$ rad.

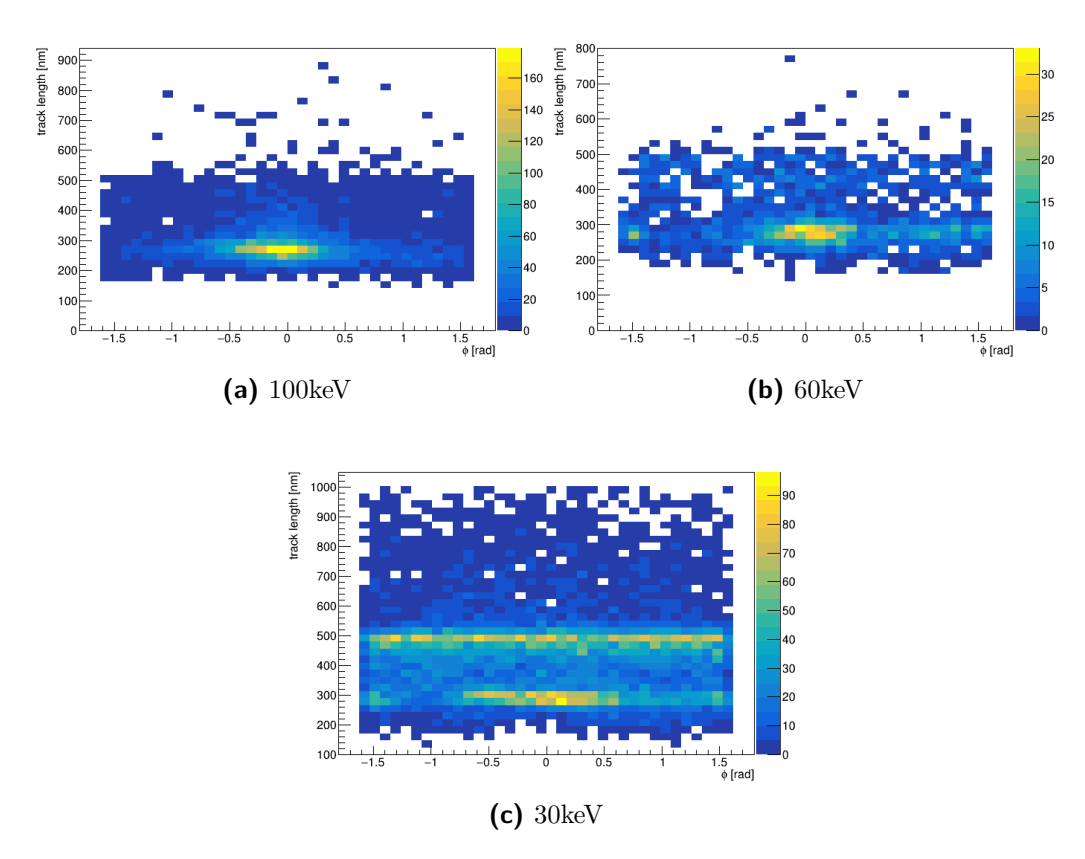


Figure 3.5: Track length versus the angle ϕ of npeaks events in 100, 60 and 30 keV samples.

3.4.3 Isolated grains

The dataset for each sample analyzed is mainly composed of isolated events, since the majority of induced recoils are unresolved by the optical microscope. Figure 3.7 shows the barycenter displacement for the horizontal samples of the three different energies, the average value is 45.2 nm for the 100 keV, 38.1 nm for the 60 keV, 39.5 nm for the 30 keV samples rispectively. The barycenter displacement is expected to increase as the energy increases, as seen for 100 keV sample. The barycenter displacement of clusters plays a key role of the discrimination between signal-like and background like event. The direction of the displacement of the barycentre provides the 2D angular distribution shown in Figure 3.8 where the moving events are in red and the

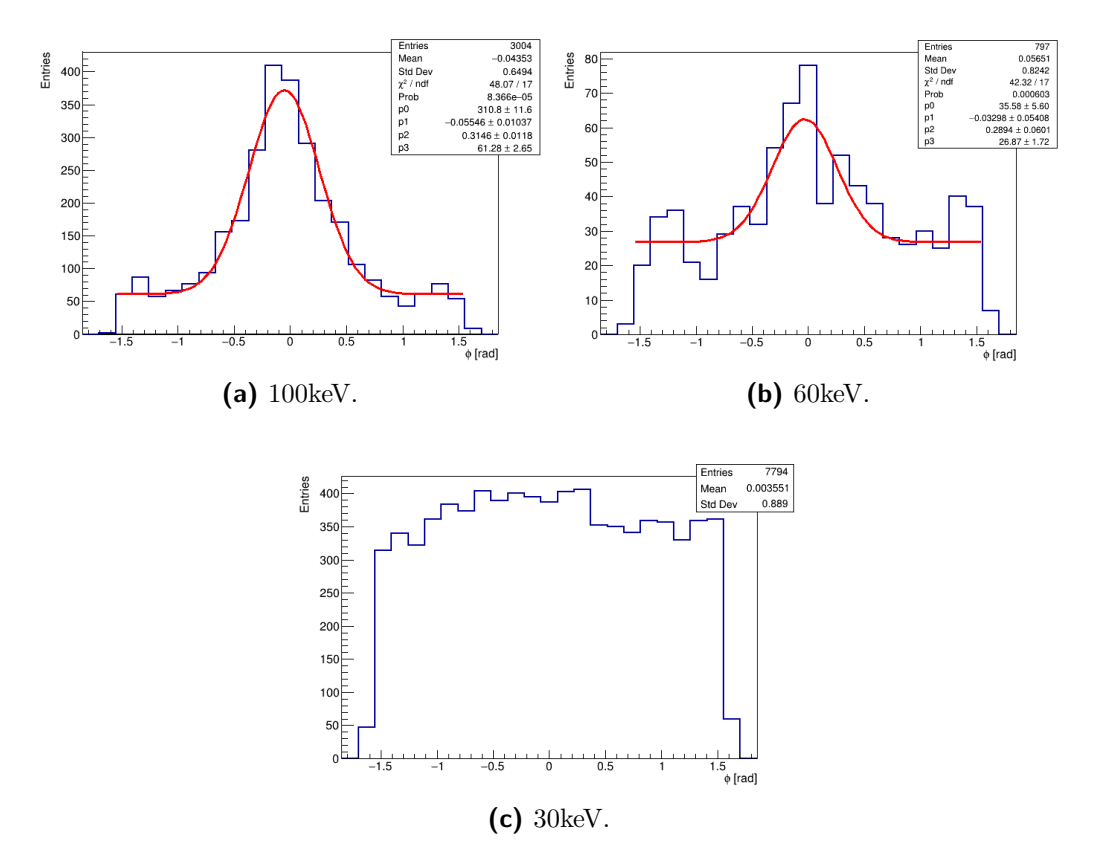


Figure 3.6: Angular distribution of npeaks grains obtained by plasmon analisys for the 100keV, 60keV, 30keV samples. The plot in (a) and (b) are fitted with a Gaussian plus a constant.

static ones in blue; their fraction is reported in Table 3.2.

As expected, moving grains have a peak in the incoming direction of carbon ions, while the static ones show flat angular distribution. For the moving grain, a Gaussian plus a constant fit was made this returning a value of $\sigma = (0.35 \pm 0.02)$ rad, for the 100 keV sample (3.8a) and $\sigma = (0.29 \pm 0.05)$ rad for the 60 keV sample (3.8b), that re comparable within errors

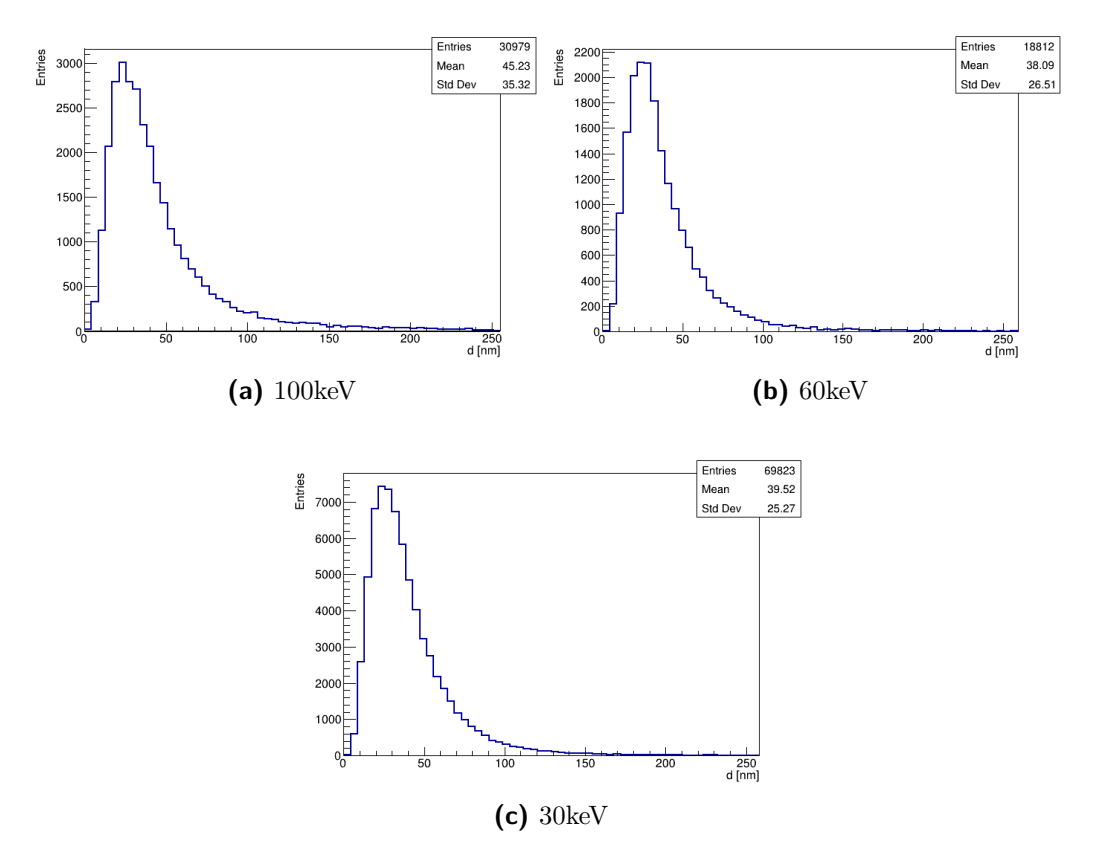


Figure 3.7: Distributions of the barycenter displacement for the three samples.

3.5 Plasmon efficiency

The efficiency of the plasmon analysis can be evaluated considering that npeaks and moving grains represents signal-like events. This efficiency can be defined as:

$$\epsilon_{pl} = \frac{N_{npeaks} + N_{moving}}{N_{tot}} \tag{3.3}$$

where N_{npeaks} and N_{moving} are the numbers of npeaks and moving grains, respectively, and N_{tot} is the total number of events. In table 3.3 are reported the plasmon efficiencies: $\epsilon_{pl} \sim (34.7 \pm 0.2)\%$ for 100 keV sample and $\epsilon_{pl} \sim (26.1 \pm 0.3)\%$ for 60 keV sample.

Samples	100 keV	60 keV	30 keV
Moving	0.32	0.24	0.27
Static	0.68	0.76	0.73

Table 3.2: Fraction of moving events and static events for 100, 60 and 30 keV samples.

Samples	100 keV	60 keV
$\overline{N_{npeaks}}$	3004	797
N_{moving}	9984	4586
N_{tot}	37380	20643
ϵ_{pl}	34.7%	26.1%

Table 3.3: Numbers of npeaks, moving grains and the total number of events for the 100 keV and 60 keV sample.

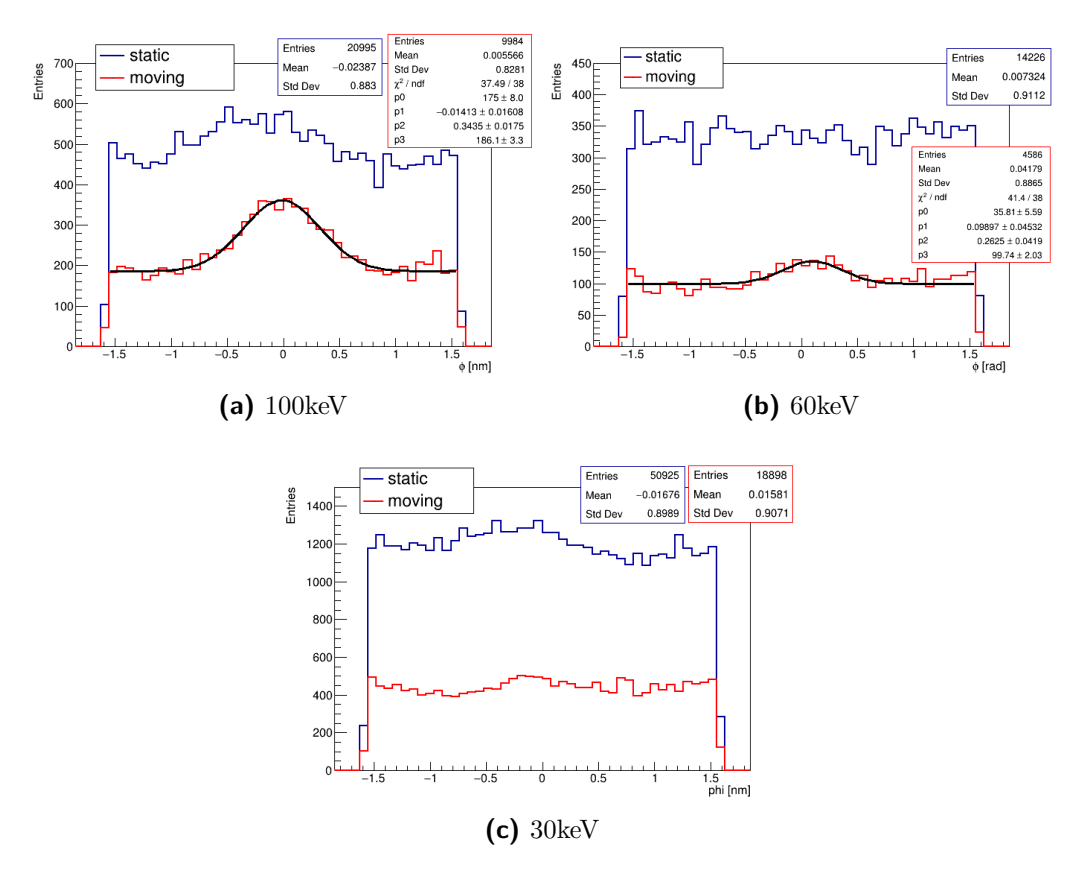


Figure 3.8: 2D angular distribution of moving grains (red) and static ones (blue) for the three different samples. The red distribution of moving grain for the 100 keV (a) and 60 keV (b) are fitted with a Gaussian plus a constant.

Chapter 4

Deep Learning and Convolutional Neural Network

This chapter will be dedicated to a description of artificial intelligence, starting from the basic principles of machine learning and then moving on to deep learning and convolutional neural networks. Reference used for this chapter are [137–139].

4.1 Artificial intelligence and Machine Learning

Artificial intelligence (AI) was born in the fifties when the still unresolved question was asked: "Can machines think?". AI is a wide-ranging branch of computer science concerned with building smart machines capable of performing tasks that typically require human intelligence. AI is a general field that includes machine learning and deep learning (see section 4.2, Figure 4.1), but this also includes many other approaches that do not involve learning at all.

Originally many experts believed that artificial intelligence at the human level could be achieved by having programmers who made a sufficiently large set of explicit rules for manipulating knowledge. This approach is known as symbolic artificial intelligence and has been the dominant paradigm in AI from the 1950s to the late 1980s. Symbolic artificial intelligence proved to be suitable to solve well-defined logical problems, such as playing chess. Instead, it proved intractable to understand the explicit rules to solve more complex

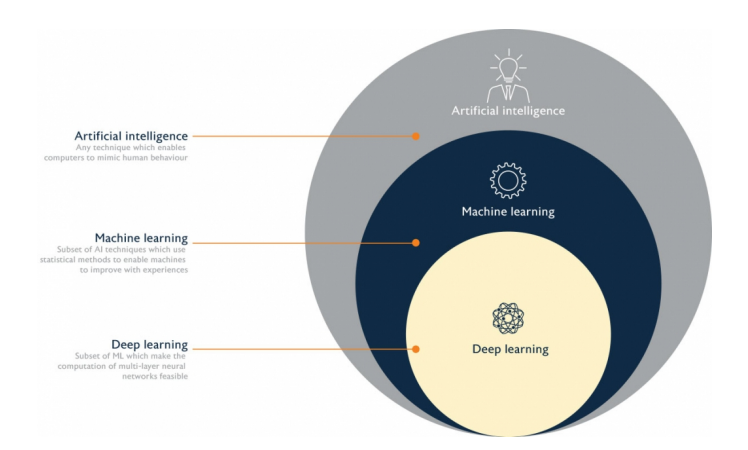


Figure 4.1: Schematic of Artificial intelligence, machine learning and deep learning.

and confusing problems, such as image classification and voice recognition. Thus giving rise to a new approach, namely machine learning.

Alan Turing in his historic 1950 article "Computing Machinery and Intelligence" [140] introduced the Turing test and the key concepts that would shape AI. He on whether computers could be capable of learning and he came to the conclusion that they could. Automatic learning stems from wondering if a computer could automatically learn rules by looking at the data; question that opens the door to a new programming paradigm. In classical programming, the paradigm of symbolic artificial intelligence, man inserts the rules (a program) and the data to be processed according to these rules, and the answers come out (Figure 4.2). With automatic learning, human beings insert the data and the answers expected from the data, and here come the rules. These rules can then be applied to new data to produce original answers. A machine-learning system is trained rather than explicitly programmed. It is fed with many examples relevant to a task, and it finds statistical structure in these examples that eventually allows the system to come up with rules for automating the task.

Machine-learning algorithms generally fall into three broad categories:

Supervised learning is by far the most common, consists of learning to map input data to known targets, given a set of examples. In general, almost all deep learning applications, such as character recognition, speech recognition, image classification and language translation belong

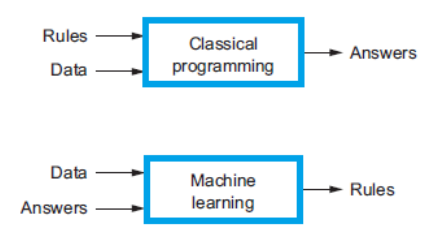


Figure 4.2: Classical programming vs Machine learning.

to it. It consists mostly of classification and regression;

Unsupervised learning consists of finding interesting transformations of input data without the help of any targets, in order, for example, to better understand the correlations present in the data. Clustering is one of the best known categories, i.e. from non-labelled data searching to find patterns or sets of points that have common characteristics;

Reinforcement learning according to which an agent receives information about its environment and learns to choose actions that will maximize some reward. Currently, this is mostly a research area and hasn't yet had significant practical successes beyond games.

In machine learning, the goal is to achieve models that generalize well to never-before-seen data, and the biggest obstacle is the overfitting, i.e. the prediction corresponds too closely or exactly to a particular set of data, and may therefore fail to fit additional data or predict future observations reliably. Therefore turn to be fundamental splitting the datset into training and test: the former is necessary for the network to learn how to perform the task for which it was conceived, minimizing the cost function; the latter is needed to test the performance and therefore the generalizations that the network makes on new data. Strategies commonly used for minimizing the cost function are Gradient Descent [138] and ADAM [141].

4.1.1 Classification and Regression problem

Classification in machine learning is a supervised learning approach in which the algorithm learns from the data given to it and make new observations or classifications. This is a process of categorizing a given set of data into classes, that starts with predicting the class of given data points. The classes are often referred to as target, label or categories.

Classification consist of approximating the mapping function from input variables to discrete output variables. The main goal is to identify in which class/category the new data will fall into.

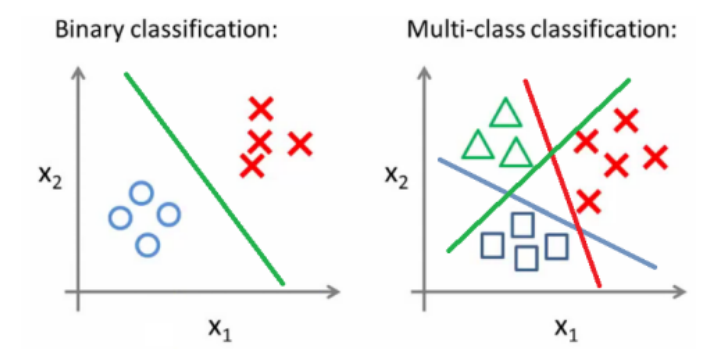


Figure 4.3: Schematic representation of binary classification (left) and multiclass classification (right) [142].

The goal of classification problems is to predict a single discrete label of an input data point. There are binary classification i.e. classifying instances into one of two classes and multi-class classification with more than two classes (see 4.3).

Examples of the former are movie reviews as positive or negative, based on the text content of the reviews; medical testing to determine if a patient has a certain disease or no; email-spam and so on. While, the latter includes, the most common application of deep learning of these days, such as handwritten character recognition, speech recognition, image classification and language translation.

Another common type of machine-learning problem is regression, which consists of predicting a continuous value instead of a discrete label: for instance, predicting tomorrow temperature, given meteorological data; estimating the price of a house, given real-estate data.

So giving some predictor variables and a continuous response variable, regression try to find a relationship between those variables that allows to predict an outcome.

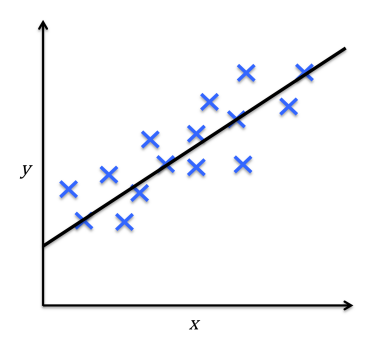


Figure 4.4: Linear regression [138].

The Figure 4.4 illustrates the concept of linear regression. Given a predictor variable x and a response variable y, a straight line fit to this data so that minimizes the distance, most commonly the average squared distance, between the sample points and the fitted line. The intercept and slope learned from this data can be used to predict the outcome variable of new data. Linear regression is just one of the simplest case of regression.

4.2 Deep Learning

Deep learning is a sub-field of machine learning that emphasizes learning successive layers of increasingly meaningful representations. Modern deep learning often involves tens or even hundreds of successive layers of representation and they are all learned automatically from exposure to training data. Meanwhile, other approaches to machine learning tend to focus on learning only one or two layers of representations of the data.

In deep learning, these layered representations are learned via models called neural networks, structured in layers stacked on top of each other. Deep learning is a framework for learning representations from data.

The training of a neural network always depends on the following objects:

- layers, which are combined into a network;
- the input data and corresponding targets;
- the loss function, which defines the feedback signal used for learning;

• the optimizer, which determines how learning proceeds

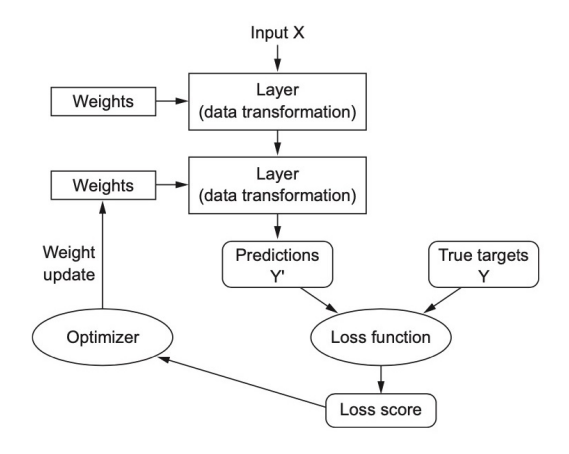


Figure 4.5: Relationship between the network, layers, loss function, and optimizer [137].

In Figure 4.5 it is shown how they interact: the network, composed of layers that are chained together, maps the input data to predictions. The loss function then compares these predictions to targets, producing a loss value: a measure of how well the network's predictions match what was expected. The optimizer uses this loss value to update the network's weights.

The most common techniques of deep learning are convolutional neural network for image processing and recurrent neural networks for sequence processing.

For this work a convolutional neural network will be used, so a full section is dedicated to it while here it is given a hint of how recurrent neural network works.

A recurrent neural network (RNN) processes sequences by iterating through the sequence elements and maintaining a state containing information relative to what it has seen so far. The simplest possible RNN is composed of just one neuron receiving inputs, producing an output, and sending that output back to itself, as shown in Figure 4.6(left). At each time step t, this recurrent neuron receives the inputs x(t) as well as its output from the previous time step, y(t-1), a representation of this network in function of the time is shown in Figure 4.6(right). From this small network, it is possible to create a

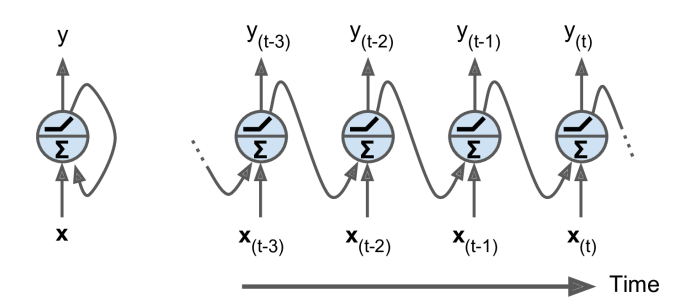


Figure 4.6: A recurrent neuron (left), unrolled through time (right)[143].

layer of recurrent neurons, where now input and output are vectors instead of scalar Figure 4.7.

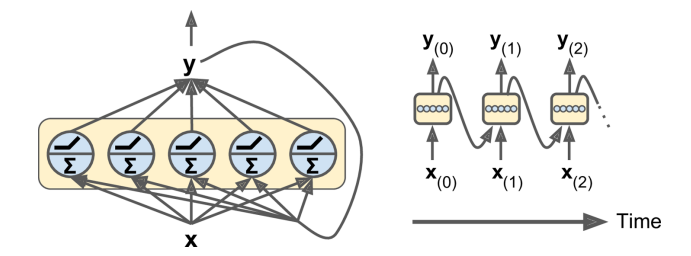


Figure 4.7: A layer of recurrent neurons (left), unrolled through time (right) [143].

4.3 Convolutional Neural Network

A convolutional neural network (CNN) is a feed-forward type of neural network inspired by the organization of the visual cortex.

CNNs are one of the most popular categories of neural networks, especially for high dimension data like images. CNNs work very similarly to standard neural networks. A fundamental difference, however, is that each unit in a layer of CNN is a filter that is convoluted with the input of that layer. CNN filters have a similar, but smaller spatial shape than input images and use parameter sharing to significantly reduce the number of learning variables. One of the first forms of CNN was the Neocognitron model proposed by Kunihiko Fukushima [144]. It consisted of several levels that automatically

learned a hierarchy of abstractions of features for model recognition. The Neocognitron was motivated by the seminal work of Hubel and Wiesel [145] on the primary visual cortex which showed that neurons in the brain are organized in the form of layers. These layers learn to recognize visual patterns by first extracting local features and then combining them to obtain higher-level representations. Network training was performed using a reinforcement learning rule. An important improvement compared to Neocognitron was the LeNet model proposed by LeCun et al. [146], where the parameters of the model were learned by using the error back-propagation. This CNN model was successfully applied to recognize handwritten figures.

CNNs are used for both supervised and unsupervised learning paradigms. In the mechanism of supervised learning, the input to the system and the desired outputs (true labels) are known and the model learns a mapping between the two. In the mechanism of unsupervised learning, the true labels for a given set of input are not known and the model aims to estimate the underlying distribution of the input data samples. CNN learns to map a given image in its corresponding category by detecting a series of abstract representations of the characteristics, ranging from simple to more complex ones. These discriminating characteristics are then used within the network to predict the correct category of an incoming image.

Convolutional neural networks are made of:

- an input, i.e. pictures
- one or more hidden layer, that compute with activation functions
- output layer that carries out the classification

A CNN is composed of several basic building blocks, called the CNN layers. Some of these layers implement functionalities such as normalization, pooling, convolution, and fully connected layers. The main difference from other neural networks is the convolutional layer. Convolution layers are the most important component of a CNN, since they extract features of the images through the use of filters which are convolved with a given input to generate an output feature map.

A filter is used to detect the presence of specific features or patterns present in the original image (input). It is usually an array of discrete numbers with a smaller dimension but the same depth as the input file. The weights of each filter (the numbers in the grid) are learned during the training of CNN. This

learning procedure involves a random initialization of the filter weights at the start of the training.

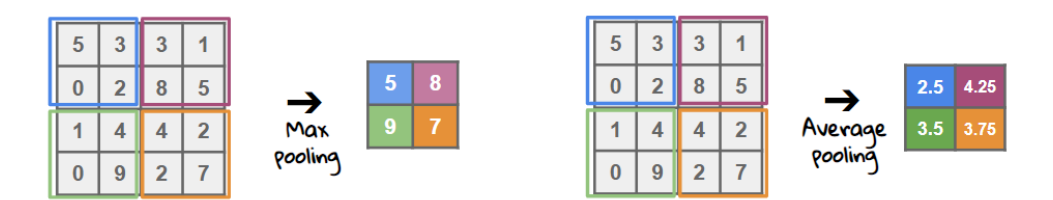


Figure 4.8: Representation of the pooling layer behavior: (left) Max pooling; (right) Average pooling.

The Pooling layer can be seen between Convolution layers in a CNN architecture. This layer reduces the number of parameters and computation in the network, controlling overfitting by progressively reducing the spatial size of the network. Similar to the convolution layer, we need to specify the size of the pooled region and the stride. Pooling may compute a max or an average. Max pooling uses the maximum value from each of a cluster of neurons at the prior layer [147, 148]. Average pooling uses the average value from each of a cluster of neurons at the prior layer [149]. Figure 4.8 (left) shows the max pooling operation, where the maximum activation is chosen from the selected block of values, while Figure 4.8 (right) shows the average pooling operation, where the average activation is chosen from the selected block of values. The pooling operation effectively down-samples the input feature map. Such a downsampling process is useful for obtaining a compact feature representation which is invariant to moderate changes in object scale, pose, and translation in an image [150].

Fully connected layers correspond essentially to convolution layers with filters of size 1×1. Each unit in a fully connected layer is densely connected to all the units of the previous layer. In a typical CNN, full-connected layers are usually placed toward the end of the architecture. However, some successful architectures are reported in the literature which use this layer at an intermediate location within a CNN (e.g., NiN [151]).

4.3.1 Hyperparameters

Similarly to all neural networks, also for convolutional ones, there are hyperparameters, values that characterize one model from the other and affect the functioning and the performance of the model itself.

The optimization of hyperparameters is a complex problem whose solution, sometimes, is empirical and usually requires comparison with numerous variants of the model to select the best one.

For an optimal process of training and evaluation of the model, at least two phases are necessary for which a division of the dataset is carried out. During the training, some instances are provided to the model for the optimization of the parameters and to compute the objective function, while during the test phase the final performance of the system and the degree of generalization achieved are evaluated.

The division of the dataset is necessary in order to avoid overestimating performance and limit overfitting. This is because if the test set is a subset of the training set, it means that the examples provided during the evaluation have already been seen and "learned" from the model and will therefore provide good results. If the test set contains examples never seen before by the model, a good response from the model will indicate a good level of generalization achieved during training.

Hyperparameters can be divided into two types: (i) that determines the network structure; (ii) that determines the network training. In the first class there are items such as:

- the size of the filter known as kernel Size;
- stride i.e. the rate at which the kernel pass over the input image;
- Padding surrounds the layer with zeros-valued pixels, thus preventing shrinking in the feature maps when multiple convolutional layers are used:
- hidden layer are the layers between input and output layer;
- activation functions allows the model to learn nonlinear prediction boundaries.

Instead in the second class there are:

- learning rate, the amount of parameter update or the size of the update step;
- epochs, the number of times we feed our network with the entire dataset;
- Batch size, the number of samples that will be propagated through the network after which weights are updated;
- loss function to measure the success of the prediction.

In the following chapter the aim of this work and the structure of the convolutional neural network made for that goal will be exposed.

Chapter 5

Convolutional Neural Network for the reconstruction of z-coordinates

5.1 z-coordinate reconstruction

The observation of tracks in emulsions is performed by optical microscopes. The highest achievable point-to-point resolution that can be obtained with an optical microscope is governed by a fundamental set of physical laws that cannot be easily overcome by rational alternations in objective lens or aperture design. A point object in a microscope, generates an image at the intermediate plane that consists of a diffraction pattern created by the action of interference. The diffraction pattern of this point source is referred to as Airy pattern. The resolution limit of a microscope is defined as the distance of the two point sources at which their images show a separation such that the peak of one Airy pattern coincides with the first dark ring of the other. This is referred to as the Rayleigh's Criterion for resolution. The numerical expression of Rayleigh's Criterion is as follows:

$$R_{Rayleigh} = 0.6 \frac{\lambda}{NA} \tag{5.1}$$

where λ is the wavelength of the illuminating light and NA is the so-called numerical aperture of objective lens. For the axial resolution the formula changes to:

$$R_{Axial} = \frac{2\lambda}{NA^2} \tag{5.2}$$

The limit is basically a result of diffraction processes and the wave nature of light. The high frequency components that give an image its sharpness are lost by the finite numerical aperture of the lens that collects the light. This results in a blurry appearance of the captured image. The resulting image is a convolution of the actual object with the so-called point spread function (PSF) of the optical system.

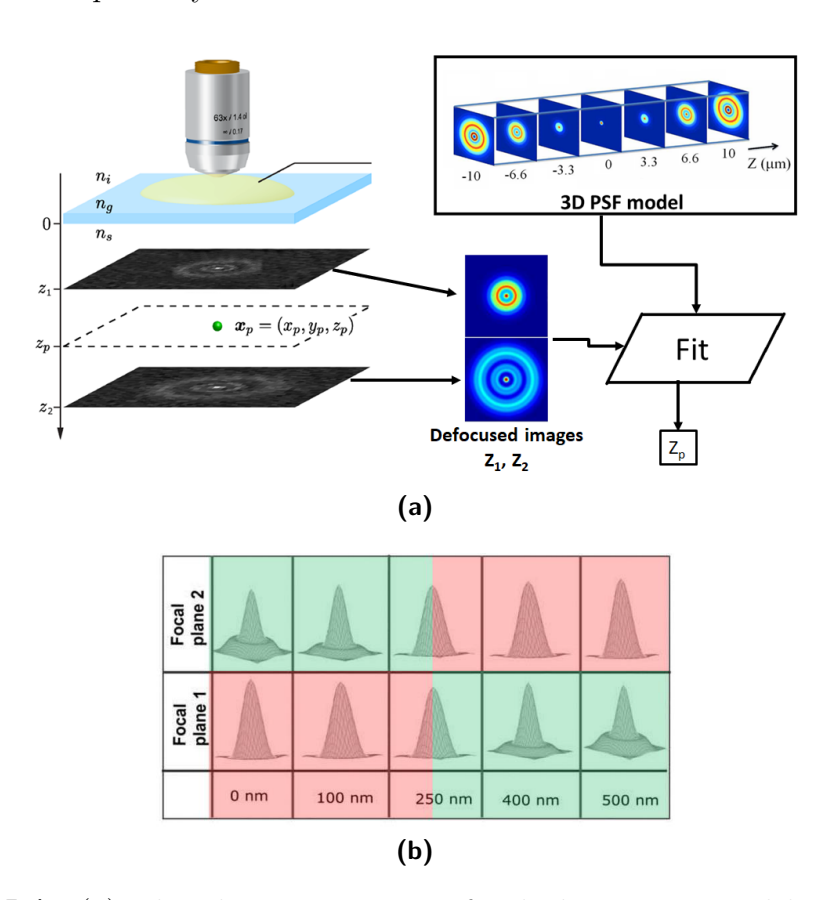


Figure 5.1: (a) The idea is to use two focal planes separated by a small distance (~DoF) so that the object will always be out of focus at one of the planes. (b) Simulated PSFs of a point-like source at different Z positions in a two-plane microscope setup. The planes are 500 nm apart. Zero of the Z-axis coincides with the Focal plane 1

However, under ideal conditions with the most powerful objective lenses, the resolution is still limited to relatively modest levels approaching 200 to 250 nm due to transmission characteristics of glass at wavelengths beneath 400

nm and the physical constraints on numerical aperture.

Though the optical resolution of a conventional microscope is limited by diffraction, and diameter of a small pinhole cannot be measured directly, the position of the pinhole center can be calculated with an extremely high precision if only one measurement is concerned. Due to the presence of thermal noise on the camera sensor and leakage of vibrations from the outer world into the scanning system, two consecutive measurements of the pinhole's center will not yield exactly the same result, thus limiting the spatial resolution. Nevertheless, it is still much higher than the optical one. As reported in [130] the spatial resolution of a conventional microscope is as high as 3 nm.

The same approach does not work in case of the axial coordinate measurement since the only available observable in this case is the 2D cross-section of the 3D point spread function, which shape strongly depends on the distance to the focal plane and does not allow precise localization of the object. A possible solution could be to scan in depth with finer sampling and fit the depth profile but this would significantly reduce the overall scanning speed. The distance from the plane of best focus at which an object is still seen as focused is referred to as the depth of focus (DoF). The DoF of a microscope can be estimated with a formula:

$$DoF = \frac{\lambda n}{NA^2} + \frac{ne}{MNA} \tag{5.3}$$

where n is the refraction index of the media and e is the dimension of the sensor pixel. For the NA = 1.45 and the blue light it gives $DoF \sim 400$ nm. As shown in Figure 5.1b, in the vicinity of the focal plane 1, inside the DoF, the PSF does change noticeably (red zone), leading to the localization problem: when an object is focused its axial coordinate is known with the precision not better than the DoF.

When the object goes out of focus and resides at the distance greater than the DoF from the focal plane, the PSF starts to change rapidly and new rings of varying radii appear, as it is shown in Figure 5.1b in green zone, allowing good axial localization of the object.

The combination of two focal planes at the distance greater than the DoF in the same microscope (shown in Figure 5.1a) allows overcoming the localization problem and enables precise measurements of the axial coordinate. Indeed, considering the Figure 5.1b, with such a configuration the object never gets focused simultaneously in focal plane 1 and 2. It is clearly visible that when the source is closer than 250 nm to either of the planes its PSF looks almost

the same. However, the PSF seen on the opposite plane changes significantly. Analyzing the difference in PSFs visible simultaneously at both planes, one can estimate the Z coordinate of the object.

In [152] this strategy was performed analytically, while in this work we have a dedicated neural network and trained it to estimate of the Z coordinate using two input PSF images of the object visible at both planes.

5.1.1 CNN architecture

The Convolutional Neural Network suitable for this work should implement a regression and not a classification since it is necessary to have a real number as output. In order to construct this CNN Keras [153] and Tensorflow [154] library were used. In Figure 5.2 a schematic representation of the built CNN architecture is shown.

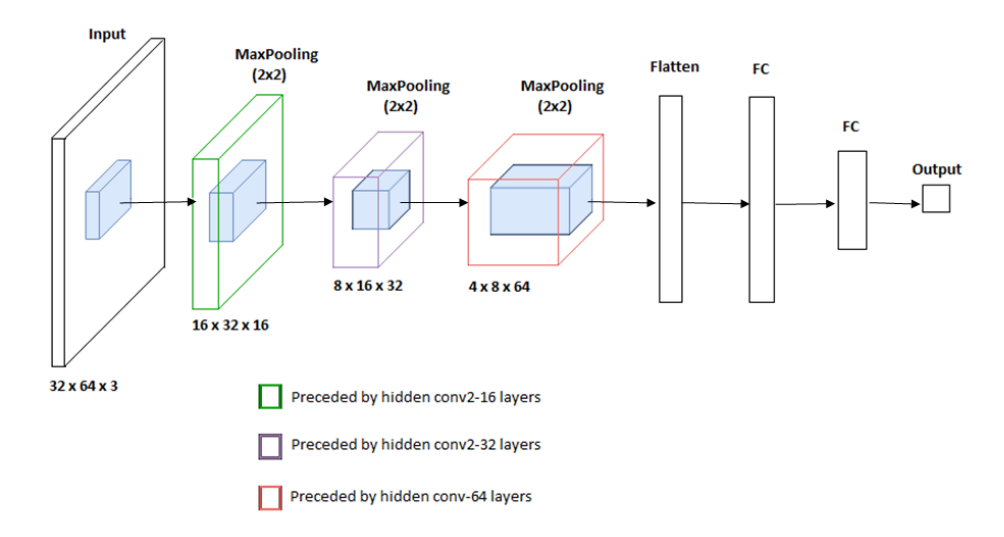


Figure 5.2: Schematic representation of CNN architecture.

For each filter adopted (16, 32, 64), the network follow the scheme:

$$CONV \Rightarrow RELU \Rightarrow BN \Rightarrow POOL$$

The convolutional layer use a kernel size of (3×3) and the function padding "same" since the reduction is made in the following. Then the ReLU activation

function is used, which takes an input and returns either the same value, or zero if the input value is negative. This can be represented as follows:

$$f_{relu}(x) = max(0, x) \tag{5.4}$$

The ReLU activation is motivated by the processing in the human visual cortex [155]. The Batch Normalization (BN) layer applies a transformation that maintains the mean output close to 0 and the output standard deviation close to 1. The pooling layer downsamples the input representation by taking the maximum (or average) value over the window defined by pool size (2×2) for each dimension along the features axis.

Then there is the flattern layer necessary to rearrange the three dimensional data, output of the last pooling layer, in a one dimensional vector since the next fully connected layers only accept one dimensional vector of numbers. The one dimensional vector is fed into the fully connected layer followed by the ReLU activaction function and a batch normalization layer. A DropOut Layer is added in order to randomly sets input units to 0 (removing neurons) with a frequency of rate (0.5) at each step during training time, which helps prevent overfitting.

Another FullyConnected Layer is added with the RelU activaction function. Finally the last FullyConected Layer with a linear activaction function is added to perform the regression.

5.1.2 Image dataset

The input dataset fed into the CNN is composed of images of a sample of 60 nm diameter sferical nanoparticles acquired with the optical microscope. In particular, to select images of interest several cuts were made on grain parameters:

- 1. the difference between the frame First and frame Last have to be larger than 4 (for the last dataset to increase statistics this value was set at 2);
- 2. the minor axis should be smaller than 155.4 nm;
- 3. the ellipticity must be smaller than 2.

In particular 2. and 3. were applied to select round events in order to be sure that are due to single nanoparticles. If grain features satisfy such cuts,

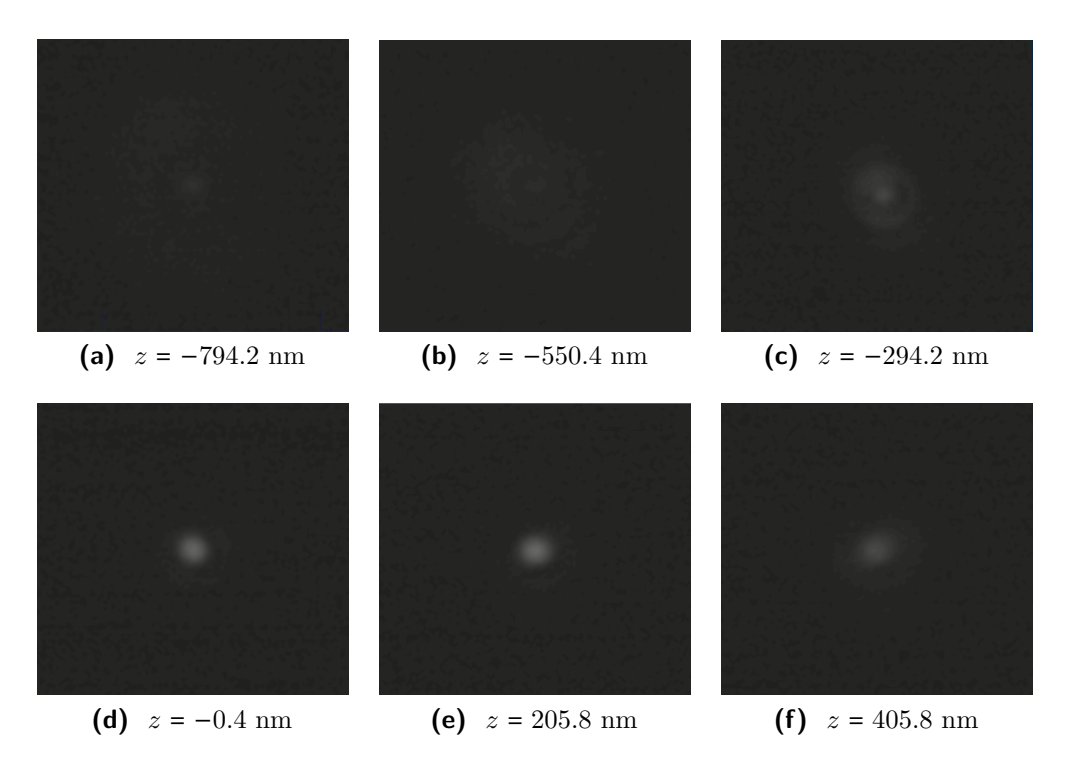


Figure 5.3: Set of images of grains acquired at different z with step of ~ 250 nm.

images are saved, in size of (90 pixel \times 90 pixel). For each grain different images are obtained with a z distance of about 250 nm, as shown in Figure 5.3.

Such dataset was fed into the CNN, after the following operations have been performed.

Images are taken from the input path and resized to a dimension of (32 pixel \times 32 pixel). Subsequently, for each grain, images with a distance of about 500 nm are grabbed together to form an image of size (32 pixel \times 64 pixels), ready for the Network (Figure 5.4).

Figure 5.5 shows three different datasets used for this work, in particular, these histograms represent the smallest z, used as a reference, of the two merged images. The smallest z values saved in a dataframe are fundamental to predict the correct one at the end of the network.

Histograms in figure 5.5a (small dataset with peaks) and 5.5b (big dataset with peaks) show 5 peaks due to the acquisition method of microscopes, which

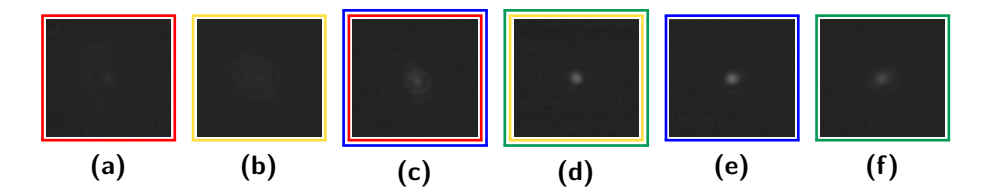


Figure 5.4: Set of images of grains acquired at different z with step of ~ 250 nm. Pictures with the same edge colour have a distance of ~ 500 nm and are grabbed together to form the input image for the CNN.

grab images with steps of 250 nm. The difference between them is due only to the increased number of entries, consequence of a more strict selection with the cut on the difference between the first frame and the last frame. While the histogram in Figure 5.5c (uniform dataset) was obtained to test the CNN on a uniform distribution. In order to remove the peaks from the large dataset, a cut at 230 entries was applied obtaining the uniform distribution. During this study, datasets have been split in 80% as the sample of training and the 20% for the test.

5.2 Results

In order to obtain the best accuracy and overcome the diffraction limit, several runs were made on the Convolutional Neural Network described in the section above. As it is known, achieving optimal results with Machine Learning technique requires finding the best parameters for the model.

A tuning on hyper-parameters that determine the network training was made; in particular the following parameters were considered: epochs, batch size and drop out, using the values [30, 200, 250, 400, 600], [4, 8, 16, 32, 64] and [0.4, 0.5, 0.6], respectively. Moreover, another parameter was changed, the loss function. It was tested only on the small dataset with peaks, since using the mean squared error (MSE), suitable for regression problem, instead of mean absolute percentage error (MAPE) shows evident improvement. The mean absolute percentage error compute the error between true z value (z_true) and the predicted z value (z_pred) as:

$$loss = 100 \times \frac{abs(z_true - z_pred)}{z_true}$$

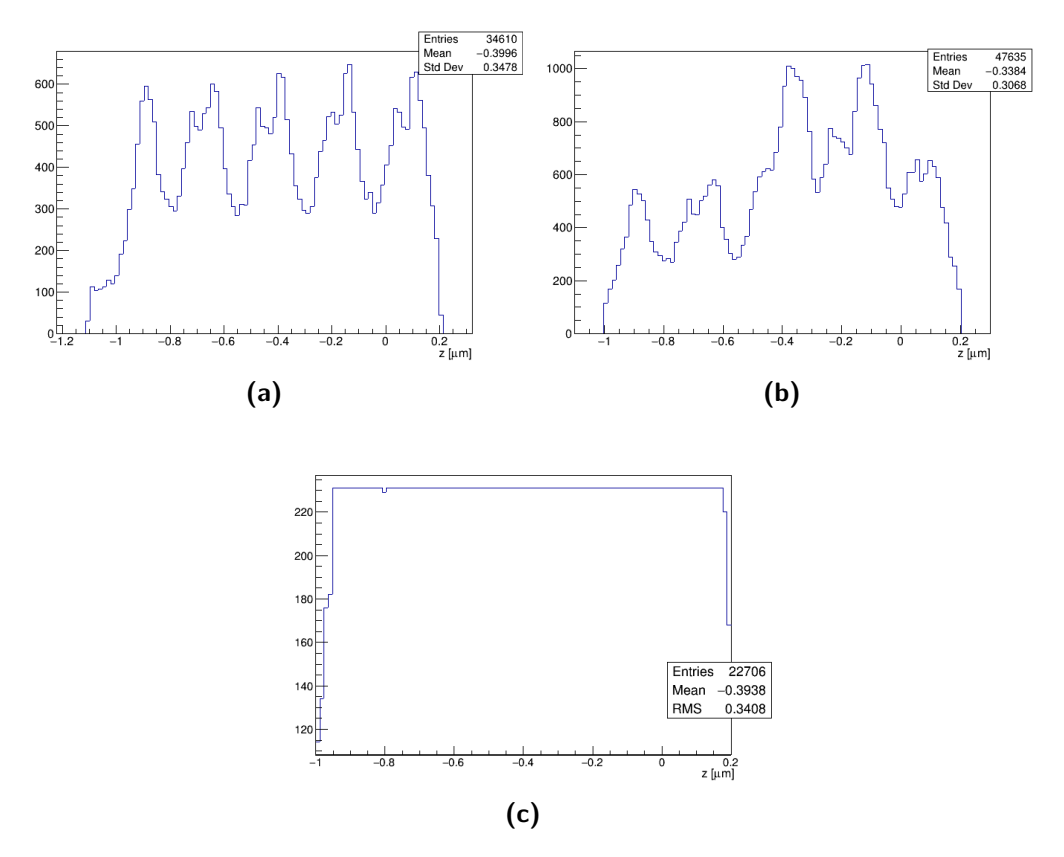


Figure 5.5: Three datasets that represent the smallest z, used as a reference and necessary for the prediction of z-coordinates, of the two merged image. (a) small dataset with peaks, (b) big dataset with peaks, (c) uniform dataset.

While the mean squared error computes the mean of squares of errors between z_true and z_pred following:

$$loss = square(z_true - z_pred)$$

5.2.1 Small dataset with peaks

The difference between the frame First and frame Last larger than 4 was selected to obtain the small dataset with 5 peaks. Some of the tests made on this dataset are reported in table 5.1. In that table, it is possible to observe that larger values correspond to the loss function MAPE while the smaller

Epochs	Batch size	Drop out	loss function	σ [nm]
400	8	0.4	MAPE	53.8 ± 1.4
400	32	0.4	MAPE	
400	4	0.4	MAPE	84.5 ± 3.6
400	8	0.4	MSE	49.1 ± 0.7
400	8	0.4	MSE	48.5 ± 0.7
400	16	0.4	MSE	45.6 ± 0.6

Table 5.1: Resolution as a function of different parameters for the dataset five peaks.

ones to the MSE.

Figure 5.6 shows plots obtained on the small dataset using 400 epochs, batch size of 8, drop out of 0.4 and the mean absolute percentage error as the loss function.

Histogram 5.6a represent the 20% of the histogram in 5.5a since these percentage was chosen as test, while histogram 5.6b shows the corresponding values predicted from the CNN. It is evident that even if there are some peaks these are not in the correct position. This is even more evident in the scatter plot, the difference between values predicted and values of test is computed as: $\Delta z = z_{pred} - z_{test}$ and is plotted versus z tested values. Here a straight line parallel to x-axis is expected but not obtained with these parameters (see 5.6c). Finally Δz values are reported in the histogram (Figure 5.6d). Δz distribution is expected to be Gaussian while in Figure 5.6d a partial Gaussian fit provided a value of $\sigma = (53.8 \pm 1.4)$ nm.

Using the same dataset, the MSE loss function, 400 epochs, batch size of 16 and drop out of 0.4 the plot shown in Figure 5.7 are obtained. Significant improvements are observed in all these plots, starting from z predicted histogram (see 5.7b) the five peaks are visible, then in the scatter plot 5.7c a straight line parallel to x-axes is evident. Finally Δz distribution (see 5.7d) is Gaussian and the fit returns $\sigma = (45.6 \pm 0.6)$ nm.

Other plots for the remaining parameters tested on the small dataset are reported in the Appendix.

Epochs	Batch size	Drop out	loss function	σ [nm]
400	16	0.4	MSE	58.3 ± 0.9
400	16	0.5	MSE	57.0 ± 0.8
400	16	0.6	MSE	63.6 ± 1.1
30	16	0.5	MSE	74.0 ± 0.6
250	16	0.5	MSE	59.5 ± 1.9
400	64	0.5	MSE	72.9 ± 1.9
600	64	0.5	MSE	

Table 5.2: Resolution as a function of different parameters for the dataset five peaks big.

5.2.2 Large dataset with peaks

Moving to the dataset with the increased statistic, several tests made are reported in table 5.2. The difference between the frame First and frame Last larger than 2 was selected to obtain this dataset. Since the improvement obtained with the MSE loss function was significant, this parameter was not changed anymore.

Figure 5.8 shows plots obtained using 400 epochs, 16 batch size and drop out 0.5. The histogram of z predicted in Figure 5.8b shows the five peaks even if there is a huge bin. The linearity in the scatter plot of Δz versus z tested was respected (Figure 5.8c) since the straight line parallel to x-axes is visible and the observed trend reflects the expected one. Even in this case Δz distribution, shown in Figure 5.8d is Gaussian and the fit returns $\sigma = (57.0 \pm 0.8)$ nm.

For plots obtained with the other parameters, it is possible to have a look in the Appendix.

5.2.3 Uniform dataset

To test the performance of the CNN on a dataset not influenced by the acquisition scanning method, the uniform dataset was obtained. All the test made are reported in the Appendix, while in Figure 5.9 are reported the plot achieved with 200 epochs, batch size of 16 and a drop out of 0.4. Also here the histogram of z test in Figure 5.9a is the 20% of the dataset in Figure 5.5c. In Figure 5.9b, the peak in the leftmost bin of the histogram can be attributed to the insufficiently good prediction of the network since the picture contrast

Epochs	Batch size	Drop out	loss function	σ [nm]
400	16	0.5	MSE	
200	16	0.5	MSE	62.3 ± 1.6
200	32	0.5	MSE	61.3 ± 1.6
200	8	0.5	MSE	62.6 ± 1.4
200	16	0.4	MSE	57.4 ± 1.3
200	32	0.4	MSE	68.1 ± 2.2

Table 5.3: Resolution as a function of different parameters for the uniform dataset.

rapidly decreases with the distance to the focal plane. Correlation scatter plot in Figure 5.9c preserved the expected linearity. Finally, Δz distribution is Gaussian (see 5.9d) and the fit returns a value of $\sigma = (57.4 \pm 1.4)$ nm.

Afterwards, other tests were performed changing this time a layer of the convolutional neural network. In particular, the max-pooling layer was replaced by the average pooling layer, since input images for this study can have some brighter pixel not due to the physics.

This test was performed for two-run, the first on the uniform dataset and the second on the big dataset with peaks. For both of them the parameters granting the best performance were used. The corresponding plots are reported for the former in Figure 5.10 and for the latter in Figure 5.11.

Using that layer, the performances of the network seem to be overall improved. On the uniform dataset a $\sigma = (57.1 \pm 1.3)$ nm was obtained, and for the large dataset with peaks $\sigma = (56.6 \pm 0.8)$ nm.

Other tests are currently under study since it is known that to obtain the best results with machine learning techniques it is fundamental tuning parameters. The number of tests made is influenced also by the computational time necessary to get the results, this time depends both on the network structure and on the size of the dataset used.

5.3 Improvements obtained by CNN

The Convolutional Neural Network configuration that returns the best performances include:

• batch size of 16;

- 200 epochs for the small dataset and 400 epochs for the bigger ones;
- drop out in the range [0.4; 0.5];
- mean squared error as loss function;
- average pooling layer.

With these parameters the best accuracy, obtained for each of the three datasets, results:

1. on the small dataset with peaks

$$\sigma = (45.6 \pm 0.6)nm$$

with an efficiency $\epsilon = 99.9\%$;

2. on the large dataset with peaks

$$\sigma = (57.0 \pm 0.8)nm$$

with an efficiency $\epsilon = 99.4\%$;

3. on the uniform dataset

$$\sigma = (57.4 \pm 1.3)nm$$

with an efficiency $\epsilon = 99.9\%$.

In conclusion, the accuracy achieved with this convolutional neural network overcome the one limited by diffraction by one order of magnitude.

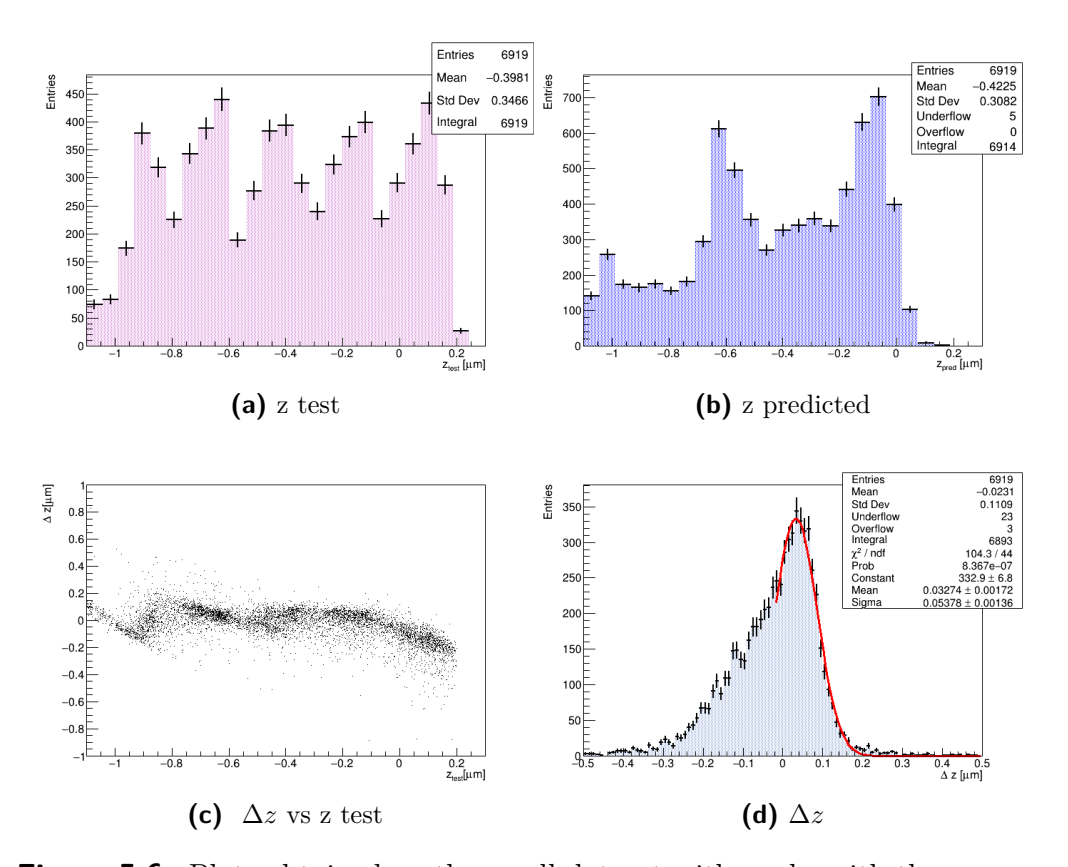


Figure 5.6: Plots obtained on the small dataset with peaks with the parameters: epochs 400, batch size 8, drop out 0.4 and mean absolute percentage error as loss function. (a) z values of test, (b) z values predicted from the CNN, (c) the difference between values predicted and values of test (Δz) versus z tested and (d) Δz .

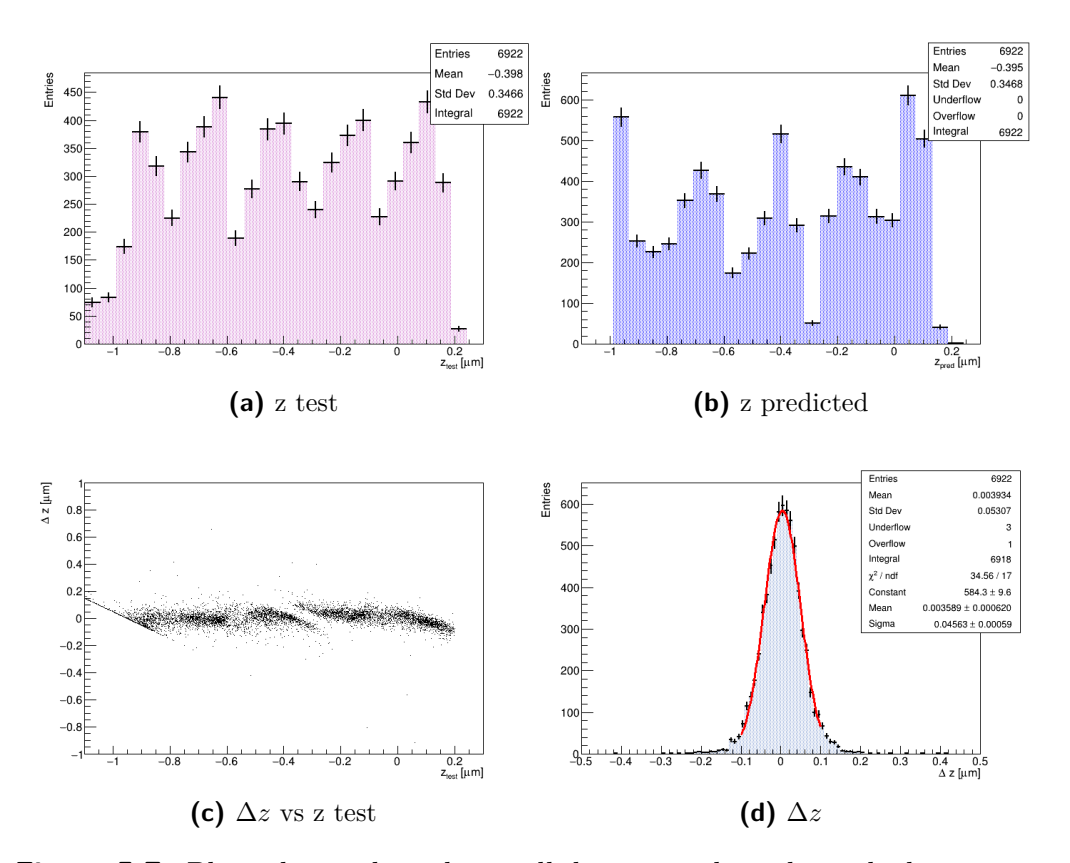


Figure 5.7: Plots obtained on the small dataset with peaks with the parameters: epochs 400, batch size 16, drop out 0.4 and mean squared error as loss function. (a) z values of test, (b) z values predicted from the CNN, (c) the difference between values predicted and values of test (Δz) versus z tested and (d) Δz .

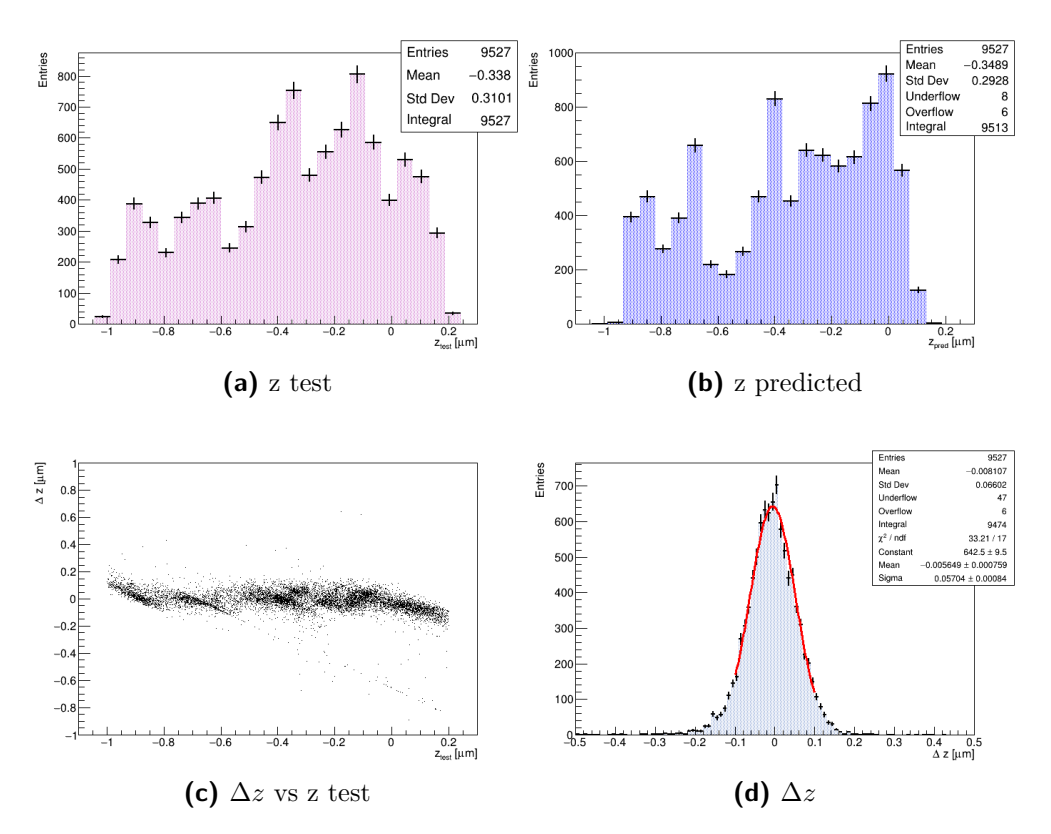


Figure 5.8: Plots obtained on the dataset big with peaks with the parameters: epochs 400, batch size 16, drop out 0.5 and mean squared error as loss function. (a) z values of test, (b) z values predicted from the CNN, (c) the difference between values predicted and values of test (Δz) versus z tested and (d) Δz .

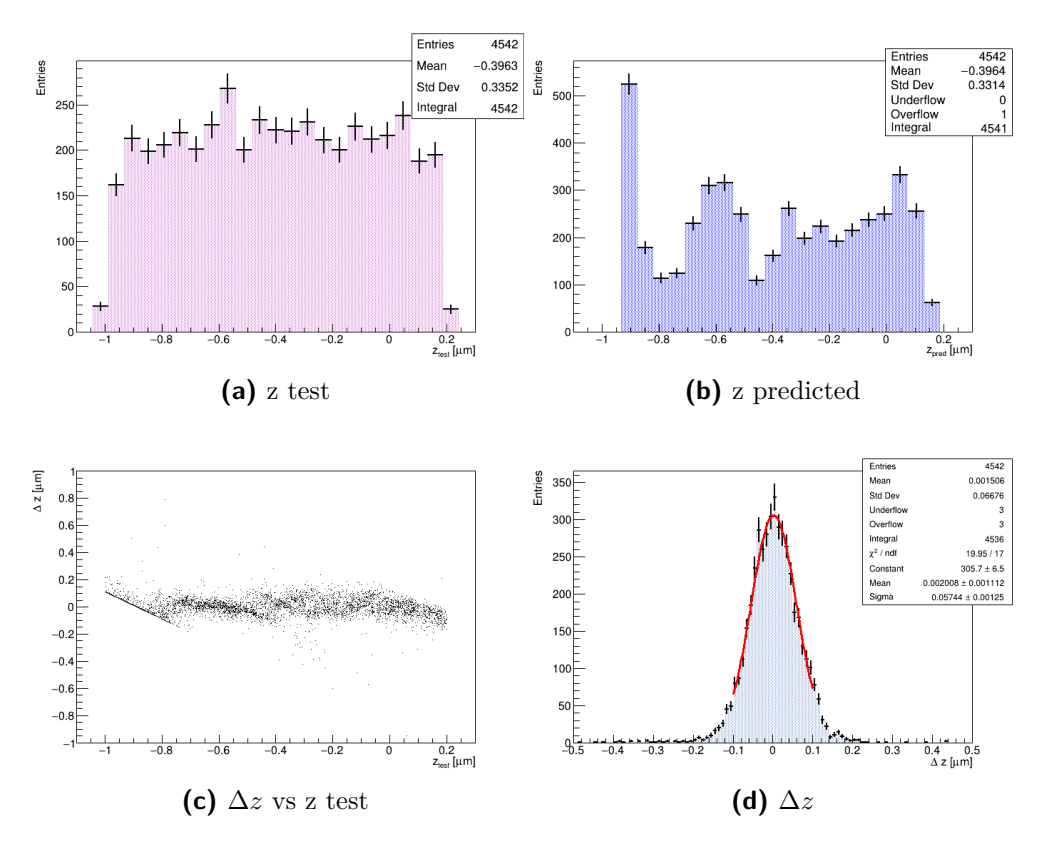


Figure 5.9: Plots obtained with the uniform dataset with the parameters: epochs 200, batch size 16, drop out 0.4 and mean squared error as loss function. (a) z values of test, (b) z values predicted from the CNN, (c) the difference between values predicted and values of test (Δz) versus z tested and (d) Δz .

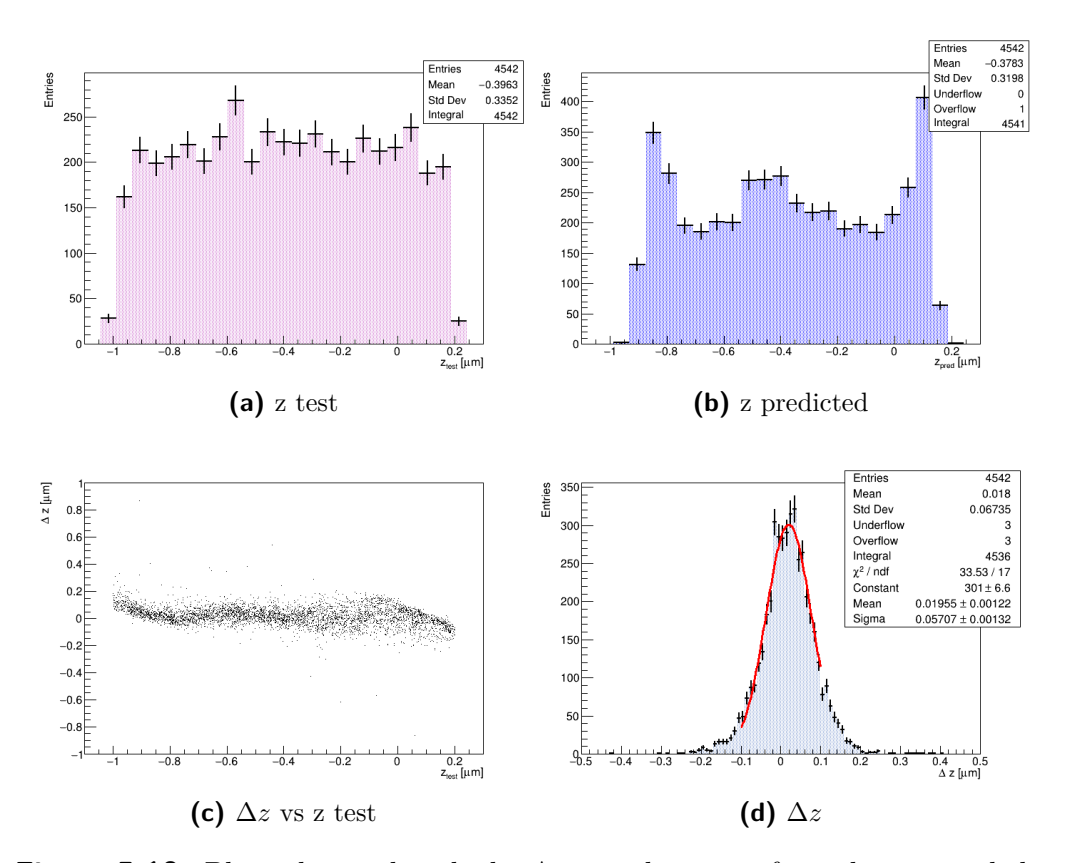


Figure 5.10: Plots obtained with the Average layer, uniform dataset and the parameters: epochs 200, batch size 16, drop out 0.4 and mean squared error as loss function. (a) z values of test, (b) z values predicted from the CNN, (c) the difference between values predicted and values of test (Δz) versus z tested and (d) Δz .

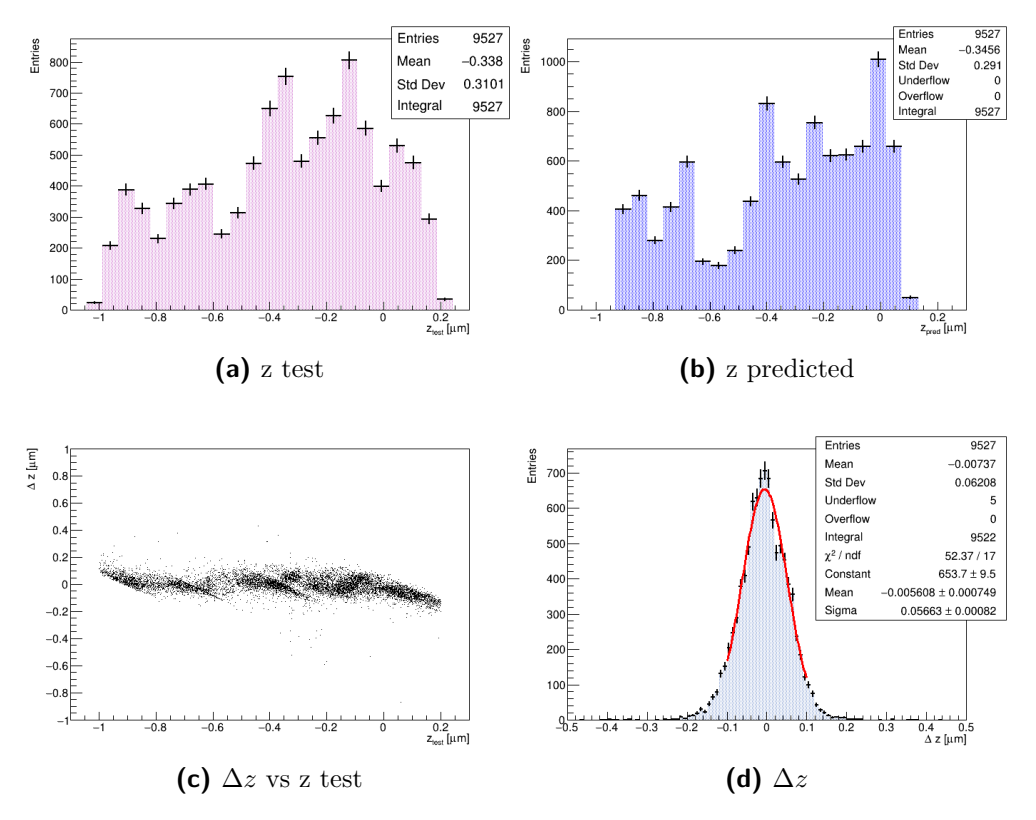


Figure 5.11: Plots obtained with the Average layer, big dataset with peaks and the parameters: epochs 400, batch size 16, drop out 0.5 and mean squared error as loss function. (a) z values of test, (b) z values predicted from the CNN, (c) the difference between values predicted and values of test (Δz) versus z tested and (d) Δz .

Conclusion

The aim of NEWSdm (Nuclear Emulsion for WIMP Search with directional measurements) is the detection of dark matter by measuring the direction of WIMP-induced nuclear recoils. The development of new emulsion films with 40 nm AgBr crystals, named Nano Imaging Trackers (NIT), paves the way for the detection and reconstruction of sub-micrometric tracks similar to those produced by a WIMP interaction with the emulsion target.

The super-resolution optical microscope allows a first step of the track reconstruction with the "shape analysis", i.e. to distinguish the clusters produced by a single grain (fog) due to thermal excitation, showing a spherical shape, from clusters formed by several grains showing, instead, an elliptical shape with the major axis along the actual direction of the trajectory of nuclear recoils. The second step of the analysis is performed employing a new optical microscope which allows extending the reconstruction of tracks beyond the diffraction limit by exploiting the resonance effect of polarized light with an accuracy better than 10 nm.

In this work 70 nm diameter grains NIT emulsion, implanted with Carbon ions with energies of 100, 60 and 30 keV, have been analyzed using both the shape analysis for the candidate selection and the plasmon analysis for the validation. With the plasmon analysis an angular accuracy of $\sigma = 0.35 \pm 0.02$ rad was obtained with a corresponding efficiency of 35% for the 100 keV sample.

In order to perform a 3d reconstruction of the track also a high accuracy for z-coordinates is needed. Actually, under ideal conditions, the accuracy is of the order of ~ 400 nm. The axial resolution is limited by both the diffraction process and the wave nature of the light. In particular, an object is still seen in focus if it is within the depth of focus, moreover, near the focal plane the point spread function (PSF) shows very small variations, thus providing a bad z localization while out of focus PSF changes rapidly and a good z

localization is obtained.

From here the idea of combining two focal planes with a distance larger than the Depth of Focus (DoF) in order to always have the object in focus in one of the planes. Analyzing the difference in PSFs visible simultaneously at both planes, one can estimate the z coordinate of the object.

This work was made with the use of a suitable convolutional neural network. A tuning on the hyperparameters both that determines the network structure and that determines the network training was made.

The best accuracy that has been obtained is of $\sigma = (45.6 \pm 0.6)$ nm with an efficiency of 99.9% so overcoming the diffraction limit by one order of magnitude.

Appendix A

In this section are reported the other plot obtained, changing parameter, to test the network. In Figure 5.12, 5.13, 5.14 and 5.15 are shown plots from the small dataset with five peaks. For the dataset big with peaks the graphs are in Figure 5.16, 5.17, 5.18, 5.19, 5.20 and 5.21. Finally, in Figure 5.22, 5.23, 5.24, 5.25 and 5.26 are displayed the results on the dataset uniform.

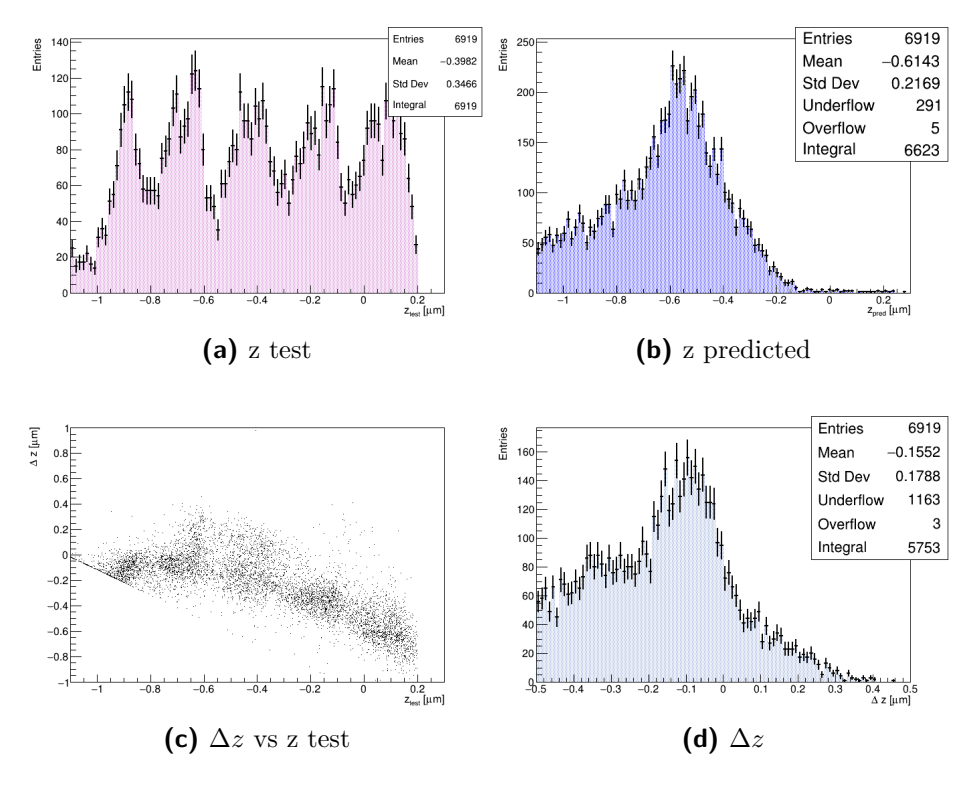


Figure 5.12: Plots obtained with the parameters: epochs 400, batch size 32, drop out 0.4 and mean absolute percentage error as loss function. (a) z values of test, (b) z values predicted from the CNN, (c) the difference between values predicted and values of test (Δz) versus z tested and (d) Δz .

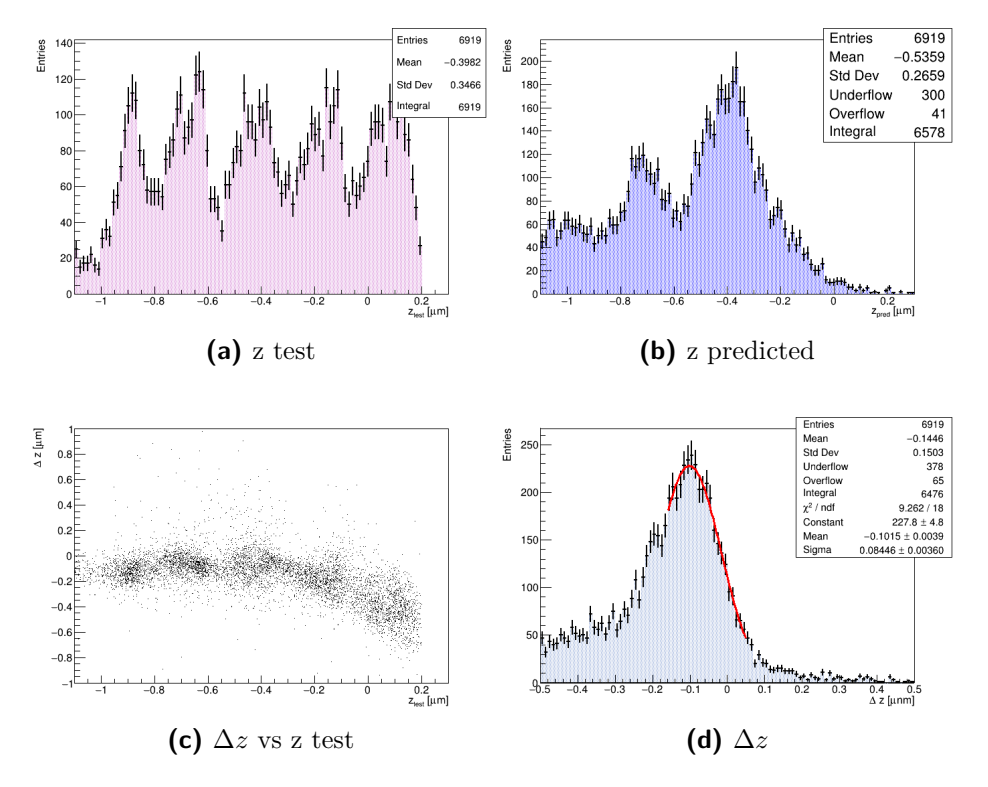


Figure 5.13: Plots obtained with the parameters: epochs 400, batch size 4, drop out 0.4 and mean absolute percentage error as loss function. (a) z values of test, (b) z values predicted from the CNN, (c) the difference between values predicted and values of test (Δz) versus z tested and (d) Δz .

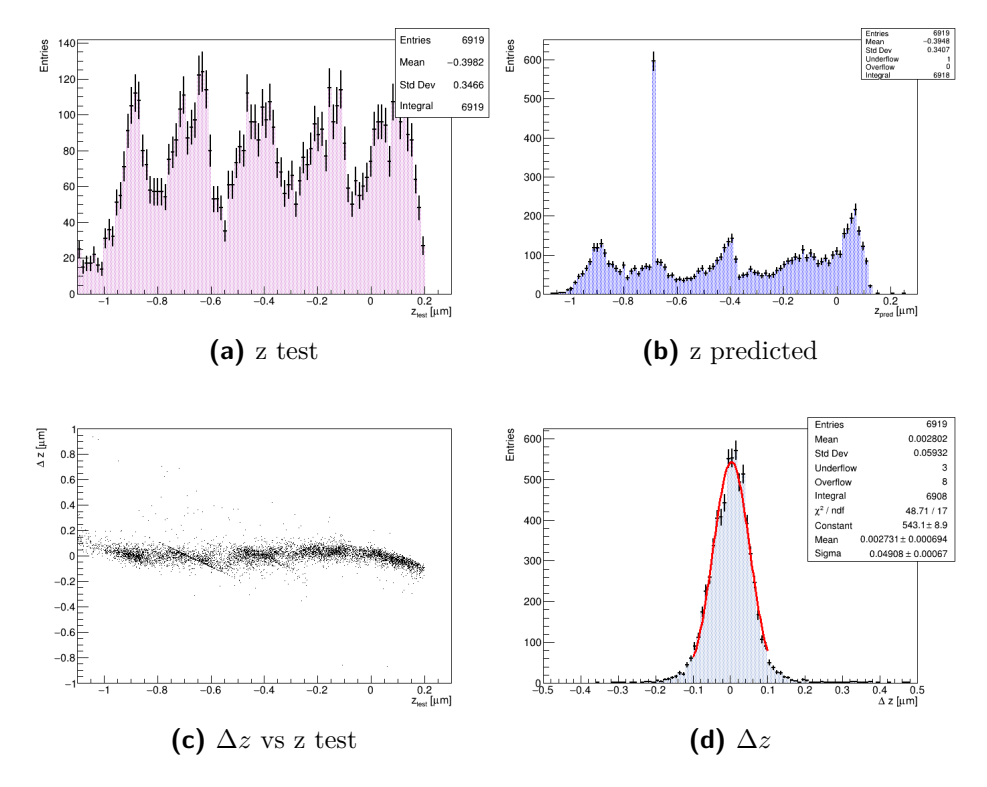


Figure 5.14: Plots obtained with the parameters: epochs 400, batch size 8, drop out 0.4 and mean squared error as loss function. (a) z values of test, (b) z values predicted from the CNN, (c) the difference between values predicted and values of test (Δz) versus z tested and (d) Δz .

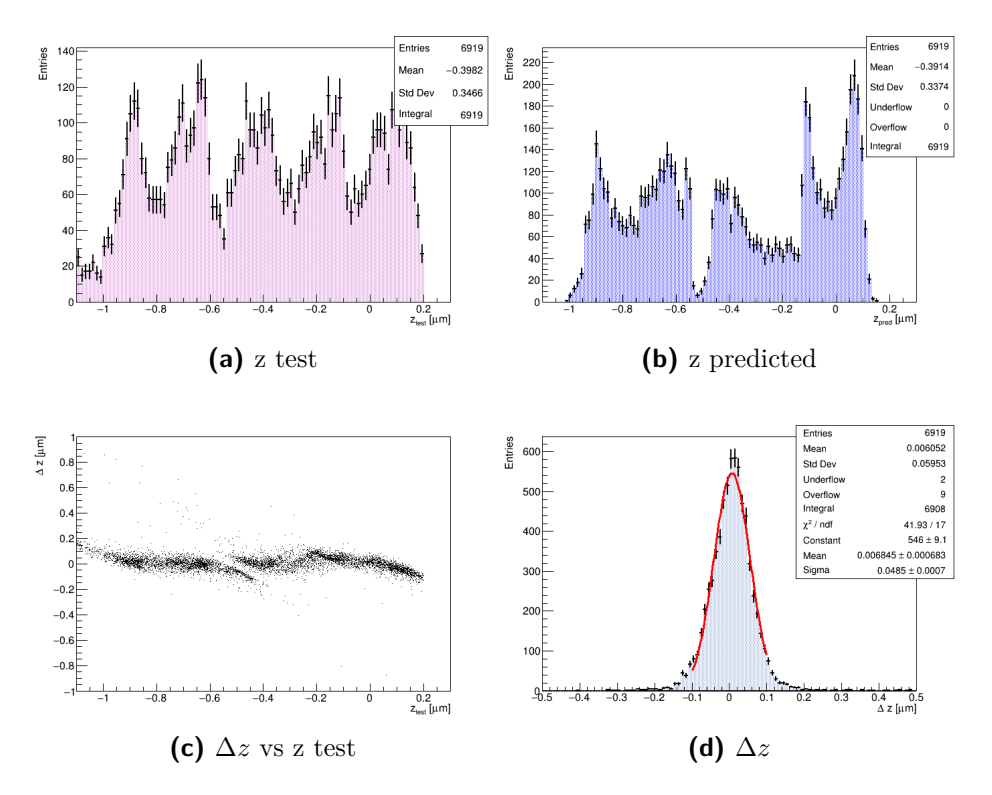


Figure 5.15: Plots obtained with the parameters: epochs 400, batch size 8, drop out 0.4 and mean squared error as loss function. (a) z values of test, (b) z values predicted from the CNN, (c) the difference between values predicted and values of test (Δz) versus z tested and (d) Δz .

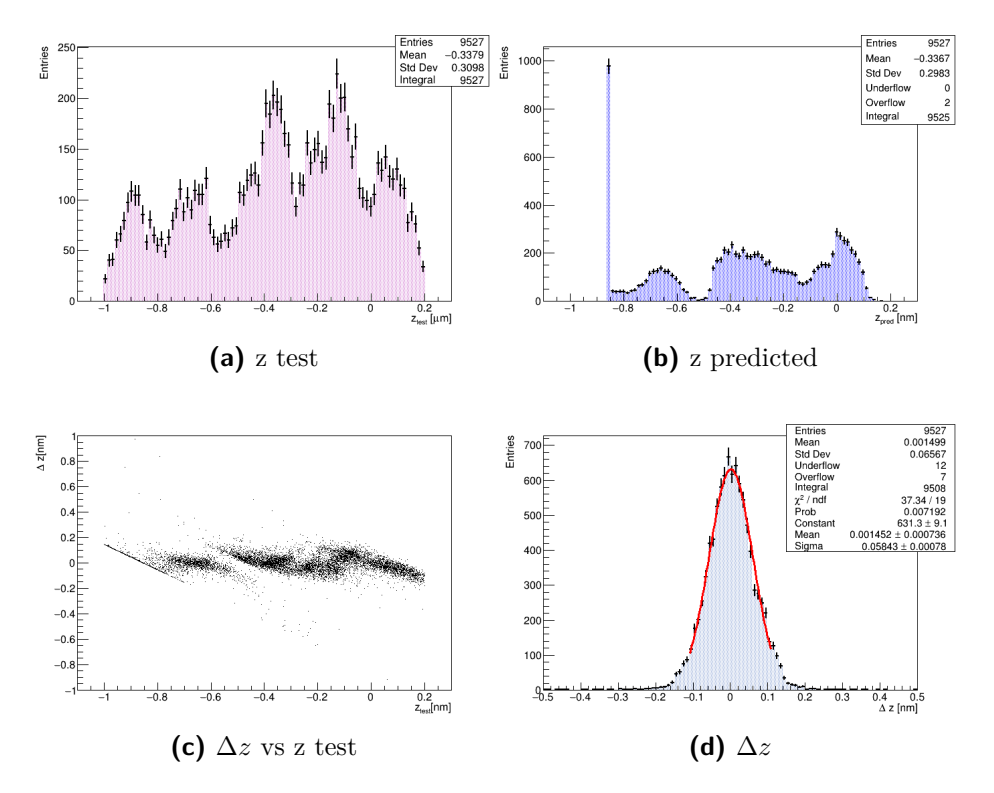


Figure 5.16: Plots obtained with the parameters: epochs 400, batch size 16, drop out 0.4 and mean squared error as loss function. (a) z values of test, (b) z values predicted from the CNN, (c) the difference between values predicted and values of test (Δz) versus z tested and (d) Δz .

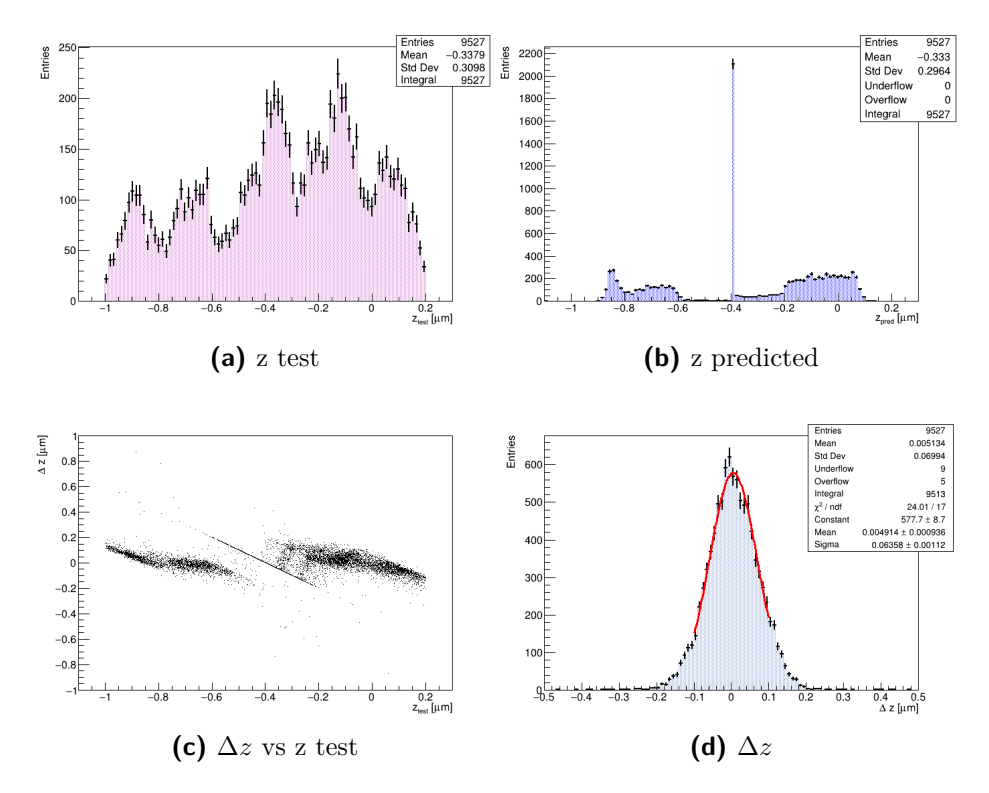


Figure 5.17: Plots obtained with the parameters: epochs 400, batch size 16, drop out 0.6 and mean squared error as loss function. (a) z values of test, (b) z values predicted from the CNN, (c) the difference between values predicted and values of test (Δz) versus z tested and (d) Δz .

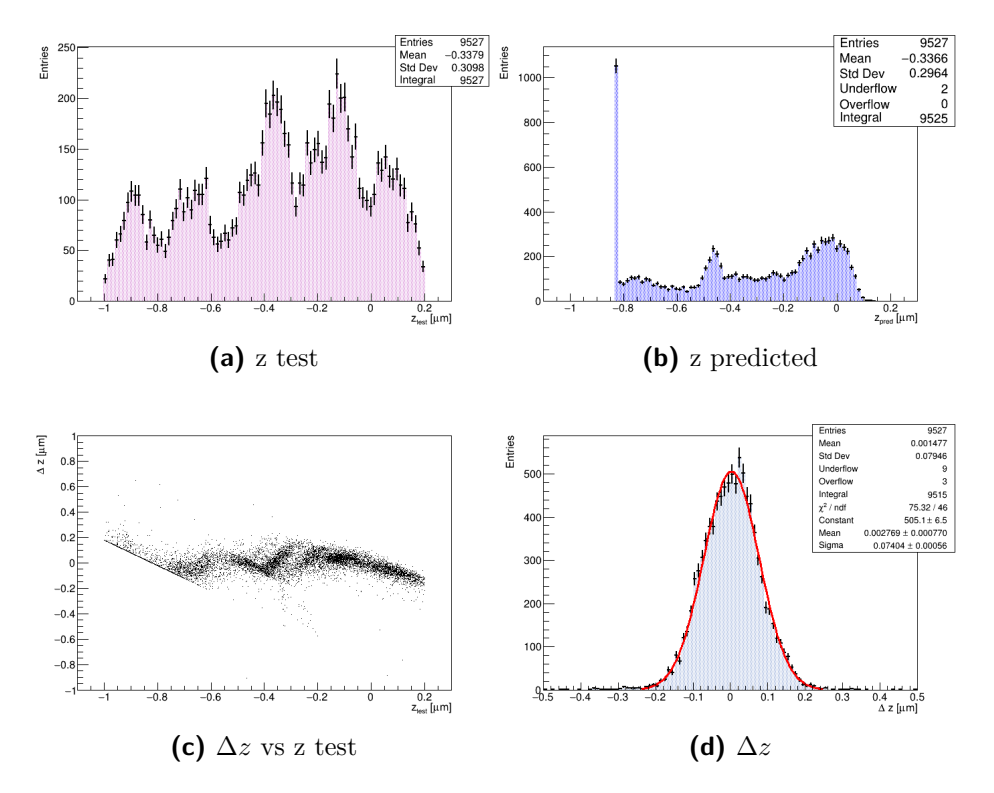


Figure 5.18: Plots obtained with the parameters: epochs 30, batch size 16, drop out 0.5 and mean squared error as loss function. (a) z values of test, (b) z values predicted from the CNN, (c) the difference between values predicted and values of test (Δz) versus z tested and (d) Δz .

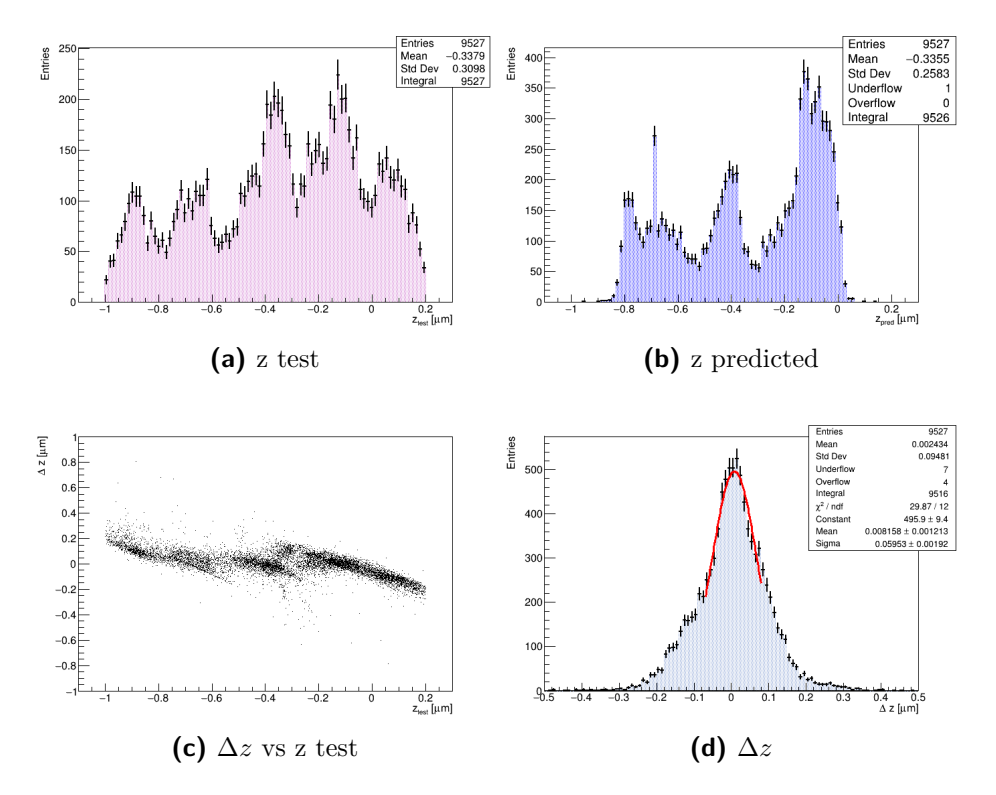


Figure 5.19: Plots obtained with the parameters: epochs 250, batch size 16, drop out 0.5 and mean squared error as loss function. (a) z values of test, (b) z values predicted from the CNN, (c) the difference between values predicted and values of test (Δz) versus z tested and (d) Δz .

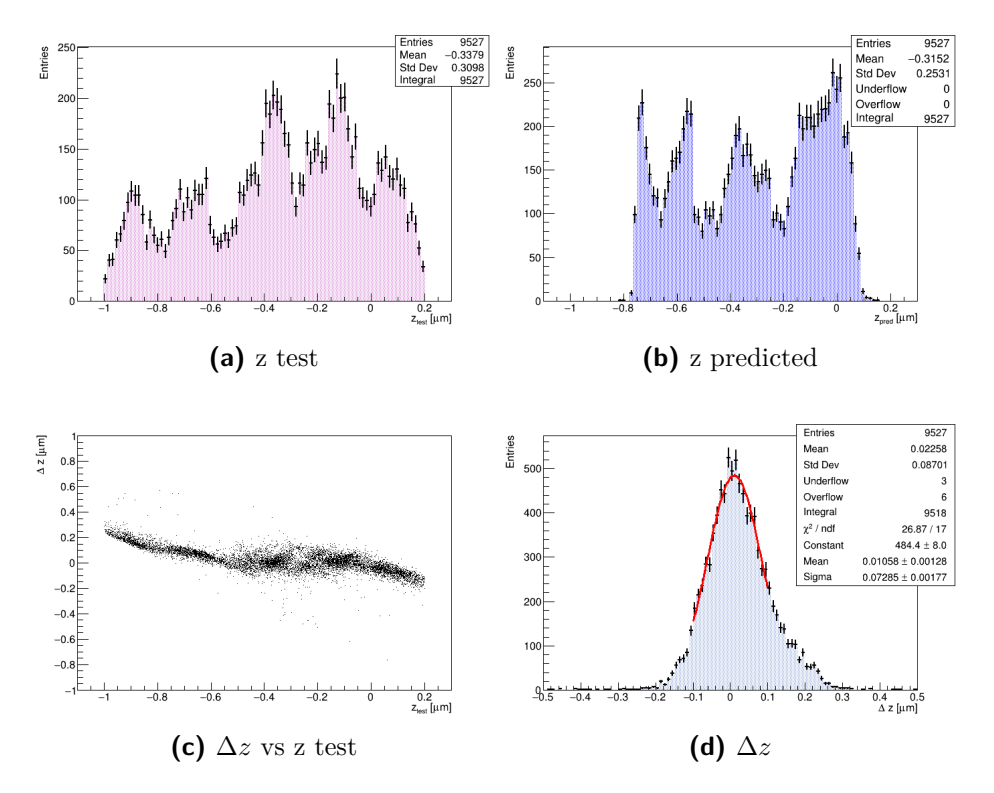


Figure 5.20: Plots obtained with the parameters: epochs 400, batch size 64, drop out 0.5 and mean squared error as loss function. (a) z values of test, (b) z values predicted from the CNN, (c) the difference between values predicted and values of test (Δz) versus z tested and (d) Δz .

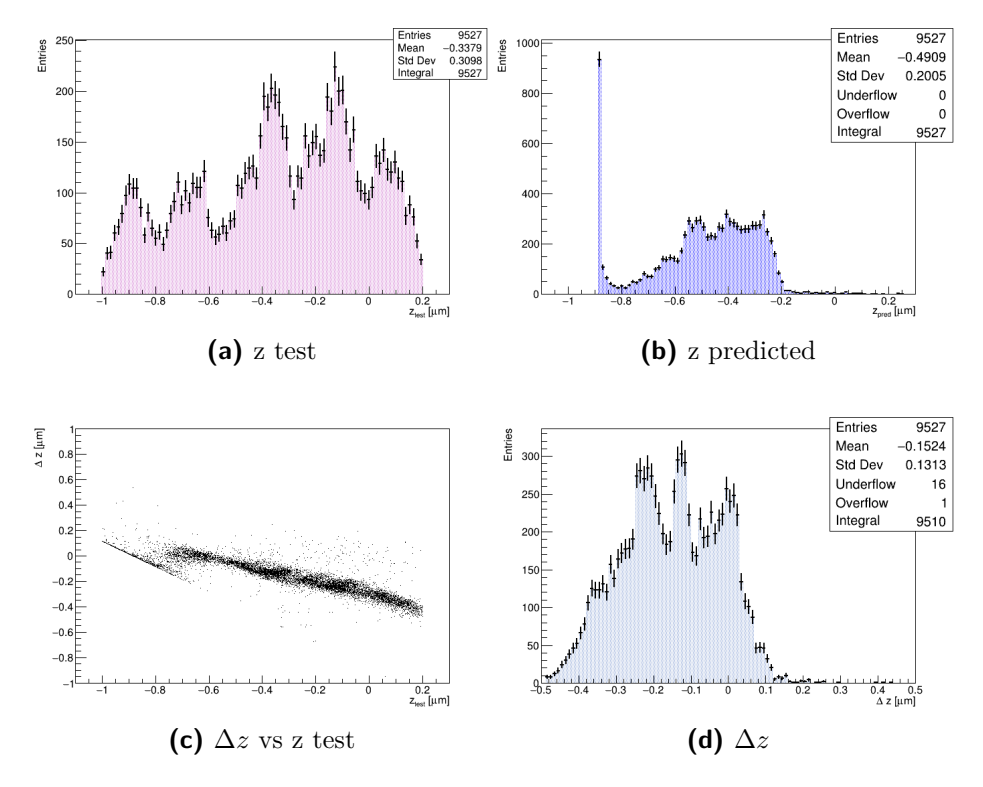


Figure 5.21: Plots obtained with the parameters: epochs 600, batch size 64, drop out 0.5 and mean squared error as loss function. (a) z values of test, (b) z values predicted from the CNN, (c) the difference between values predicted and values of test (Δz) versus z tested and (d) Δz .

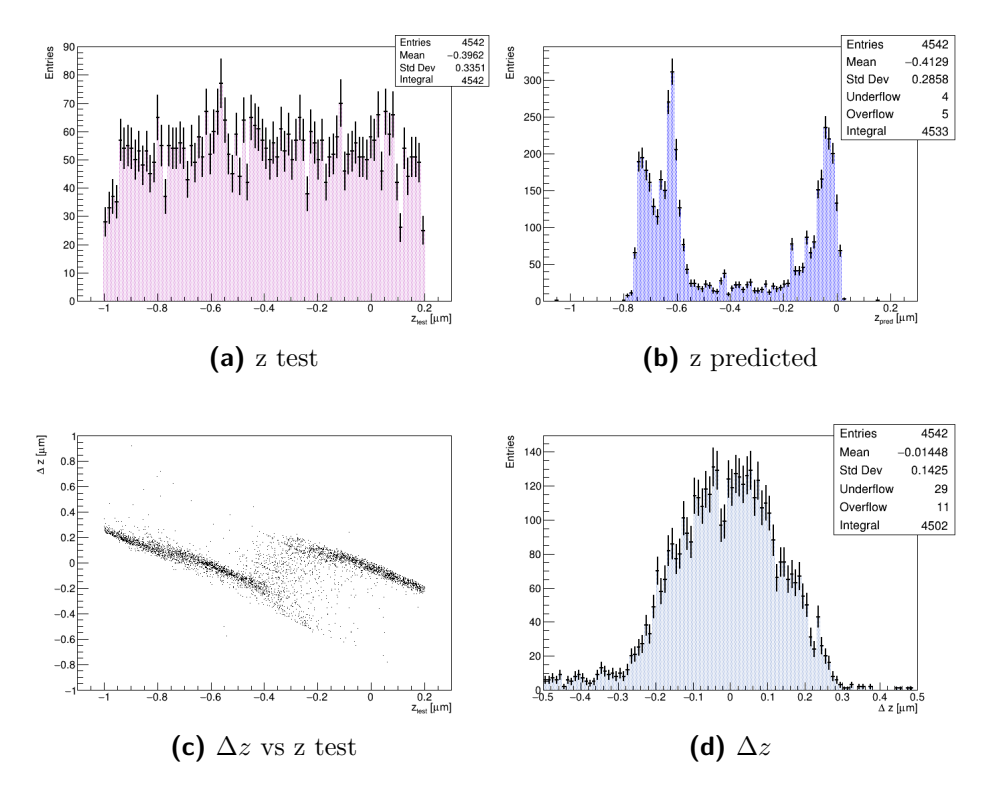


Figure 5.22: Plots obtained with the parameters: epochs 400, batch size 16, drop out 0.5 and mean squared error as loss function. (a) z values of test, (b) z values predicted from the CNN, (c) the difference between values predicted and values of test (Δz) versus z tested and (d) Δz .

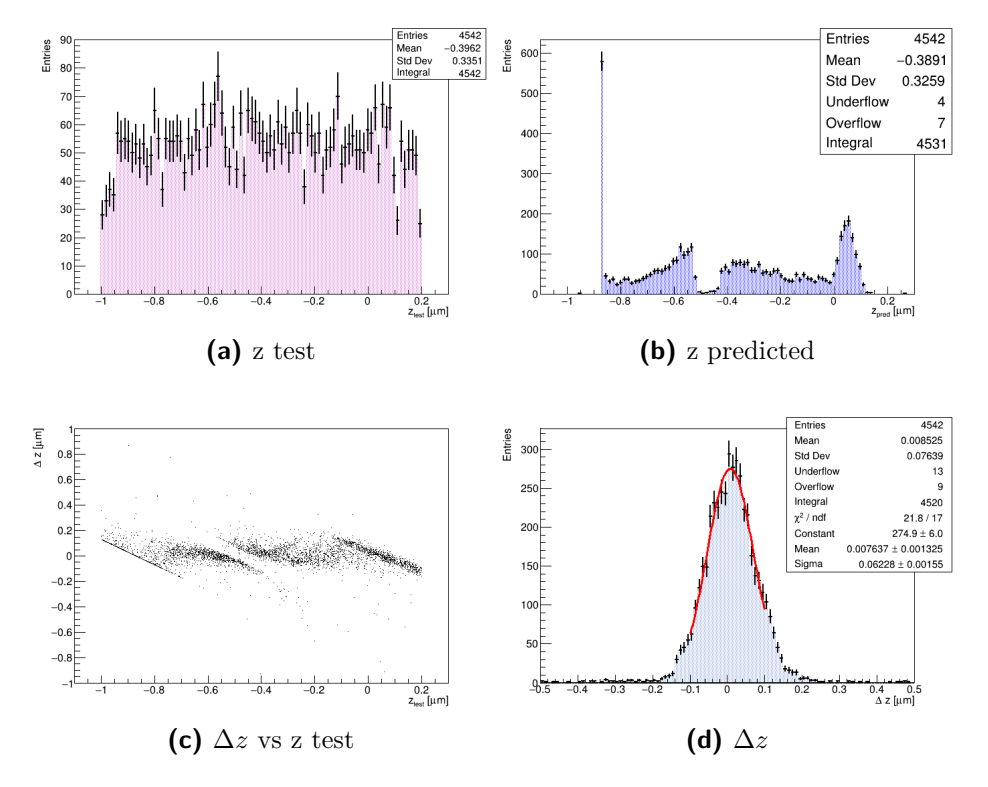


Figure 5.23: Plots obtained with the parameters: epochs 200, batch size 16, drop out 0.5 and mean squared error as loss function. (a) z values of test, (b) z values predicted from the CNN, (c) the difference between values predicted and values of test (Δz) versus z tested and (d) Δz .

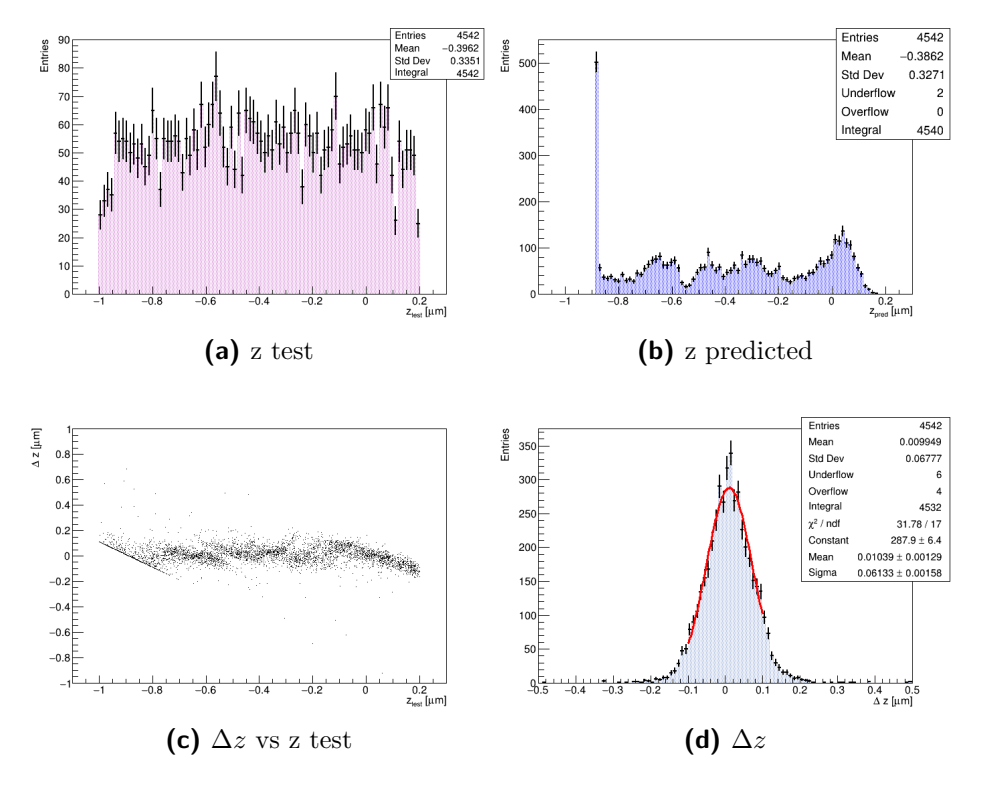


Figure 5.24: Plots obtained with the parameters: epochs 200, batch size 32, drop out 0.5 and mean squared error as loss function. (a) z values of test, (b) z values predicted from the CNN, (c) the difference between values predicted and values of test (Δz) versus z tested and (d) Δz .

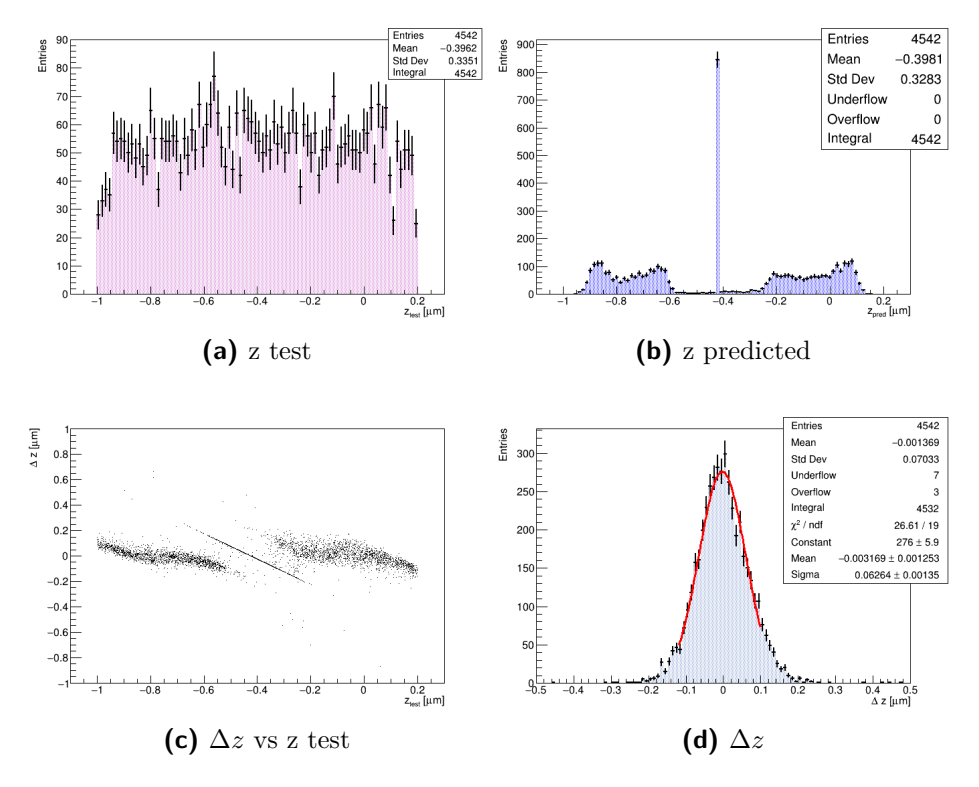


Figure 5.25: Plots obtained with the parameters: epochs 200, batch size 8, drop out 0.5 and mean squared error as loss function. (a) z values of test, (b) z values predicted from the CNN, (c) the difference between values predicted and values of test (Δz) versus z tested and (d) Δz .

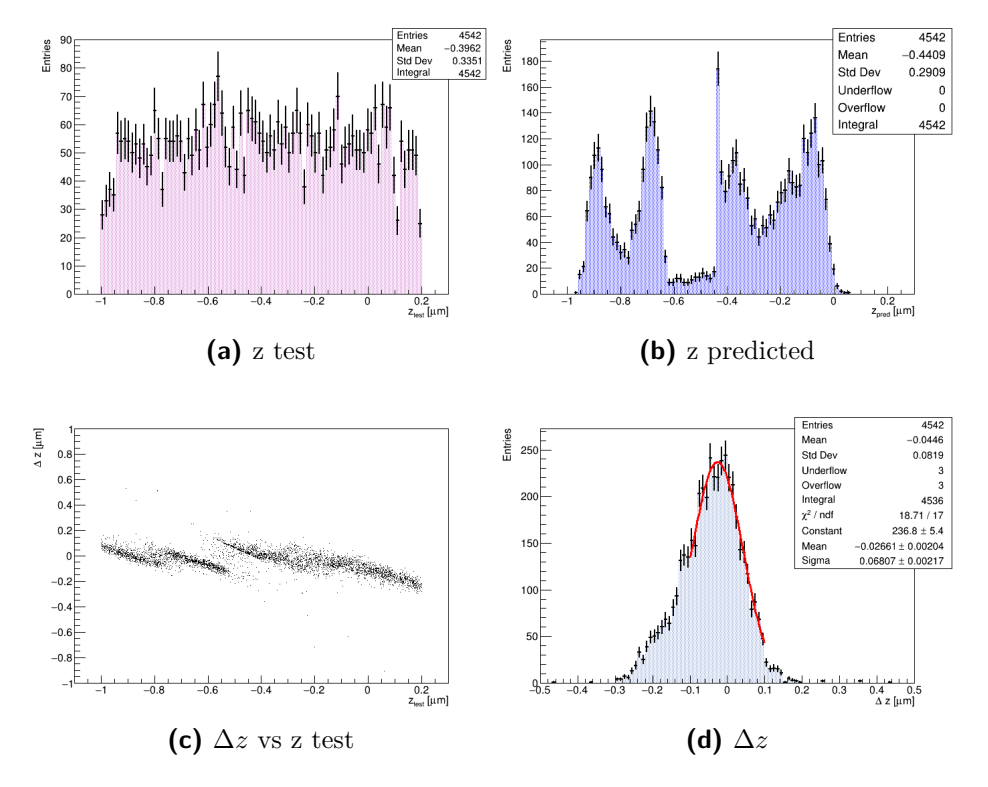


Figure 5.26: Plots obtained with the parameters: epochs 200, batch size 32, drop out 0.4 and mean squared error as loss function. (a) z values of test, (b) z values predicted from the CNN, (c) the difference between values predicted and values of test (Δz) versus z tested and (d) Δz .

- [1] Fritz Zwicky. "The redshift of extragalactic nebulae". In: *Helvetica Physica Acta* 6 (1933), pp. 110–127 (p. 3).
- [2] Vera C Rubin and W Kent Ford Jr. "Rotation of the Andromeda nebula from a spectroscopic survey of emission regions". In: *The Astrophysical Journal* 159 (1970), p. 379 (p. 4).
- [3] Vera C Rubin. "Dark matter in spiral galaxies". In: Scientific American 248.6 (1983), pp. 96–109 (p. 4).
- [4] KG Begeman. "HI rotation curves of spiral galaxies. I-NGC 3198". In: Astronomy and Astrophysics 223 (1989), pp. 47–60 (p. 5).
- [5] Richard Massey, Thomas Kitching, and Johan Richard. "The dark matter of gravitational lensing". In: *Reports on Progress in Physics* 73.8 (2010), p. 086901 (p. 4).
- [6] Matthias Bartelmann. "Gravitational lensing". In: Classical and Quantum Gravity 27.23 (2010), p. 233001 (p. 4).
- [7] Dennis Walsh, Robert F Carswell, and Ray J Weymann. "0957+ 561 A,
 B: twin quasistellar objects or gravitational lens?" In: Nature 279.5712 (1979), pp. 381-384 (p. 4).
- [8] Donald H Perkins. *Particle astrophysics*. 10. Oxford University Press, 2009 (pp. 4, 9).
- [9] Bohdan Paczynski. "Gravitational microlensing by the galactic halo". In: *The Astrophysical Journal* 304 (1986), pp. 1–5 (p. 4).
- [10] Patrick Tisserand et al. "Limits on the Macho Content of the Galactic Halo from the EROS-2 Survey of the Magellanic Clouds". In: Astronomy & Astrophysics 469.2 (2007), pp. 387–404 (p. 5).

[11] Charles Alcock et al. "The MACHO project: microlensing results from 5.7 years of Large Magellanic Cloud observations". In: *The Astrophysical Journal* 542.1 (2000), p. 281 (p. 5).

- [12] N Miyake et al. "A sub-Saturn mass planet, MOA-2009-BLG-319Lb". In: *The Astrophysical Journal* 728.2 (2011), p. 120 (p. 5).
- [13] Andrzej Udalski. "The optical gravitational lensing experiment. Real time data analysis systems in the OGLE-III survey". In: arXiv preprint astro-ph/0401123 (2004) (p. 5).
- [14] Douglas Clowe et al. "A direct empirical proof of the existence of dark matter". In: *The Astrophysical Journal Letters* 648.2 (2006), p. L109 (p. 6).
- [15] M Markevitch, D Clowe, et al. "The matter of the bullet cluster". In: NASA. gov, Aug 26 (2006) (p. 6).
- [16] Arno A Penzias and Robert Woodrow Wilson. "A measurement of excess antenna temperature at 4080 Mc/s." In: *The Astrophysical Journal* 142 (1965), pp. 419–421 (p. 6).
- [17] George F Smoot et al. "Structure in the COBE differential microwave radiometer first-year maps". In: *The Astrophysical Journal* 396 (1992), pp. L1–L5 (p. 7).
- [18] Gary Hinshaw et al. "Five-year wilkinson microwave anisotropy probe" observations: data processing, sky maps, and basic results". In: *The Astrophysical Journal Supplement Series* 180.2 (2009), p. 225 (p. 7).
- [19] Peter AR Ade et al. "Planck 2013 results. XVI. Cosmological parameters". In: Astronomy & Astrophysics 571 (2014), A16 (p. 7).
- [20] D Larson et al. "Seven-year wilkinson microwave anisotropy probe (WMAP*) observations: power spectra and WMAP-derived parameters". In: *The Astrophysical Journal Supplement Series* 192.2 (2011), p. 16 (p. 7).
- [21] David N Spergel et al. "Three-year Wilkinson Microwave Anisotropy Probe (WMAP) observations: implications for cosmology". In: *The Astrophysical Journal Supplement Series* 170.2 (2007), p. 377 (pp. 7, 11).

[22] Richard H Cyburt. "Primordial nucleosynthesis for the new cosmology: Determining uncertainties and examining concordance". In: *Physical Review D* 70.2 (2004), p. 023505 (p. 8).

- [23] N Aghanim et al. "Planck 2018 results. VI. Cosmological parameters". In: arXiv preprint arXiv:1807.06209 (2018) (p. 8).
- [24] Peter AR Ade et al. "Planck 2015 results-xiii. cosmological parameters". In: Astronomy & Astrophysics 594 (2016), A13 (p. 8).
- [25] K Garrett and G Duda. "Dark matter: a primer, Adv. Astron. 2011 (2011) 968283". In: arXiv preprint arXiv:1006.2483 () (p. 8).
- [26] Gianfranco Bertone, Dan Hooper, and Joseph Silk. "Particle dark matter: Evidence, candidates and constraints". In: *Physics reports* 405.5-6 (2005), pp. 279–390 (p. 9).
- [27] Lars Bergström. "Dark matter candidates". In: New Journal of Physics 11.10 (2009), p. 105006 (p. 9).
- [28] Gerard Jungman, Marc Kamionkowski, and Kim Griest. "Supersymmetric dark matter". In: *Physics Reports* 267.5-6 (1996), pp. 195–373 (p. 10).
- [29] JD Lewin and PF Smith. Review of mathematics, numerical factors, and corrections for dark matter experiments based on elastic nuclear recoil. Tech. rep. SCAN-9603159, 1996 (pp. 10, 13, 14).
- [30] Lars Bergström, Piero Ullio, and James H Buckley. "Observability of γ rays from dark matter neutralino annihilations in the Milky Way halo". In: *Astroparticle Physics* 9.2 (1998), pp. 137–162 (p. 10).
- [31] J Richard Bond, George Efstathiou, and Joseph Silk. "Massive neutrinos and the large-scale structure of the universe". In: *Physical Review Letters* 45.24 (1980) (p. 11).
- [32] N Jarosik et al. "Seven-year wilkinson microwave anisotropy probe (WMAP*) observations: sky maps, systematic errors, and basic results". In: *The Astrophysical Journal Supplement Series* 192.2 (2011), p. 14 (p. 11).
- [33] Stephen P Martin. "A supersymmetry primer". In: *Perspectives on supersymmetry II*. World Scientific, 2010, pp. 1–153 (p. 11).
- [34] Xiao-Jun Bi, Peng-Fei Yin, and Qiang Yuan. "Status of dark matter detection". In: *Frontiers of Physics* 8.6 (2013), pp. 794–827 (p. 12).

[35] Georges Aad et al. "Search for dark matter candidates and large extra dimensions in events with a jet and missing transverse momentum with the ATLAS detector". In: *Journal of High Energy Physics* 2013.4 (2013), p. 75 (p. 11).

- [36] ATLAS collaboration et al. "The ATLAS Experiment at the CERN Large Hadron Collider, JINST 3 (2008) S08003". In: Cited on (2008), p. 24 (p. 11).
- [37] Serguei Chatrchyan et al. "Search for Dark Matter and Large Extra Dimensions in p p Collisions Yielding a Photon and Missing Transverse Energy". In: *Physical review letters* 108.26 (2012), p. 261803 (p. 11).
- [38] CMS Collaboration et al. The CMS experiment at the CERN LHC. 2008 (p. 11).
- [39] Jennifer M Gaskins. "A review of indirect searches for particle dark matter". In: *Contemporary Physics* 57.4 (2016), pp. 496–525 (p. 11).
- [40] LAT Collaboration et al. "Search for gamma-ray spectral lines with the Fermi large area telescope and dark matter implications". In: *arXiv* preprint arXiv:1305.5597 (2013) (p. 12).
- [41] G Kanbach et al. "The project EGRET (energetic gamma-ray experiment telescope) on NASA's Gamma-Ray Observatory GRO". In: *Space Science Reviews* 49.1-2 (1989), pp. 69–84 (p. 12).
- [42] Wim de Boer et al. "EGRET excess of diffuse galactic gamma rays as tracer of dark matter". In: *Astronomy & Astrophysics* 444.1 (2005), pp. 51–67 (p. 12).
- [43] HESS Collaboration et al. "Search for dark matter annihilation signatures in HESS observations of Dwarf Spheroidal Galaxies". In: arXiv preprint arXiv:1410.2589 (2014) (p. 12).
- [44] MG Aartsen et al. "Search for annihilating dark matter in the Sun with 3 years of IceCube data". In: *The European Physical Journal C* 77.3 (2017), p. 146 (p. 12).
- [45] Silvia Adrián-Martínez et al. "Limits on dark matter annihilation in the sun using the ANTARES neutrino telescope". In: *Physics Letters B* 759 (2016), pp. 69–74 (p. 12).

[46] K Choi et al. "Search for neutrinos from annihilation of captured low-mass dark matter particles in the Sun by Super-Kamiokande". In: *Physical review letters* 114.14 (2015), p. 141301 (p. 12).

- [47] O Adriani et al. "Observation of an anomalous positron abundance in the cosmic radiation". In: arXiv preprint arXiv:0810.4995 (2008) (p. 12).
- [48] O Adriani et al. "New measurement of the antiproton-to-proton flux ratio up to 100 GeV in the cosmic radiation". In: *Physical Review Letters* 102.5 (2009), p. 051101 (p. 12).
- [49] M Aguilar et al. "First result from the Alpha Magnetic Spectrometer on the International Space Station: precision measurement of the positron fraction in primary cosmic rays of 0.5–350 GeV". In: *Physical Review Letters* 110.14 (2013), p. 141102 (p. 12).
- [50] Markus Ackermann et al. "Measurement of separate cosmic-ray electron and positron spectra with the Fermi Large Area Telescope". In: *Physical Review Letters* 108.1 (2012), p. 011103 (p. 12).
- [51] Kfir Blum, Boaz Katz, and Eli Waxman. "AMS-02 results support the secondary origin of cosmic ray positrons". In: *Physical review letters* 111.21 (2013), p. 211101 (p. 12).
- [52] Teresa Marrodan Undagoitia and Ludwig Rauch. "Dark matter direct-detection experiments". In: *Journal of Physics G: Nuclear and Particle Physics* 43.1 (2015), p. 013001 (pp. 13, 20).
- [53] Frank J Kerr and Donald Lynden-Bell. "Review of galactic constants". In: Monthly Notices of the Royal Astronomical Society 221.4 (1986), pp. 1023–1038 (p. 13).
- [54] Martin C Smith et al. "The RAVE survey: constraining the local galactic escape speed". In: *Monthly Notices of the Royal Astronomical Society* 379.2 (2007), pp. 755–772 (p. 14).
- [55] David N Spergel. "Motion of the Earth and the detection of weakly interacting massive particles". In: *Physical Review D* 37.6 (1988), p. 1353 (p. 15).
- [56] Andrzej K Drukier, Katherine Freese, and David N Spergel. "Detecting cold dark-matter candidates". In: *Physical Review D* 33.12 (1986), p. 3495 (pp. 15, 19).

[57] CDMS II Collaboration et al. "Dark matter search results from the CDMS II experiment". In: *Science* 327.5973 (2010), pp. 1619–1621 (p. 16).

- [58] Z. Ahmed et al. "Search for annual modulation in low-energy CDMS-II data". In: (Mar. 2012). arXiv: 1203.1309 [astro-ph.CO] (p. 16).
- [59] Craig E Aalseth et al. "CoGeNT: A search for low-mass dark matter using p-type point contact germanium detectors". In: *Physical Review D* 88.1 (2013), p. 012002 (p. 16).
- [60] R Agnese et al. "Search for low-mass weakly interacting massive particles with SuperCDMS". In: *Physical review letters* 112.24 (2014), p. 241302 (p. 16).
- [61] R Agnese et al. "New results from the search for low-mass weakly interacting massive particles with the CDMS low ionization threshold experiment". In: *Physical review letters* 116.7 (2016), p. 071301 (p. 16).
- [62] G Angloher et al. "Limits on WIMP dark matter using scintillating CaWO4 cryogenic detectors with active background suppression". In: Astroparticle Physics 23.3 (2005), pp. 325–339 (p. 16).
- [63] Godehard Angloher et al. "Results from 730 kg days of the CRESST-II Dark Matter Search". In: *The European Physical Journal C* 72.4 (2012), p. 1971 (p. 16).
- [64] G Angloher et al. "Results on light dark matter particles with a low-threshold CRESST-II detector". In: *The European Physical Journal C* 76.1 (2016), pp. 1–8 (p. 16).
- [65] Mark G Boulay and Andrew Hime. "Technique for direct detection of weakly interacting massive particles using scintillation time discrimination in liquid argon". In: *Astroparticle Physics* 25.3 (2006), pp. 179–182 (p. 17).
- [66] Akira Hitachi et al. "Effect of ionization density on the time dependence of luminescence from liquid argon and xenon". In: *Physical Review B* 27.9 (1983), p. 5279 (p. 17).
- [67] AI Bolozdynya. "Two-phase emission detectors and their applications". In: Nuclear Instruments and Methods in Physics Research Section A: Accelerators, Spectrometers, Detectors and Associated Equipment 422.1-3 (1999), pp. 314–320 (p. 17).

[68] Alain Lansiart et al. "Development research on a highly luminous condensed xenon scintillator". In: *Nuclear Instruments and Methods* 135.1 (1976), pp. 47–52 (p. 18).

- [69] Boulay for the DEAP Collaboration et al. "DEAP-3600 Dark Matter Search at SNOLAB". In: arXiv preprint arXiv:1203.0604 (2012) (p. 18).
- [70] Keith Rielage et al. "Update on the MiniCLEAN dark matter experiment". In: arXiv preprint arXiv:1403.4842 (2014) (p. 18).
- [71] K Abe et al. "XMASS detector". In: Nuclear Instruments and Methods in Physics Research Section A: Accelerators, Spectrometers, Detectors and Associated Equipment 716 (2013), pp. 78–85 (p. 18).
- [72] P Benetti et al. "First results from a Dark Matter search with liquid Argon at 87 K in the Gran Sasso Underground Laboratory". In: Astroparticle Physics 28.6 (2008), pp. 495–507 (p. 18).
- [73] Pl Agnes et al. "First results from the DarkSide-50 dark matter experiment at Laboratori Nazionali del Gran Sasso". In: *Physics Letters B* 743 (2015), pp. 456-466 (p. 18).
- [74] A Badertscher et al. "ArDM: first results from underground commissioning". In: Journal of Instrumentation 8.09 (2013), p. C09005 (p. 18).
- [75] Elena Aprile. "The X enon 1T Dark Matter Search Experiment". In: Sources and Detection of Dark Matter and Dark Energy in the Universe. Springer, 2013, pp. 93–96 (p. 18).
- [76] Daniel S Akerib et al. "First results from the LUX dark matter experiment at the Sanford Underground Research Facility". In: *Physical review letters* 112.9 (2014), p. 091303 (p. 18).
- [77] D Yu Akimov et al. "The ZEPLIN-III dark matter detector: Instrument design, manufacture and commissioning". In: *Astroparticle Physics* 27.1 (2007), pp. 46–60 (p. 18).
- [78] XiGuang Cao et al. "PandaX: a liquid xenon dark matter experiment at CJPL". In: *Science China Physics, Mechanics & Astronomy* 57.8 (2014), pp. 1476–1494 (p. 18).

[79] Xiang Xiao et al. "Low-mass dark matter search results from full exposure of the PandaX-I experiment". In: *Physical Review D* 92.5 (2015), p. 052004 (p. 18).

- [80] DC Malling et al. "After LUX: the LZ program". In: arXiv preprint arXiv:1110.0103 (2011) (p. 18).
- [81] DS Akerib et al. "LUX-ZEPLIN (LZ) conceptual design report". In: arXiv preprint arXiv:1509.02910 (2015) (p. 18).
- [82] Rita Bernabei et al. "Final model independent result of DAMA/ LIBRA -phase1". In: *The European Physical Journal C* 73.12 (2013), p. 2648 (p. 19).
- [83] Rita Bernabei et al. "First model independent results from DAMA/LI-BRA -phase2". In: *Universe* 4.11 (2018), p. 116 (p. 19).
- [84] Christopher Savage et al. "Compatibility of DAMA/LIBRA dark matter detection with other searches". In: *Journal of Cosmology and Astroparticle Physics* 2009.04 (2009), p. 010 (p. 19).
- [85] Richard W Schnee. "Introduction to dark matter experiments". In: *Physics of the Large and the Small: TASI 2009.* World Scientific, 2011, pp. 775–829 (p. 19).
- [86] Kfir Blum. "DAMA vs. the annually modulated muon background". In: arXiv preprint arXiv:1110.0857 (2011) (p. 19).
- [87] Jonathan H Davis. "Fitting the annual modulation in DAMA with neutrons from muons and neutrinos". In: *Physical review letters* 113.8 (2014), p. 081302 (p. 19).
- [88] John P Ralston. "One Model Explains DAMA/LIBRA, CoGENT, CDMS, and XENON". In: arXiv preprint arXiv:1006.5255 (2010) (p. 19).
- [89] Emily Shields, Frank Calaprice, and Jingke Xu. "SABRE: A new NaI (T1) dark matter direct detection experiment". In: *Phys. Procedia* 61 (2015), pp. 169–178 (p. 19).
- [90] Marc Schumann. "Direct Detection of WIMP Dark Matter: Concepts and Status". In: J. Phys. G 46.10 (2019), p. 103003. DOI: 10.1088/1361-6471/ab2ea5. arXiv: 1903.03026 [astro-ph.CO] (p. 22).

[91] T. Ikeda et al. "Results of a directional dark matter search from the NEWAGE experiment". In: J. Phys. Conf. Ser. 1468.1 (2020). Ed. by Masayuki Nakahata, p. 012042. DOI: 10.1088/1742-6596/1468/1/ 012042 (p. 22).

- [92] Cosmin Deaconu et al. "Measurement of the directional sensitivity of Dark Matter Time Projection Chamber detectors". In: *Physical Review D* 95.12 (2017), p. 122002 (p. 22).
- [93] Y. Tao et al. "Dark Matter Directionality Detection performance of the Micromegas-based μ TPC-MIMAC detector". In: (Mar. 2020). arXiv: 2003.11812 [physics.ins-det] (p. 22).
- [94] E. Daw et al. "Long-term study of backgrounds in the DRIFT-II directional dark matter experiment". In: JINST 9 (2014), P07021.
 DOI: 10.1088/1748-0221/9/07/P07021. arXiv: 1307.5525
 [physics.ins-det] (p. 22).
- [95] I. Jaegle et al. "Simulation of the Directional Dark Matter Detector (D³) and Directional Neutron Observer (DiNO)". In: EAS Publ. Ser. 53 (2012). Ed. by F. Mayet and D. Santos, pp. 111–118. DOI: 10.1051/eas/1253014. arXiv: 1110.3444 [astro-ph.IM] (p. 22).
- [96] Vincenzo Caracciolo et al. "The ADAMO Project and developments". In: J. Phys. Conf. Ser. Vol. 718. 2016, p. 42011 (p. 22).
- [97] DCaNT: DIRECTIONAL WIMP DETECTION WITH CARBON NANOTUBES. URL: https://web.infn.it/cygnus/dcant/ (p. 22).
- [98] Huajie Cao et al. "Measurement of scintillation and ionization yield and scintillation pulse shape from nuclear recoils in liquid argon". In: *Physical Review D* 91.9 (2015), p. 092007 (p. 22).
- [99] Christian W Fabjan. Particle Physics Reference Library: Volume 2: Detectors for Particles and Radiation. Vol. 2. Springer Nature, 2020 (p. 23).
- [100] Giuseppe PS Occhialini and CF Powell. "Nuclear disintegrations produced by slow charged particles of small mass". In: *Nature* 159.4032 (1947), pp. 186–190 (p. 23).
- [101] MF Kaplon et al. "The Absorption Mean Free Path of the High-Energy Nucleonic Component of Cosmic Radiation". In: *Physical Review* 91.6 (1953), p. 1573 (p. 23).

[102] Giovanni De Lellis. "Charm physics with neutrinos". In: *Nuclear Physics B-Proceedings Supplements* 142 (2005), pp. 109–114 (p. 23).

- [103] N. Agafonova et al. "Final Results of the OPERA Experiment on ν_{τ} Appearance in the CNGS Neutrino Beam". In: *Phys. Rev. Lett.* 120.21 (2018). [Erratum: Phys.Rev.Lett. 121, 139901 (2018)], p. 211801. DOI: 10.1103/PhysRevLett.120.211801. arXiv: 1804.04912 [hep-ex] (p. 23).
- [104] M Natsume et al. "Low-velocity ion tracks in fine grain emulsion". In: Nuclear Instruments and Methods in Physics Research Section A: Accelerators, Spectrometers, Detectors and Associated Equipment 575.3 (2007), pp. 439–443 (p. 25).
- [105] Tatsuhiro Naka et al. "Fine grained nuclear emulsion for higher resolution tracking detector". In: Nuclear Instruments and Methods in Physics Research Section A: Accelerators, Spectrometers, Detectors and Associated Equipment 718 (2013), pp. 519–521 (p. 25).
- [106] A Aleksandrov et al. "NEWS: Nuclear emulsions for WIMP search". In: arXiv preprint arXiv:1604.04199 (2016) (pp. 26, 35, 40, 41, 43, 45).
- [107] N Agafonova et al. "Discovery potential for directional Dark Matter detection with nuclear emulsions". In: *The European Physical Journal* C 78.7 (2018), p. 578 (p. 30).
- [108] Tadaaki Tani and Tatsuhiro Naka. "Nuclear emulsions for dark matter detection". In: *Radiation Measurements* 95 (2016), pp. 31–36 (p. 30).
- [109] Marijke Haffke et al. "Background measurements in the gran sasso underground laboratory". In: Nuclear Instruments and Methods in Physics Research Section A: Accelerators, Spectrometers, Detectors and Associated Equipment 643.1 (2011), pp. 36–41 (p. 31).
- [110] E Aprile et al. "Xenon100 collaboration". In: arXiv preprint arXiv: 1104.2549 (2011) (p. 32).
- [111] D-M Mei and A Hime. "Muon-induced background study for underground laboratories". In: *Physical Review D* 73.5 (2006), p. 053004 (pp. 32, 33).
- [112] Michelangelo Ambrosio et al. "Measurement of the residual energy of muons in the Gran Sasso underground laboratories". In: *Astroparticle physics* 19.3 (2003), pp. 313–328 (p. 33).

[113] A Lindote et al. "Simulation of neutrons produced by high-energy muons underground". In: *Astroparticle Physics* 31.5 (2009), pp. 366–375 (p. 33).

- [114] VA Kudryavtsev, NJC Spooner, and JE McMillan. "Simulations of muon-induced neutron flux at large depths underground". In: Nuclear Instruments and Methods in Physics Research Section A: Accelerators, Spectrometers, Detectors and Associated Equipment 505.3 (2003), pp. 688–698 (p. 33).
- [115] Alfredo Ferrari et al. *FLUKA: a multi-particle transport code*. Tech. rep. Stanford Linear Accelerator Center (SLAC), 2005 (p. 33).
- [116] T Habu et al. "High contrast effects of tetrazolium compounds in silver halide photography". In: *Journal of imaging science* 35.3 (1991), pp. 202–205 (p. 34).
- [117] Mitsuhiro Kimura et al. "WIMP tracking with cryogenic nuclear emulsion". In: Nuclear Instruments and Methods in Physics Research Section A: Accelerators, Spectrometers, Detectors and Associated Equipment 845 (2017), pp. 373–377 (p. 34).
- [118] Robert S Houk et al. "Inductively coupled argon plasma as an ion source for mass spectrometric determination of trace elements". In: *Analytical Chemistry* 52.14 (1980), pp. 2283–2289 (p. 34).
- [119] W Betal Wilson et al. "Sources: a code for calculating (α, n) , spontaneous fission, and delayed neutron sources and spectra". In: *Radiation protection dosimetry* 115.1-4 (2005), pp. 117–121 (p. 34).
- [120] A Alexandrov et al. "Intrinsic neutron background of nuclear emulsions for directional Dark Matter searches". In: *Astroparticle Physics* 80 (2016), pp. 16–21 (p. 35).
- [121] N Armenise et al. "High-speed particle tracking in nuclear emulsion by last-generation automatic microscopes". In: Nuclear Instruments and Methods in Physics Research Section A: Accelerators, Spectrometers, Detectors and Associated Equipment 551.2-3 (2005), pp. 261–270 (p. 36).

[122] A Aleksandrov and V Tioukov. "A novel approach for fast scanning of nuclear emulsions with continuous motion of the microscope stage". In: Nuclear Instruments and Methods in Physics Research Section A: Accelerators, Spectrometers, Detectors and Associated Equipment 718 (2013), pp. 184–185 (p. 36).

- [123] A Alexandrov et al. "A new fast scanning system for the measurement of large angle tracks in nuclear emulsions". In: *Journal of Instrumentation* 10.11 (2015), P11006 (pp. 36, 38).
- [124] A Alexandrov, V Tioukov, and M Vladymyrov. "Further progress for a fast scanning of nuclear emulsions with Large Angle Scanning System". In: *J. Instrumentation* 9 (2014), p. C02034 (p. 37).
- [125] Andrey Alexandrov et al. "The continuous motion technique for a new generation of scanning systems". In: *Scientific reports* 7.1 (2017), pp. 1–10 (p. 38).
- [126] Andrey Alexandrov, Giovanni De Lellis, and Valeri Tioukov. "A Novel optical scanning technique with an Inclined Focusing plane". In: *Scientific Reports* 9.1 (2019), pp. 1–10 (p. 38).
- [127] K Morishima and T Nakano. "Development of a new automatic nuclear emulsion scanning system, S-UTS, with continuous 3D tomographic image read-out". In: *Journal of Instrumentation* 5.04 (2010), P04011 (p. 38).
- [128] Nicola D'Ambrosio et al. "Nuclear emulsions as a very high resolution detector for directional dark matter search". In: *Journal of Instrumentation* 9.01 (2014), p. C01043 (p. 38).
- [129] A Alexandrov et al. "Development of a super-resolution optical microscope for directional dark matter search experiment". In: Nuclear Instruments and Methods in Physics Research Section A: Accelerators, Spectrometers, Detectors and Associated Equipment 824 (2016), pp. 600–602 (pp. 38, 39).
- [130] Andrey Alexandrov et al. "Super-resolution high-speed optical microscopy for fully automated readout of metallic nanoparticles and nanostructures". In: *Scientific Reports* 10.1 (2020), pp. 1–12 (pp. 39, 40, 73).

[131] Hiroharu Tamaru et al. "Resonant light scattering from individual Ag nanoparticles and particle pairs". In: Applied physics letters 80.10 (2002), pp. 1826–1828 (pp. 40, 44, 45).

- [132] M Kimura and T Naka. "Submicron track readout in fine-grained nuclear emulsions using optical microscopy". In: Nuclear Instruments and Methods in Physics Research Section A: Accelerators, Spectrometers, Detectors and Associated Equipment 680 (2012), pp. 12–17 (p. 41).
- [133] F Mayet et al. "R&D status of nuclear emulsion for directional dark matter search". In: *European Astronomical Society Publications Series* 53 (2012), pp. 51–58 (p. 41).
- [134] T Naka et al. "Analysis system of submicron particle tracks in the fine-grained nuclear emulsion by a combination of hard x-ray and optical microscopy". In: *Review of Scientific Instruments* 86.7 (2015), p. 073701 (pp. 42, 44).
- [135] Jules L Hammond et al. "Localized surface plasmon resonance as a biosensing platform for developing countries". In: *Biosensors* 4.2 (2014), pp. 172–188 (p. 44).
- [136] James F Ziegler, Matthias D Ziegler, and Jochen P Biersack. "SRIM—The stopping and range of ions in matter (2010)". In: Nuclear Instruments and Methods in Physics Research Section B: Beam Interactions with Materials and Atoms 268.11-12 (2010), pp. 1818–1823 (p. 49).
- [137] Francois Chollet. Deep Learning mit Python und Keras: Das Praxis-Handbuch vom Entwickler der Keras-Bibliothek. MITP-Verlags GmbH & Co. KG, 2018 (pp. 60, 65).
- [138] Sebastian Raschka. *Python machine learning*. Packt publishing ltd, 2015 (pp. 60, 62, 64).
- [139] Salman Khan et al. "A guide to convolutional neural networks for computer vision". In: Synthesis Lectures on Computer Vision 8.1 (2018), pp. 1–207 (p. 60).
- [140] Alan M Turing. "Computing machinery and intelligence (1950)". In: The Essential Turing: The Ideas that Gave Birth to the Computer Age. Ed. B. Jack Copeland. Oxford: Oxford UP (2004), pp. 433–64 (p. 61).
- [141] Diederik P Kingma and Jimmy Ba. "Adam: A method for stochastic optimization". In: arXiv preprint arXiv:1412.6980 (2014) (p. 62).

[142] Multi-Class classification. URL: https://medium.com/@b.terryjack/tips-and-tricks-for-multi-class-classification-c184ae1c8 ffc (p. 63).

- [143] Recurrent neural network. URL: https://www.oreilly.com/library/view/neural-networks-and/9781492037354/ch04.html (p. 66).
- [144] K Fukushima and S Miyake. Neocognitron: A self-organizing neural network model for a mechanism of visual pattern recognition In: Competition and cooperation in neural nets. 1982 (p. 66).
- [145] David H Hubel and Torsten N Wiesel. "Receptive fields of single neurones in the cat's striate cortex". In: *The Journal of physiology* 148.3 (1959), p. 574 (p. 67).
- [146] Yann LeCun et al. "Backpropagation applied to handwritten zip code recognition". In: *Neural computation* 1.4 (1989), pp. 541–551 (p. 67).
- [147] Ibtesam M Dheir et al. "Classifying Nuts Types Using Convolutional Neural Network". In: (2020) (p. 68).
- [148] Dan Ciregan, Ueli Meier, and Jürgen Schmidhuber. "Multi-column deep neural networks for image classification". In: 2012 IEEE conference on computer vision and pattern recognition. IEEE. 2012, pp. 3642–3649 (p. 68).
- [149] Sparsh Mittal. "A survey of FPGA-based accelerators for convolutional neural networks". In: *Neural computing and applications* (2020), pp. 1–31 (p. 68).
- [150] Ian Goodfellow. "NIPS 2016 tutorial: Generative adversarial networks". In: arXiv preprint arXiv:1701.00160 (2016) (p. 68).
- [151] Min Lin, Qiang Chen, and Shuicheng Yan. "Network in network". In: arXiv preprint arXiv:1312.4400 (2013) (p. 68).
- [152] Sripad Ram et al. "High accuracy 3D quantum dot tracking with multifocal plane microscopy for the study of fast intracellular dynamics in live cells". In: *Biophysical journal* 95.12 (2008), pp. 6025–6043 (p. 74).
- [153] Keras library. URL: https://keras.io/ (p. 74).
- [154] Tensorflow library. URL: https://www.tensorflow.org/ (p. 74).

[155] R Hahnloser et al. "Digital selection and analog amplification co-exist in an electronic circuit inspired by neocortex". In: *Nature* 405.6789 (2000), pp. 947–951 (p. 75).